Politecnico di Milano
Department of Energy
Doctoral Program in Energy

Characterization and performance assessment of air permeable building components

Doctoral Dissertation of:
Andrea ALONGI

Supervisor:
Prof. Livio MAZZARELLA

The Chair of the Doctoral Program:
Prof. Carlo Enrico BOTTANI

2012 - XXIII

Research, such as life,
is meaningless
unless is shared...

Abstract

Dynamic insulation walls can be used in buildings to achieve a high level of integration between envelope and ventilation system. This technology, which has been studied in northern Europe since the early Nineties, is based on the passage of ventilation air through porous layers of the walls: in this way, such layers act both as a heat exchanger and as a filter.

This research work is aimed at obtaining a good comprehension of heat and mass transfer mechanisms inside porous materials. With this purpose, a detailed study of possible theoretical approaches has been performed, leading to the implementation of the volume average method. This mathematical procedure allows us to take into account the macroscopic effects of the microscopic interaction between fluid and solid phase of a porous domain. Correction parameters, such as thermal tortuosity and thermal dispersion, have been defined and quantified, by means of the characterization of fibrous insulation an no-fines concrete.

Both materials have been modeled to perform CFD parametric simulations: while fibrous insulation has been geometrically simplified, describing the solid matrix as a ordered array of parallel cylinders, no-fines concrete has been studied by means of image analysis technique, applied on real samples we have produced. Numerical results have been used to correlate thermal tortuosity and dispersion with macroscopic quantities (porosity and Peclet number). Air permeability and Ergun coefficient have also been obtained, and, for what concerns the concrete-based material, experimentally validated.

Both theoretical and numerical achievements have been used in the development of a one-dimensional full-implicit finite difference model, aimed at the simulation of dynamic insulation multi-layered components under transient boundary conditions. The algorithm as been used to build a Type for the TRNSYS© calculus suite.

In the last part of this work, it is reported the description of an experimental apparatus we have designed and built. It is based on two chambers connected through the porous sample and a ventilation system. The laboratory arrangement is able to reproduce both steady state and transient temperature conditions, independently in each chamber. It will be used to validate all numerical and theoretical results presented in this dissertation.

Acknowledgments

I would like to thank my supervisor, Professor Livio Mazzarella, for his support, his advice and for the trust that had in my work.

I also wish to thank Professor Luca Bertolini and his research group from the "G.Natta" Department of Politecnico di Milano, for the help they gave me in part of the experimental work I have done.

I would also like to mention here all my colleagues: it is just because of you that I feel it is a pleasure to come to work every day, even in bad times. Among them, a special thanks goes to Tommaso and Rossano (if you think about it, I'm sure you know why).

Thanks to my parents and my family for their love, their encouraging words, for always spurring me to believe in myself and give my best, even when weariness and frustration threatened to take over. Your support helped me to overcome difficult moments, when my work was becoming meaningless to me.

I wish also to thank my wife Eleonora: reading what I wrote in the acknowledgments of the master graduation thesis, I have realized of how much time has passed since then, how many things we have shared and how you have been important to me over these years. So, simply, thank you for your love.

And now, few words to thank my friends: Guido e Giovanni, for every beer, every movie and every night spent talking about everything and nothing; Daniele, because every time we meet I feel like we had never part with; the Danieles, you are two wonderful people, and I'm glad you became part of my life (Eleonora... thank you also for that...); Michele, Simona and *le Tope*, my friends from Tibaldi, and my old colleagues from university (Sara, Paola, Paolo, Stefano, and all the others), thank you for all the time spent together. Finally, all the old and new friends I have not named, but that somehow have supported me with words and affection.

Finally, a last, loving thoughts goes to Mario.

Contents

Nomenclature

A	Surface (m^2)
c	Specific heat $(J/(kgK))$
c_p	Specific heat at constant pressure $(J/(kgK))$
C_E	Ergun coefficient $(m?2)$
h	Heat transfer coefficient $(W/(m^2K))$
$\mathbf{K}$	Permeability tensor (3-by-3) (m^2)
K	Permeability (m^2)
L	Reference length (m)
L_{ACF}	Reference length related to autocorrelation function(m)
L_ε	Reference length related to porosity(m)
$\underline{n}_{sf}$	Local coordinate normal to A_{sf} - $\underline{n}_{sf} = n_{sf,x}\underline{i} + n_{sf,y}\underline{j}$
Nu	Nusselt number (-) - $Nu = \frac{h_{cv} \cdot L}{\lambda_{air}}$
p, P	Pressure (Pa)
Pe	Peclet number (-) - $Pe = u \cdot \frac{L_{REV}(\rho c_p)_f}{\lambda_f}$
R	Thermal resistance (m^2K/W)
R	Electrical resistance (Ω)
Re	Reynolds number (-) - $\frac{\rho \cdot u \cdot L}{\mu}$
t	Time coordinate (s)
T	Temperature (K)
$\mathbf{u}$	Local velocity vector $(m/s])$ - $\mathbf{u} = u\underline{i} + v\underline{j}$
u	Local value of x component of $\mathbf{u}($ $m/s)$
U	Thermal transmittance $(W/(m^2K))$
V	Volume (m^3)
x	Space coordinate (m)

Greek symbols

α	Thermal diffusivity (m^2/s)
α	Solar absorbance (-)
α_{TCR}	Temperature coefficient of resistivity $(1/K)$
ε	Volume fraction of the fluid phase, or *porosity* (-)
ϵ	Surface emissivity (-)
φ_{sol}	Solar irradiance (W/m^2)
λ	Thermal conductivity $(W/(mK))$
μ	Dynamic viscosity $(Pa \cdot s)$
ρ	Density $[kg/m^3]$

Subscript

cv	Convective quantity
eff	Effective quantity
f	Quantity referred to fluid
$disp$	Referred to thermal dispersion $(W/(mK))$
D	Referred to Darcean (or *filter*) velocity (m/s)
rd	Radiative quantity
REV	Quantity referred to the REV
s	Quantity referred to solid
sf	Interface between fluid and solid phase
tor	Referred to thermal tortuosity $(W/(mK))$

Special operators

$\langle\phi\rangle$	Volume average of ϕ
$\tilde{\phi}$	Local space deviation of ϕ

Acronyms

CFD	Computational Fluid Dynamic
$DAVTB$	Dual Air Vented Thermal Box
TPS	Transient Plane Source
REV	Representative Elementary Volume

Introduction

This study is focused on the *dynamic insulation* technology, also known as *breathable wall* technology. Building envelope components belonging to this category are generally multi-layered walls, which include air permeable layers in the stratigraphy. Such layers are crossed by ventilation air of confined environments, thus acting as heat exchangers and a filters of the ventilation system.

This technology has been studied in Northern European countries since the early Nineties, and is based on the integration between building envelope and ventilation plant: in cold climates, air entering through the wall is preheated (and filtered), because of the heat exchange with the solid matrix of porous layers, and the energy load to the plant is reduced. In past years, some efforts have been made by various research groups to assess energy performance of this technical solution, by means of analytical, numerical or experimental approaches. In Chapter 1 a short review of works found in literature is presented.

A careful analysis of earlier studies has led to following considerations: first of all, dynamic insulation seems to be promising in the reduction of energy consumption for building usage; secondly, some technological issues have been raised, mainly related to the superficial temperature reduction due to the air flow; moreover, we

have found only few studies aimed at the assessment of the energy performance of dynamic insulation components in hot climates. Finally, we have noticed that the analytical approach used in all past works introduces an implicit simplification in dealing with the heat transfer in porous media.

Going more in detail, the approach involved to describe thermophysical properties of porous materials usually does not take into account the microscopic interaction between fluid and solid phases of the medium. Moreover, neither effects of flowing air, nor effects of the solid matrix geometry are considered. Hence, we have applied the volume average method to the problem under discussion, in order to assess the macroscopic effects of the heat transfer in porous media at the microscopic level. Furthermore, while in earlier works the fluid mechanics of the problem is not treated explicitly, we have analyzed some possible approaches to evaluate the air velocity inside interconnected pores, from a macroscopic point of view. All theoretical considerations are reported in Chapter 2, together with all the required mathematical instruments.

The theoretical approach selected has led to the definition of new quantities, such as thermal tortuosity and thermal dispersion, which are related to the geometrical structure of the solid matrix of the porous material considered. The same consideration can be done about parameters that influence the fluid dynamic behavior of the air flowing inside pores (permeability and Egrun coefficient). In order to quantify these parameters, and their effects on the overall problem, numerical and experimental analyses have been performed.

Going more in depth, two main categories of materials have been considered: fibrous insulation (e.g. rock wool), and no-fines concrete. In both cases, CFD

simulations have been done on small portions of the porous domains, typical for the aforementioned materials, in order to calculate the temperature distribution and the velocity field under various boundary conditions. While the first kind of porous medium has been strongly simplified from the geometrical point of view, the solid matrix of pervious concrete has been carefully characterized, by means of image analysis of samples. Moreover, thermophysical properties of the solid phase, permeability and Ergun coefficient have been experimentally derived for the concrete-based material considered. All the performed analyses are reported in Chapters 3 and 4.

Along with the material characterization, which is mandatory to correctly describe both the fluid dynamic and the heat transfer in porous media, a numerical algorithm aimed at the simulation of dynamic insulation building components under transient boundary conditions has been developed. Therefore, a one-dimensional time-dependent finite difference model has been produced. More in detail, a code has been developed using the MATLAB® environment: its purpose is to simulate multi-layered walls, with both permeable and not-permeable layers implemented (like the real component may be). Then, the code has been used to define a TRNSYS® Type: in this way, it will be possible to simulate the whole building with breathable walls, taking into account their interaction with other structures, and the effects of various boundary conditions (climate, internal gains, ventilation rate, etc.). The whole algorithm is described in Chapter 5.

It is important to notice that all results, coming from the studies previously presented, need an empirical validation to assess their reliability. For this reason, we have decided to design and build an experimental apparatus, which is able to

reproduce both steady state and transient thermal boundary conditions (Chapter 6).

Chapter 1

Dynamic insulation technology

The aim of this Chapter is to introduce a kind of building envelope system usually called *dynamic insulation*, also known as *breathable wall*. In the next sections, a description of this technology and its physical and technical foundations is provided to the reader. Then, a summary of its evolution and present state of the art is given. Successively, pros and cons of this technology are discussed.

1.1 Technological description

The system under study is a particular kind of parietodynamic building envelope technology, which means that it is able to modify its behavior according to different climate and working conditions [1]. For instance, the so called double-skin façade could be considered a parietodynamic system, because it can change its performance thanks to the variable intensity and direction of the ventilation rate across it.

Since the early Nineties, some studies have been developed in relation to opaque closure systems (either vertical or horizontal), which are usually known as *dynamic*

insulation [2]. This technology is based on the integration between ventilation plant and building structures, and works as follows: instead of being delivered or extracted through ducts or openings, ventilation air is forced to go slowly through dedicated building envelope porous walls, like that represented in Figure 1.1, which consequently acts as a heat exchanger [3] and a filter [4] of the ventilation system. Hence, air is pre-tempered using the waste heat normally lost through the fabric of the building. Depending on the rate of the air flow, part or all of the fabric heat that is normally lost is recovered to the building's fresh air ventilation supply.

If we consider the vertical envelope solution, the system is, from the technical point of view, in many aspects similar to conventional walls, because it is composed by [5]:

1. external screen for protection against weather conditions (rain, wind, etc.);
2. external ventilated cavity;
3. insulating substrate (in the case of dynamic insulation, it may include one or more layers of material with open cell pores);
4. internal ventilated cavity (it can be directly linked with the internal environment, or can be connected to the ventilation plant, if present);
5. internal finishing.

Finally, it is possible to identify two main working configurations: *pro-flux*, where heat flux and air flow have the same direction (incoming or outgoing), and *contra-flux*, where they have opposite direction. An example of building design with dynamic insulation is presented in [6].

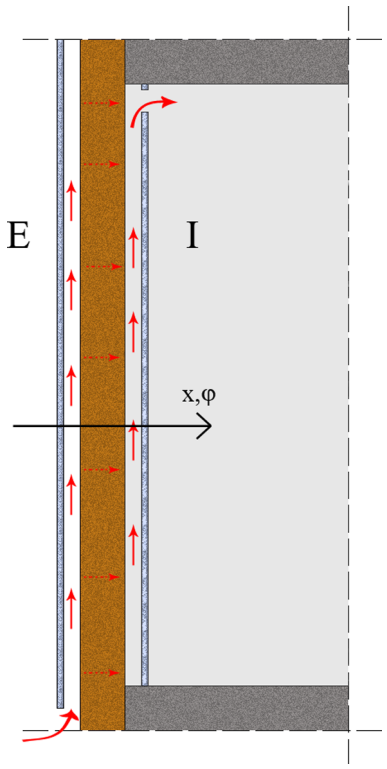

Figure 1.1: Typical multi-layered dynamic insulation wall.

1.2 The wall as a heat exchanger

1.2.1 Steady state heat transfer

The evaluation of the temperature profile in a three-layer wall has been done considering the heat transfer phenomenon in steady state condition [7], using the following equation:

$$\lambda_i \frac{\mathrm{d}^2 T(x)}{\mathrm{d}x^2} - u\rho_a c_a \frac{\mathrm{d}T(x)}{\mathrm{d}x} = 0 \quad \text{with} \quad i = 1, 2, 3. \tag{1.1}$$

where ρ_a, c_a and u are the density, the specific heat and the velocity of the flowing air, and λ_i is the thermal conductivity of the i-th layer.

In Eq. (1.1) both conductive and convective terms are present. We underline that

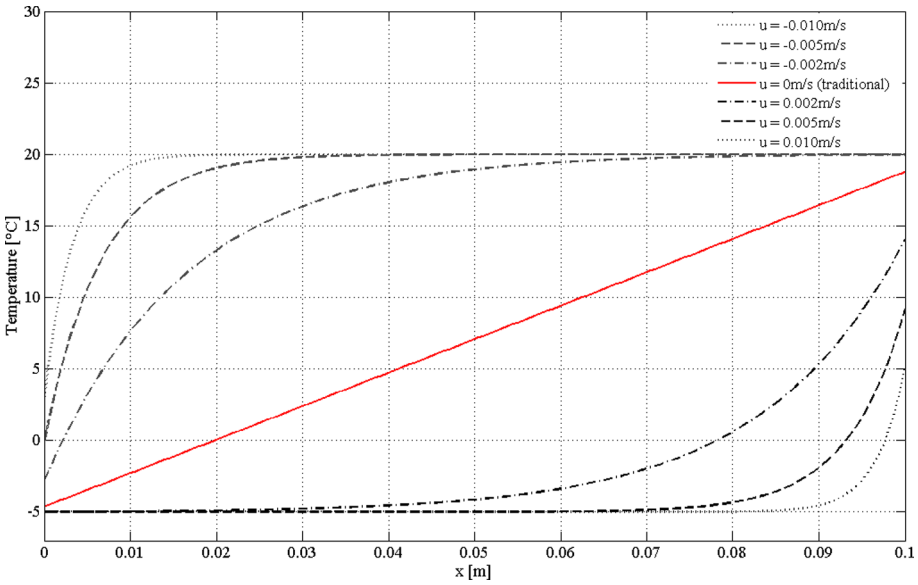

Figure 1.2: Temperature profile inside a single layer wall, in steady-state condition (Neumann boundary conditions).

the convention adopted is the one described in Figure 1.1. After the introduction of appropriate boundary conditions (Dirichlet or Neumann conditions at the domain boundary, temperature and flux continuity at the layers interfaces), the temperature distribution represented in Figure 1.2 has been found.

The heat exchange the between flowing air and the solid matrix of the porous layer yields to a reduction of the effective U-value, as represented in Figure 1.3. From the analytical point of view, the equation to evaluate the U-value of the air-permeable part of the wall is [3, 5]:

$$U_{dyn} = \frac{u\rho_a c_a}{R_s e^{(u\rho_a c_a R_s)} - 1} \tag{1.2}$$

where R_s is the thermal resistance of layers involved. If a wall is composed by both by *stationary* (diffusive) and dynamic layers, its effective transmittance U_{eff}

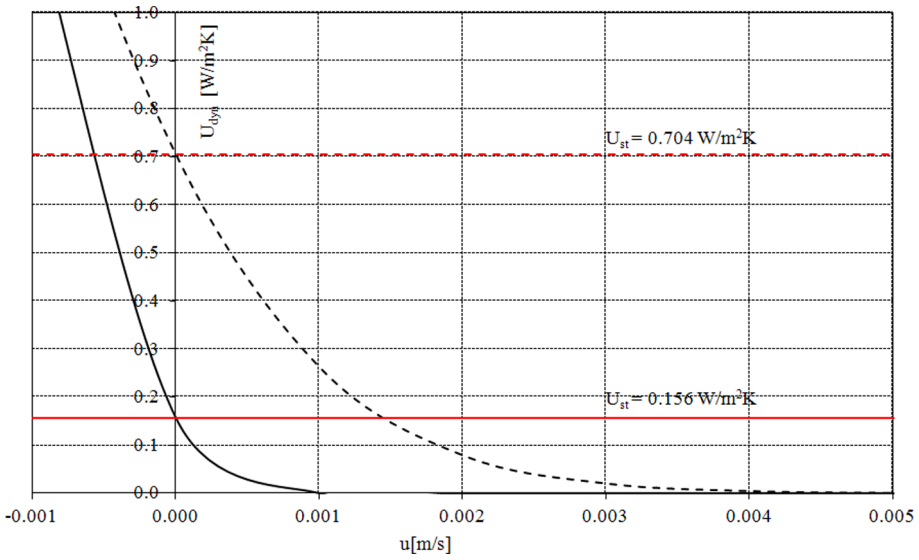

Figure 1.3: Transmittance variation as a function of air velocity.

becomes [5]:

$$U_{eff} = \frac{1}{\frac{1}{U_{st}} + \frac{1}{U_{dyn}}} \tag{1.3}$$

where U_{st} is the U-value of the diffusive part of the considered wall.

Considering Figure 1.3 and Eq. (1.2), the dynamic part of the U-value depends on the air velocity and on the thermal resistance of the layer: the reduction of thermal transmittance for growing air velocity values is more effective in a well insulated wall. It is also possible to infer a non symmetrical behavior of the envelope in *pro* and *contra-flux* conditions.

Finally, it is important to notice that thermophysical properties of porous materials involved in Eq. (1.1) (thermal conductivity, density and specific heat), are calculated as a volume average value of corresponding properties of both air and the solid part of the material. This introduces an implicit simplification, by neglecting

the macroscopic effects of the microscopic interaction between the fluid and the solid part that compose the porous media (contact surface, geometry, convective heat exchange, etc.).

1.2.2 Numerical analysis

In literature, a numerical study of energy performance of the dynamic insulation technology has been found. It is presented in [8]: a set of CFD simulation of a room with dynamic insulation has been performed, evaluating heat losses and thermal comfort for different working conditions.

For the reference condition, two walls are dynamically insulated (while the others are connected to adjacent rooms - i.e. adiabatic condition) and the total air flow passes through them (1 volume per hour). No infiltrations and heating plant have been considered at the beginning. The only internal gains are provided by a person with a heat generation of 70 W and a uniformly distribute heat source of 20 W/m^2, which could result from a underfloor heating plant, or from other rooms heat gains (e.g. lighting). In other simulations, air infiltrations are taken into account to evaluate the effects on comfort conditions. A radiator and an heat recovery unit are introduced.

The study presented has demonstrated the influence of the air tightness of the whole envelope on the effectiveness of dynamic insulation closures. Furthermore, the need for careful design has been emphasized, to ensure an adequate level of the wall internal surface temperature, which strongly affects comfort conditions (such achievement has been analytically confirmed in [9]).

1.2.3 Field and experimental analyses

Some experimental works on dynamic insulation systems, both field studies and laboratory tests, have been found in literature.

The first work is reported in [10]: this paper deals with the evaluation of two upon 12 residential buildings in the Oslo area with dynamically insulated roof. The air flow has been provided by imposing a 10 Pa pressure difference between indoor and outdoor (obtaining an air velocity through the insulation around 2 m/h). The ventilation rate has been set around 1.1 volumes per hour, including the air changes through the ventilation plant (0.8 vol/h) and the ones coming through leaks in walls and floors (about 0.3 vol/h). Following parameters have been measured: temperature inside, outside and the profile through the dynamic insulation; pressure difference between outside, the attic, through the insulation and the inside; wind speed and direction; ventilation rate inside and in the attic; tightness and thermography of the houses. Following conclusions are given: first of all, in buildings with good air tightness, dynamic insulation can significantly heat losses through the envelope; secondly, the control strategy for the ventilation rate needs to be accurately defined.

The second work [11] deals with the evaluation of the inner and the outer air film resistance. The performance of dynamic insulation has been studied using a hot-box, in order to measure the temperature profile through the wall (a single layer of mineral wool). Measured and theoretical data have been matched assuming 0.14 m^2K/W and 0.19 m^2K/W for inner and outer thermal resistance of the air film respectively. Such values have been demonstrated theoretically.

In [12] an experimental work on a wall component tested under real weather conditions is reported. Indoor and outdoor climatic conditions have been measured: beam and diffuse solar radiation, long wave radiation, wind velocity and direction, relative humidity, air and surface temperature, and heating and cooling power demand. Tests have been performed both in winter and spring, to evaluate dynamic insulation system performance for various pressure difference between indoor and outdoor and for two control regimes (fixed temperature around 22 °C and free floating). This work leads to following considerations: first of all, internal superficial temperature decreases when air flow rate increases (rising air velocity); secondly, it is important to adjust working configuration (pro or contra-flux) taking into account external climatic conditions; finally, conductive heat losses through wall decrease for increasing pressure difference values (which affects air velocity through the envelope component).

The most recent work found in literature is described in [13]: a field study of a dynamic insulation panel has been performed in a residential building in Abu Dhabi, during the hottest period of the year (from June to September). The dynamic insulation cell (0.6m × 0.6m × 0.095m) is a commercial product, composed by a fiber-based porous material contained within a rigid EPS encasement package. Results have highlighted that the ventilation air is pre-cooled by an average of 3 °C (this cooling effect can go from 2-4 °C in the evening and in the early morning, to 6-12 °C during the hottest part of the day).

1.3 The wall as an air filter

As we previously stated, walls based on dynamic insulation technology are able to act as a filter, when they are integrated in the ventilation plant of a building: particles drawn by the flowing air are trapped by the solid matrix of the porous "filter".

This behavior is studied in [4], where the collection efficiency of dynamic insulation layers is analyzed, as a function of particles diameter a air velocity. Generally, a traditional air filter has an open fibrous structure, with a porosity around 90-95%. Trapping mechanisms are (Figure 1.4):

Direct interception, which involves a particle following a streamline and being captured, if it comes directly into contact with a fiber.

Inertial impaction, in which a particle is captured because it deviates by its own inertia from the streamlines around the fiber.

Diffusional deposition, in which Brownian motion of the particle brings it into contact with the fiber.

Thanks to the low air velocity typically used for this technology, all the three mechanisms previously described are involved, while the third is not activated in traditional filters.

A way to represent a fibrous filter behavior is the single fiber theory, which evaluates the flow field around a fiber, taking into account neighboring fibers. This flow field is used to calculate particles trajectories. Thank to this approach, it has been possible to demonstrate that a fibrous dynamic insulation layer can effectively trap most of small air borne particles, whit a high collection efficiency for the

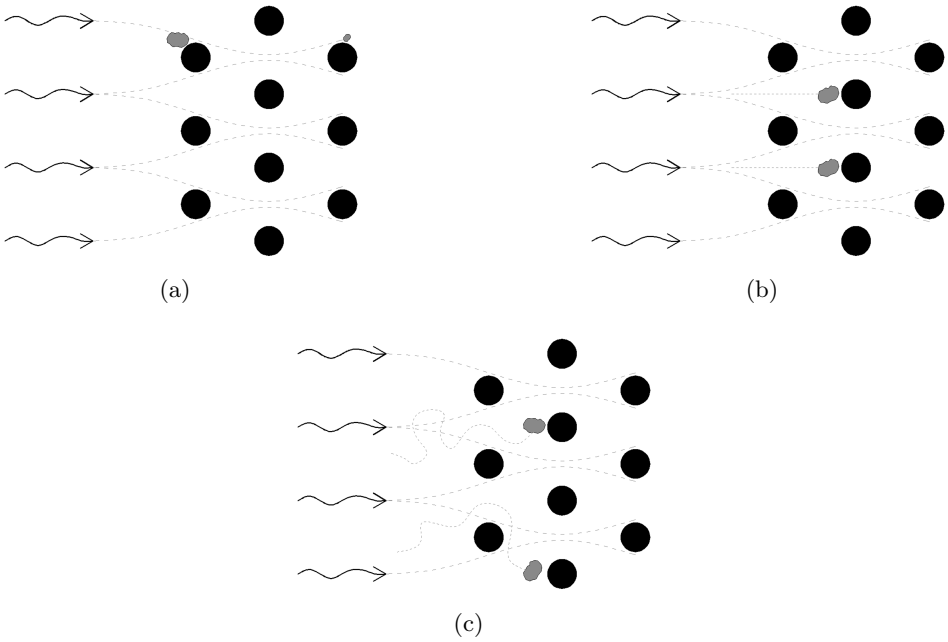

Figure 1.4: Particle filtration mechanisms: (a) *direct interception* (the larger particles are carried by the air flow to impact against the fibers, while the smaller ones deviate); (b) *inertial impaction* (the airflow diverges close to the fibers, but the particles continue to move by inertia in a straight line), (c) *diffusional deposition* (for low speed flows, the Brownian motion brings particles to impact on fibers).

so-called *thin particulate* [5]: only the 1% of particles with diameter lower than 0.022 μm and grater than 7.5 μm penetrates a dynamic insulation layer with a thickness of 1 mm.

For what concerns filter clogging, studies of porous ceilings reported in [4] have shown that on samples that have been installed for 6-16 years there was no noticeable decrease in air permeability, if compared with initial values. It has been estimated that, for a flow rate of 80 m^3/m^2h, the lifetime of a mineral wool layer would exceed 20 years. In homes and office buildings, flow rates are generally one order of magnitude lower, which leads to a slower dust accumulation rate in air permeable layers of walls.

1.4 Material properties

Fibrous insulating materials have been generally used to build dynamic insulation systems: in fact, this technology has been initially developed for cold North-European climates, where the main task for the building envelope is to reduce thermal losses in winter. Then, the thermal resistivity has been considered as the main way to achieve this goal.

Another approach, which has not yet led to a commercial product, is the use of capacitive materials, such as concrete blocks or panels. Going more in detail, to guarantee a sufficient level of air permeability, an air permeable concrete (APC) has been studied as a potential component for dynamic insulation systems [14].

When hardened, this compound is highly porous and voids are interconnected to allow air permeability. Their diameter is in a range between 0.5 mm and 5 mm. In [14] a mathematical procedure to evaluate effective thermal conductivity (λ_e) is presented, with following assumption:

- effects of aggregates shape, size and size distribution on λ_e are negligible;
- change in packing behavior resulting from interparticle forces is assumed to be constant;
- solid matrix is assumed do be dry.

This porous material is treated as a three-phase domain with a one-dimensional heat transfer model, with the assumption of negligibility of radiative and convective heat transfer. This model leads to the following equation for effective thermal

conductivity:

$$\lambda_e = (\phi_a + \phi_c) \left\{ \frac{\lambda_v \lambda_c}{\phi_c \lambda_v + \phi_v \lambda_c} + [\phi_c \lambda_c + \phi_a \lambda_a] \right\} \cdot (1 - P_t) \tag{1.4}$$

where P_t is a cement porosity factor based on the water/cement ratio, ϕ_a, ϕ_c and ϕ_v are the volume fraction of aggregates, cement paste and voids respectively.

This model has been validated by means of laboratory tests using the hot wire method. Predicted results show an acceptable agreement with experimental data when the filling degree is in a range between 50% and 100%. Predictions for lower values are not supported experimentally.

1.5 Objective and content of the research

According to the literature analysis, it is possible to underline strengths and weaknesses of the dynamic insulation technology: first of all, it has been demonstrated that with the convective component it is possible to significantly reduce the envelope thermal transmittance; furthermore, this technology provides a good level of integration between the ventilation system and the building envelope (higher mass involvement, lower entrance velocity of the ventilation air, high filtration efficiency). As far as cons are concerned, comfort issues have been detected, associated to a reduction of internal surface temperature for rising air velocity; secondly, it is important to underline a manufacturing complexity of the system, and a strong dependence of its performance by the whole envelope air tightness (adequate control of stray leakage).

With the described background, this research is divided into the following top-

ics. First of all, a different theoretical approach to heat transfer in porous media is taken into account: the differential equation of thermal energy is derived using the averaging volume method. The evaluation of effective thermal conductivity is than achieved by means of parametric CFD simulations. Secondly, a finite difference algorithm to simulate air permeable walls in transient conditions has been developed, in order to assess dynamic insulation performance in hot climates (which have not been analyzed in detail in past works). Finally an experimental apparatus have been designed and built, with the aim both to validate the theoretical model and the calculus algorithm, to investigate pro and contra flux working configurations, and to test the technology behavior under variable temperature boundary conditions.

Chapter 2

Fluid mechanics and heat transfer in porous media

The mathematical description of the heat transfer through a dynamic insulation layer has been presented in Chapter 1 and is mathematically described with Eq. (1.1), which is based on the assumption of isotropic and homogeneous medium. In this equation, density, specific heat and thermal conductivity of the porous layer are considered from a macroscopic point of view. This means that each of these quantities is an average value over the flowing fluid (air) and the solid matrix of the material (i.e. values obtainable from data sheets). Furthermore, their dependence on the flow field inside cavities is not taken into account explicitly. In this way, the thermal (convective) interaction between the fluid and the solid phase at a microscopic level is not considered, as well as the geometry of the solid microstructure.

Since we do not have found in literature any rigorous analysis to demonstrate, from the theoretical point of view, the validity of the simplified model previously

described (in the range of the parameters typical for the problem under examination - dynamic insulation layers), we have decided to study in deep the convective and conductive heat transfer in porous media. For this purpose, in order to take into account the effects of microscopic interaction on the macroscopic thermal performance of a dynamic insulation layer, we have decided to solve the velocity field (air velocity is not any more a problem parameter) and to use the average volume method [15–19] for the energy equation.

2.1 Porosity

If we consider a porous medium, *porosity* is defined as the ratio between the total void volume and the the total volume occupied by both void and solid matrix.

Moreover, a pore can be connected with more than another one (*interconnected*), to only another void (*dead end*) or is not connected (*isolated*). The volume fraction of the interconnected pores is called *effective porosity*.

Furthermore, a porous material is characterized not only by its porosity, but also by its solid matrix structure, which affects the pore structure. In fact, pores can have various size, can be connected or not and, finally, the whole structure can be ordered or disordered (and isotropic).

This leads to various matrix structures, with different levels of simplicity. From this distinction comes the need of appropriate analytical, numerical and experimental approaches to treat the effects of the microscopic geometry on the macroscopic fluid mechanics and heat transfer problem.

2.2 The local volume averaging technique

The purpose of this section is to briefly describe theorems and mathematical principles that underpin the local volume averaging method.

This technique has been applied on transport and energy equations in order to precisely describe multiphase systems behavior: the aim of this procedure is to reach a rigorous treatment of transport phenomena in porous media, taking into account all microscopic interaction between phases and describing their effects on the macroscopic behavior of the whole domain (which is then considered homogeneous).

As previously noted, the phenomenon of heat transfer in porous media has a number of complexities related to the microstructural inhomogeneity of the material: it is possible to identify two phases that constitute the porous medium: respectively a solid (s) and a fluid phase (f) - Figure 2.1.

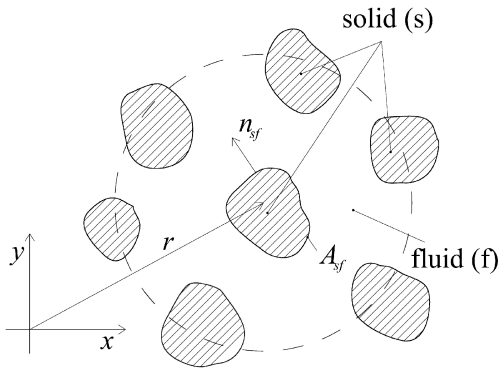

Figure 2.1: Schematic representation of the microstructure of a generic porous medium.

This implies the need for appropriate mediation techniques of thermophysical characteristics, in order to treat the problem from the macroscopic point of view, taking into account the microstructure of the material at the same time.

One of possible approach is the volume averaging technique [15, 17, 20]. Consid-

ering a thermodynamic property ψ, with a surface flux vector $\mathbf{i}$, an external source f and a volumetric production G, the corresponding conservation equation is:

$$\frac{\partial(\rho\psi)}{\partial t} + \nabla \cdot (\rho \mathbf{u}\psi) - \nabla \cdot \mathbf{i} - \rho f = \rho G \tag{2.1}$$

where ρ is the density and $\mathbf{u}$ is the velocity field in a point $\mathbf{r}$. Eq. (2.1) is applicable both to the solid and the fluid phase (the domain can be treated as a generic bi-phase system α-phase $\cup$ β-phase), while decays at the interface between phases or, more generally, at every discontinuities of the domain (*Theorem I*). At the interface $\alpha\beta$ the balance equation becomes:

$$(\rho\psi(\mathbf{w} - \mathbf{u}) + \mathbf{i})|_\alpha \cdot \underline{n}^{\alpha\beta} + (\rho\psi(\mathbf{w} - \mathbf{u}) + \mathbf{i})|_\beta \cdot \underline{n}^{\beta\alpha} = 0 \tag{2.2}$$

where $\mathbf{w}$ is the interface velocity and $\underline{n}^{\alpha\beta}$ is the unit vector perpendicular to the surface and directed from α to β (than we have $\underline{n}^{\alpha\beta} = -\underline{n}^{\beta\alpha}$). The microstructural complexity and the morphological variability of the interface lead to the impossibility to reach an analytical solution.

Therefore, the volume averaging method is introduced to treat the microscopic thermophysical problem from a macroscopic point of view. Equations are then derived over a volume dV, defined so that its shape, size and orientation are independent from the position in space and time. In the same way areas dA are defined. This process leads to the definition of macroscopic quantities for each phase, considering each element dV as a physical point.

Hence, the volume on which quantities are mediated must be representative of the domain microscopic structure: this leads to the definition of *Representative Ele-*

mentary Volume (REV) and *Representative Elementary Area* (REA). A volume can be considered representative of the whole domain only if its characteristic dimension (D) satisfies the following inequality:

$$l \ll D \ll L \tag{2.3}$$

where l is the microscopic dimensional scale of the porous matrix, and L is the dimension of macroscopic inhomogeneities. Considering $\mathbf{x}$ as the center of gravity of the volume dV and ξ as the relative distance of a single particle from the volume center of gravity, it is possible to define the phases volume fraction γ (not defined on the interface $\alpha\beta$):

$$\gamma_\alpha = \gamma_\alpha(\mathbf{x}+\xi, t) = \begin{cases} 1 \text{ if } (\mathbf{x}+\xi) \in V_\alpha \\ 0 \text{ if } (\mathbf{x}+\xi) \in V_\beta \end{cases} \tag{2.4}$$

Eq. (2.4) can be integrated to evaluate the volume, or area, fraction of α-phase inside dV or dA (dV_α e dA_α):

$$dV_\alpha(\mathbf{x}+\xi, t) = \int_{dV} \gamma_\alpha(\mathbf{x}+\xi, t)dv \tag{2.5}$$

$$dA_\alpha(\mathbf{x}+\xi, t) = \int_{dA} \gamma_\alpha(\mathbf{x}+\xi, t)da \tag{2.6}$$

Moreover, Eq. (2.4) is useful to simplify the volume integral calculation of a

generic function h over dV_α, which is the part of dV occupied by the phase α:

$$\int_{dV_\alpha} h dv = \int_{dV} h\gamma_\alpha dv \tag{2.7}$$

It is also possible to define the volume fraction of phases as:

$$\varepsilon_\alpha(\mathbf{x}+\xi,t) = \frac{dV_\alpha}{dV} = \frac{1}{dV}\int_{dV} \gamma_\alpha(\mathbf{x}+\xi,t)dv \tag{2.8}$$

that is called *porosity* (ε) when it is evaluated on the fluid phase. We have also to remember that the sum of volume fractions of all phases must be equal to one, while for each phase it is defined between 0 and 1.

The specific surface related to the generic phase (e.g. the fluid phase), will be then defined as the ratio between the phase internal area and the volume dV:

$$S_\alpha(\mathbf{x}+\xi,t) = \frac{\sum_{\alpha\neq\beta} S_{\alpha\beta}}{dV} = \frac{1}{dV} = \frac{1}{dV}\sum_{\alpha\neq\beta}\int_{dA_{\alpha\beta}} dA \tag{2.9}$$

Now, for the generic equation h we can define following average operators:

1. *volume average operator* - $\langle \quad \rangle_\alpha$

$$\langle h\rangle_\alpha(\mathbf{x}+\xi,t) = \frac{1}{dV}\int_{dV} h(\mathbf{x}+\xi,t)\gamma_\alpha(\mathbf{x}+\xi,t)dv \tag{2.10}$$

2. *intrinsic volume average operator* - $\langle \quad \rangle_\alpha^\alpha$

$$\langle h\rangle_\alpha^\alpha(\mathbf{x}+\xi,t) = \frac{1}{dV_\alpha(\mathbf{x}+\xi,t)}\int_{dV} h(\mathbf{x}+\xi,t)\gamma_\alpha(\mathbf{x}+\xi,t)dv \tag{2.11}$$

3. *mass average operator* - $\bar{}^{\,\alpha}$

$$\begin{aligned}\bar{h}^{\alpha}(\mathbf{x}+\xi,t) &= \frac{\int_{dV}\rho(\mathbf{x}+\xi,t)h(\mathbf{x}+\xi,t)\gamma_{\alpha}(\mathbf{x}+\xi,t)dv}{\int_{dV}\rho(\mathbf{x}+\xi,t)\gamma_{\alpha}(\mathbf{x}+\xi,t)dv} = \\ &= \frac{1}{\langle\rho\rangle_{\alpha}(\mathbf{x}+\xi,t)dV}\int\limits_{dV}\rho(\mathbf{x}+\xi,t)h(\mathbf{x}+\xi,t)\gamma_{\alpha}(\mathbf{x}+\xi,t)dv\end{aligned} \tag{2.12}$$

4. *areal average operator* - $\hat{}^{\,\alpha}$

$$\hat{h}^{\alpha}(\mathbf{x}+\xi,t) = \frac{1}{dA}\int\limits_{dA}\mathbf{h}(\mathbf{x}+\xi,t)\cdot\underline{n}\gamma_{\alpha}(\mathbf{x}+\xi,t)da \tag{2.13}$$

Starting from Eqs. (2.10) and (2.11), it is possible to obtain, using Eq. (2.8) too, the following relation between volume average and intrinsic volume average:

$$\langle h\rangle_{\alpha} = \varepsilon_{\alpha}\langle h\rangle_{\alpha}^{\alpha} \tag{2.14}$$

In order to obtain the average of a general balance equation of a phase, it is possible to switch from microscopic to macroscopic quantities integrating microscopic equations over the three-dimensional domain V. This can be done taking into account previous definitions:

$$\begin{aligned}\int\limits_{V}\left[\frac{1}{dV}\int\limits_{dV_{\alpha}}h(\mathbf{x}+\xi,t)dv_{\xi}\right]dV_x &= \int\limits_{V}\left[\frac{1}{dV}\int\limits_{dV}h\gamma_{\alpha}dv_{\xi}\right]dV_x \equiv \\ &\equiv \int\limits_{V}\int\limits_{dV}h\gamma_{\alpha}dv = \int\limits_{V}\langle h\rangle_{\alpha}dV\end{aligned} \tag{2.15}$$

The same can be done for the edge A:

$$\int_A \left[\frac{1}{dA} \int_{dA_\alpha} h\gamma_\alpha da_\xi \right] dA_x \quad or \quad \int_A \left[\frac{1}{dA} \int_{dA_\alpha} \mathbf{h} \cdot \underline{n}\gamma_\alpha da_\xi \right] dA_x \equiv \equiv \int_A \int_{dA} \mathbf{h} \cdot \underline{n}\gamma_\alpha da = \int_A \hat{h}^\alpha dA \tag{2.16}$$

In Eq. (2.15) and (2.16) after the symbol $\equiv$ contracted forms are reported, which will be used hereafter for sake of shortness.

Below, some theorems about the mean values, integral and partial derivative over space or time of the function h are reported:

- *Theorem II* - time derivative integration

$$\int_V \int_{dV} \frac{\partial h}{\partial t} \gamma_\alpha dv = \int_V \frac{\partial}{\partial t} \int_{dV} h\gamma_\alpha dv - \int_V \sum_{\beta \neq \alpha} \int_{dA_{\alpha\beta}} h\mathbf{w} \cdot \underline{n}^{\alpha\beta} da \tag{2.17}$$

- *Theorem III* - space derivative integration

$$\int_V \int_{dV} (\nabla \cdot \mathbf{h}) \gamma_\alpha dv = \int_V \int_{dV} \nabla \cdot (\mathbf{h}\gamma_\alpha) dv + \int_V \sum_{\beta \neq \alpha} \int_{dA_{\alpha\beta}} \mathbf{h} \cdot \underline{n}^{\alpha\beta} da \tag{2.18}$$

- *Theorem IV* - modified form of the Gauss Theorem

$$\begin{aligned} \int_V \nabla \cdot \int_{dV} \mathbf{h} dv = \int_V \int_{dV} \nabla \cdot \mathbf{h} dv = \int_A \int_{dA} \mathbf{h} \cdot \underline{n} da \\ \Rightarrow \int_V \int_{dV} (\nabla \cdot \mathbf{h}) \gamma_\alpha dv = \int_A \int_{dA} (\mathbf{h} \cdot \underline{n}) \gamma_\alpha da + \int_V \sum_{\beta \neq \alpha} \int_{dA_{\alpha\beta}} \mathbf{h} \cdot \underline{n}^{\alpha\beta} da \end{aligned} \tag{2.19}$$

Finally, we can define the local value of a function h, referred to the phase α, as the local sum of the volume average ($\langle \quad \rangle_\alpha$) and the local deviation from the volume average ($\tilde{\ }^\alpha$):

$$h = \langle h \rangle_\alpha + \tilde{h}^\alpha \tag{2.20}$$

2.3 Fluid mechanics analysis

The first study of the relation between the fluid velocity, flowing through a porous medium, and the pressure drop has been performed by Darcy (1856) and led to the following equation:

$$-\frac{dp}{dx} = \frac{\mu}{K} u_D \tag{2.21}$$

where μ is the air dynamic viscosity (in $Pa \cdot s$) and K is the air permeability (in m^2), which is a parameter describing the solid matrix. Finally, u_D is the "Darcean velocity" (or filter velocity), which is determined by dividing the mass flow-rate by the product of the fluid density (which is assumed to be incompressible) and the cross-sectional area of the porous layer. In this way, a linear relationship is stated, which is typical for a Stokes flow. This leads to a deviation of the actual flow from Eq. (2.21) at high velocities.

Solid matrices can be divided in *isotropic* and *anisotropic* media: in the first case, pressure gradient and velocity vector are parallel, giving the following equation:

$$-\frac{dp}{dx} = \frac{\mu}{K} \mathbf{u_D} \tag{2.22}$$

For anisotropic media, pressure gradient and velocity vector are not parallel. This gives the following tensorial notation:

$$-\frac{dp}{dx} = \frac{\mu}{\mathbf{K}}\mathbf{u_D} \tag{2.23}$$

where $\mathbf{K}$ is the following second-order symmetric ($K_{ij} = K_{ji}$) tensor.

$$\mathbf{K} = \begin{bmatrix} K_{11} & K_{12} & K_{13} \\ K_{21} & K_{22} & K_{23} \\ K_{31} & K_{32} & K_{33} \end{bmatrix} \tag{2.24}$$

More in general, permeability is a measure of the flow conductance of the matrix, and is a synthetic description of the pore structure, which is highly variable. This consideration leads to the need of mathematical models to describe the microscopic geometry and its effects on the fluid dynamic behavior [20].

Capillary models: the Navier-Stokes equation is applied to flow in small-diameter conduits, which can be divided in two categories: parallel/series conduits and network of conduits. The reliability of this model is limited to simple and regular structures.

Hydraulic radius model: the hydraulic diameter is defined as

$$d_h = \frac{4\varepsilon}{A_0(1-\varepsilon)}$$

where A_0 is the volumetric surface area (equal to A_{fs}/V_s). This model gives a relationship between permeability and hydraulic diameter, as a function of

the capillary cross-section shape (circular, rectangular, elliptical, etc.).

Local volume average: the procedure described in §2.2 is applied to the Navier-Stokes equation for the fluid phase of the REV. This approach introduces a large number of unknown, coming from the complexity of the flow paths and the interpore and pore-to-pore fluid dynamic interaction. Therefore, empiricism at various level is mandatory to complete volume-averaged conservation equations (mass and momentum). This method leads to the following equation:

$$\rho_0 \left[\frac{\partial \langle \mathbf{u} \rangle}{\partial t} + \langle \mathbf{u} \cdot \nabla \mathbf{u} \rangle \right] = -\nabla \langle P - p_0 \rangle + \mu \nabla^2 \langle \mathbf{u} \rangle - \frac{\varepsilon \mu}{d^2 k_s} \langle \mathbf{u} \rangle \tag{2.25}$$

where d is the characteristic length at the pore scale, k_s is a nondimensional function of porosity and P is the combined effect of pressure p and the body force per unit volume exerted by the fluid on the pore walls. However, this method has not been implemented in this work.

Semiheuristic momentum equation: this approach has been introduced to have a set of of governing equations that can describe both the momentum transport through porous media (K is small) as well as that in plain media (K is very large). This equation is substantially an extension of the Darcy law in

Eq. (2.21), based on the application of local volume averaging:

$$\underbrace{\frac{\rho}{\varepsilon}\left(\frac{\partial \mathbf{u}_D}{\partial t}+\mathbf{u}_D\cdot\nabla\mathbf{u}_D\right)}_{\substack{\text{macroscopic inertial force or macroflow-development term}}} = \underbrace{-\nabla\langle p\rangle^f}_{\substack{\text{pore pressure gradient}}} + \underbrace{\rho\mathbf{f}}_{\substack{\text{body force}}} +$$

$$+ \underbrace{\frac{\mu}{\varepsilon}\nabla^2\mathbf{u}_D}_{\substack{\text{macroscopic or bulk viscous shear stress diffusion (Brinkman viscous term or bounding surface effect)}}} - \underbrace{\frac{\mu}{K}\mathbf{u}_D}_{\substack{\text{microscopic viscous shear stress,(Darcy term)}}} - \underbrace{\frac{C_E}{K^{1/2}}\rho\left|\mathbf{u}_D\right|\mathbf{u}_D}_{\substack{\text{microscopic inertial force (Ergun inertial term or micro-flow development term)}}} \tag{2.26}$$

where C_E is Ergun coefficient, which is a form-drag constant [20–22]

In the work under discussion, the semiheuristic momentum equation (2.26) has been implemented, after the introduction of some simplifications. First of all, Eq. (2.26) has been reduced to a one-dimensional domain, becoming:

$$\frac{\rho}{\varepsilon}\left(\frac{\partial u_D}{\partial t}+u_D\frac{\partial u_D}{\partial x}\right) = -\frac{\partial\langle p\rangle^f}{\partial x}+\rho\mathbf{f}+\frac{\mu}{\varepsilon}\frac{\partial^2 u_D}{\partial x^2}-\frac{\mu}{K}u_D-\frac{C_E}{K^{1/2}}\rho\left|u_D\right|u_D. \tag{2.27}$$

The assumption of one-dimensional domain, applied to the continuity equation, leads to:

$$\nabla\cdot\mathbf{u}_D=0\Rightarrow\frac{\partial u_D}{\partial x}=0 \quad \forall x. \tag{2.28}$$

This means that also the second order space derivative is equal to zero.

The Eq. (2.27) has then been simplified by applying the Eq. (2.28) and neglecting

every body-force effect. Finally, we obtain:

$$\frac{\rho}{\varepsilon}\frac{\partial u_D}{\partial t} = -\frac{\partial \langle p \rangle^f}{\partial x} - \frac{\mu}{K}u_D - \frac{C_E}{K^{1/2}}\rho\left|u_D\right|u_D \tag{2.29}$$

Hence, Eq.(2.29) has been used in this work. In the following chapters the discretization of Eq. (2.29), and the experimental and numerical derivation of quantities (i.e. permeability and Ergun coefficient) are presented.

2.4 Heat transfer analysis

As far as the heat transfer phenomenon is concerned, the volume average approach has been applied to the internal energy equation, taking into account a two-phase domain, divided in a solid (s) and a fluid (f), which are the solid matrix of a porous media and the flowing air respectively.

Assuming a stationary, laminar and fully developed velocity field, neglecting heat sources or sinks, we can define an energy equation for each phase in the domain and a boundary condition on the interface A_{fs} (Figure 2.1), according to the procedure presented in [20]:

$$(\rho c_p)_f\left(\frac{\partial T_f}{\partial t} + \mathbf{u}_f \cdot \nabla T_f\right) = \nabla \cdot \lambda_f \nabla T_f \quad \text{in } V_f \tag{2.30}$$

$$(\rho c)_s\frac{\partial T_s}{\partial t} = \nabla \cdot \lambda_s \nabla T_s \quad \text{in } V_s \tag{2.31}$$

$$T_f = T_s, \quad \underline{n}_{fs} \cdot \lambda_f \nabla T_f = \underline{n}_{fs} \cdot \lambda_s \nabla T_s \quad \text{on } A_{fs} \tag{2.32}$$

According to Eq. (2.20), we can divide temperature and velocity in local volume average and deviation:

$$T_f = \langle T_f \rangle_f + \tilde{T}^f \tag{2.33}$$

$$T_s = \langle T_s \rangle_s + \tilde{T}^s \tag{2.34}$$

$$\mathbf{u}_f = \langle \mathbf{u}_f \rangle_f + \tilde{\mathbf{u}}^f \tag{2.35}$$

Using Eqs. (2.33), (2.34) and (2.35) and the average volume approach, the partial differential equation will become:

$$(\rho c_p)_f \left(\frac{\partial \langle T \rangle_f}{\partial t} + \langle \mathbf{u} \rangle_f \cdot \nabla \langle T \rangle_f \right) = \nabla \cdot \left(\lambda_f \nabla \langle T \rangle_f + \frac{\lambda_f}{V_f} \int\limits_{A_{fs}} \underline{n}_{fs} \tilde{T}_f dA \right) - (\rho c_p)_f \nabla \left\langle \tilde{\mathbf{u}} \tilde{T} \right\rangle_f + \frac{1}{V_f} \int\limits_{A_{fs}} \underline{n}_{fs} \cdot \lambda_f \nabla \tilde{T}_f dA \tag{2.36}$$

$$(\rho c)_s \frac{\partial \langle T \rangle_s}{\partial t} = \nabla \cdot \left(\lambda_s \nabla \langle T \rangle_s + \frac{\lambda_s}{V_s} \int\limits_{A_{fs}} \underline{n}_{sf} \tilde{T}_s dA \right) + \frac{1}{V_s} \int\limits_{A_{fs}} \underline{n}_{sf} \cdot \lambda_s \nabla \tilde{T}_s dA \tag{2.37}$$

while for the boundary condition over the interface we will have:

$$\begin{aligned} \tilde{T}_f &= \tilde{T}_s + \left(\langle T \rangle_s - \langle T \rangle_f \right) \\ \underline{n}_{fs} \cdot \lambda_f \nabla \tilde{T}_f &= \underline{n}_{fs} \cdot \lambda_s \nabla \tilde{T}_s + \underline{n}_{fs} \cdot \left(\lambda_s \langle T \rangle_s - \lambda_f \langle T \rangle_f \right) \end{aligned} \tag{2.38}$$

For the sake of brevity, we omit the mathematical manipulations, as well as the conservation equations related to local disturbances of temperature for the two phases, referring to [20] for more information.

The problem can be further simplified. Performing an order of magnitude analysis, it is possible to introduce the hypothesis of local thermal equilibrium:

- Time scale t will have to respect

$$\frac{\varepsilon(\rho c)_f l^2}{t} \left(\frac{1}{\lambda_f} + \frac{1}{\lambda_s} \right) \ll 1 \quad \text{and} \quad \frac{(1-\varepsilon)(\rho c)_s l^2}{t} \left(\frac{1}{\lambda_f} + \frac{1}{\lambda_s} \right) \ll 1 \tag{2.39}$$

- Space scale l will have to respect

$$\frac{\varepsilon \lambda_f l}{A_0 L^2} \left(\frac{1}{\lambda_f} + \frac{1}{\lambda_s} \right) \ll 1 \quad \text{and} \quad \frac{(1-\varepsilon) \lambda_s l}{A_0 L^2} \left(\frac{1}{\lambda_f} + \frac{1}{\lambda_s} \right) \ll 1 \tag{2.40}$$

where A_0 is the specific area. If inequalities (2.39) and (2.40) are fulfilled, it is possible to assume the validity of the hypothesis of local thermal equilibrium, which leads to:

$$\langle T \rangle_f = \langle T \rangle_s = \langle T \rangle \tag{2.41}$$

By applying the Eq. (2.8) to the fluid phase, we will have $\varepsilon_f = \varepsilon \equiv$ *porosity* and, consequently, $\varepsilon_s = 1 - \varepsilon$. Summing Eq. (2.36) and (2.37), introducing the interface

condition ($\underline{n}_{fs} = -\underline{n}_{sf}$), we will find the following macroscopic energy equation for the porous media:

$$[\epsilon(\rho c_p)_f + (1-\epsilon)(\rho c)_s] \frac{\partial \langle T \rangle}{\partial t} + (\rho c_p)_f \langle \mathbf{u} \rangle \nabla \langle T \rangle = \nabla \cdot \underline{\underline{\lambda}}_{eff} \cdot \nabla \langle T \rangle \tag{2.42}$$

$$\tilde{T}_f = \tilde{T}_s = \tilde{T}, \quad -\underline{n} \cdot \nabla \tilde{T} = \underline{n} \cdot \nabla \langle T \rangle \quad su \quad A_{fs} \tag{2.43}$$

Furthermore, we have to underline that in V_f and V_s local temperature deviations $\tilde{T}^f$ and $\tilde{T}^s$ do not have the same value. In Eq. (2.42) the effective conductivity tensor $\underline{\underline{\lambda}}_{eff}$ depends on the thermal tortuosity tensor $\underline{\underline{\lambda}}_{tor}$ and the thermal dispersion tensor $\underline{\underline{\lambda}}_{disp}$:

$$\underline{\underline{\lambda}}_{eff} = [\epsilon \lambda_f + (1-\epsilon)\lambda_s] \mathbf{I} + \underline{\underline{\lambda}}_{tor} + \underline{\underline{\lambda}}_{disp} \tag{2.44}$$

$$\underline{\underline{\lambda}}_{tor} \cdot \nabla \langle T \rangle = \frac{\lambda_f - \lambda_s}{\Delta V} \int_{A_{sf}} \underline{n}_{sf} \tilde{T} dA \tag{2.45}$$

$$\underline{\underline{\lambda}}_{disp} \cdot \nabla \langle T \rangle = \frac{(\rho c_p)_f}{\Delta V} \int_{V_f} \tilde{\underline{u}}^f \tilde{T}^f dV \tag{2.46}$$

2.5 Conclusions

In this Chapter, we have introduced the theoretical background supporting the study under discussion. Equations for both fluid dynamic and heat transfer in

porous media have been defined, together with main quantities which affect these problems.

The velocity field in the fluid phase of a porous medium is described by Eq. (2.29). This means that we have to evaluate both permeability and Ergun coefficient, for the different materials involved.

A similar issue has been risen in the heat transfer treatment, described by Eq. (2.42), where a corrected value of thermal conductivity appears. Considering Eq. (2.44), (2.45) and (2.46), the differential problem needs another set of equations to be solved, in order to calculate the spatial distribution of local deviations from the volume average value of temperature and velocity. Several approaches to the *closure problem* have been found in literature, aimed at the numerical or analytical evaluation of effective properties [23–29]. Since equations depend on the domain microstructure, which is highly variable, we have decided to numerically evaluate $\underline{\underline{\lambda}}_{tor}$ and $\underline{\underline{\lambda}}_{disp}$, simulating the fluid-dynamic problem over a REV, and correlating the solution with macroscopic parameters, with an approach similar to the one used in [26].

Following chapters deal with the characterization of fibrous insulation and permeable concrete from both fluid mechanics and heat transfer points of view, by means of numerical simulations and laboratory tests.

Chapter 3

Fibrous insulating materials characterization

In this Chapter, the characterization of fibrous insulation materials is presented. More in detail, the volume averaging technique has been applied to a geometrical simplification of an elementary cell and, by means of CFD simulations, thermal tortuosity, dispersion and air permeability have been derived as a function of macroscopic parameters, such as porosity and Peclet number (defined as $u_x \cdot \frac{L_{REV}(\rho c_p)_f}{\lambda_f}$ when referred to REV dimension).

The elementary volume has been modeled as an ordered array of longitudinally-displaced cylinders, representing rock wool fibers (the elementary cell); temperature distribution and velocity field have been calculated for six levels of porosity, five average inlet air velocity and two temperature gradient along the x-axis, for both *pro* and *contra-flux* conditions.

Numerical results have been processed and used to define regression equations

for thermal tortuosity, dispersion and to correlate pressure drop with average air velocity.

It is important to notice that this particular analysis has been performed to test the reliability of the volume average method to the problem under discussion. For this reason, all randomness of the solid matrix have been neglected. A more detailed geometrical characterization have been done for pervious concrete, as described in the next Chapter.

3.1 Domain definition and numerical model

The definition of the *REV* (Figure 3.1) has been done approximating the solid matrix of rock wool as an array of parallel cylinders, orthogonally displaced to the two-dimensional CFD simulation plane. The dimension of the *REV* side (L_{REV}) has been calculated as a function of porosity, keeping constant the solid cylinders diameter (5 μm). Thus, six *REV*s have been defined for six values of porosity (ε = 50%, 80%, 85%, 90% 95% and 99%). Keeping in mind that fibrous insulating materials in buildings are characterized by high porosity values (generally greater than 90% for commercial materials), lower values of this parameter have been taken into account only to reach more general correlations for thermal dispersion and tortuosity.

Thermophysical properties of the materials used for simulations are listed in Table 3.1. Since this work deals with building material like rock wool, dolomitic rock properties have been used to describe the solid matrix.

Energy and momentum equations have been solved over the fluid and the solid

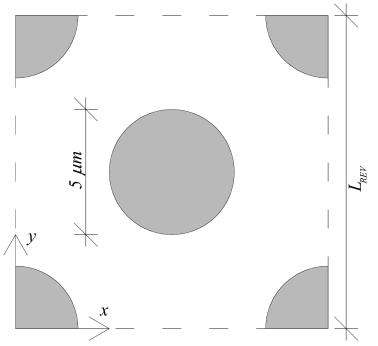

Figure 3.1: Geometrical approximation of a representative elementary volume of a transversal section of a fibrous insulating material, based on an array of solid cylinders.

Table 3.1: Thermophysical properties of fluid and solid matrix used in CFD simulations.

Fluid: Air	
Density - ρ_f	1.225 kg/m^3
Conductivity - λ_f	0.024 W/mK
Specific Heat - $c_{p,f}$	1006 J/kgK
Solid: Dolomitic Rock	
Density - ρ_s	2870 kg/m^3
Conductivity - λ_s	1.75 W/mK
Specific Heat - $c_{p,s}$	910 J/kgK

phases in steady-state conditions, using a finite volume discretization method. There was no need for a viscous model, because of the low Re condition, resulting from low values of inlet air velocity. This condition leads also to low values of Pe number.

3.2 Boundary conditions

Dealing with boundary conditions, five steps of average inlet velocity have been applied to the inlet section on the unit-cell left side. Pe number has been successively calculated using the mean volume value of the x component of velocity. A temperature gradient has been imposed over the x coordinate, keeping its value constant along the y-axis: temperature values have been given for the left side,

both for the solid wall and the inlet fluid. Since the fluid part of the unit-cell right side is an outlet boundary condition, it was not possible to assign any temperature value. This problem has been solved by extending five times the elementary cell over the x direction and imposing the temperature value on the solid part of the right side (Figure 3.2).

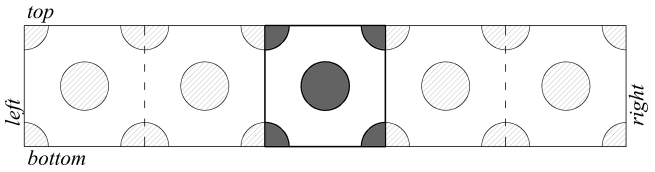

Figure 3.2: Definition of the calculus domain for CFD simulations. Results on central elementary cell have been used for thermal tortuosity and dispersion evaluation.

Table 3.2: Boundary conditions for the numerical solution of the velocity field.

Inlet mean velocity	u_a	u_b	u_c	u_d	u_e
$\bar{u}_{in}$ $[m/s]$	0.001	0.003	0.005	0.007	0.01

Table 3.3: Boundary conditions for the numerical solution of the temperature distribution.

Temp. diff.	porosity (ε)					
over the x-axis	50%	80%	85%	90%	95%	99%
ΔT_1 $[K]$	0.080	0.125	0.146	0.176	0.250	0.560
ΔT_2 $[K]$	0.402	0.625	0.729	0.878	1.250	2.798

As will be later discussed, for every simulation, temperature distribution along the y-axis has been checked on the left and right sides of the central *REV*. The aim was to verify that the y-component of the temperature gradient was always negligible on the edges. Symmetry condition has been taken into account for both top and bottom faces of the computational domain. Values of boundary conditions are listed in Table 3.2 and 3.3. The simulation of *pro-flux* and *contra-flux* configurations have been performed reverting temperature values of left and right faces.

3.3 Results and discussion

An amount of 120 simulations has been performed, 60 for both *pro* and *contra-flux* conditions. Results have been postprocessed to calculate macroscopic parameter for fluid dynamic and heat transfer.

3.3.1 Fluid dynamic

For what concerns the relationship between average air velocity and pressure drop across a fibrous insulation layer of a permeable wall, CFD simulations results have been used to evaluate permeability coefficient K and C_E in Eq. (2.29). For this reason, average air velocity in a REV (as represented in Figure 3.1) and average pressure drop between left and right sides have been plotted for different porosity values and velocity boundary conditions (Figure 3.3).

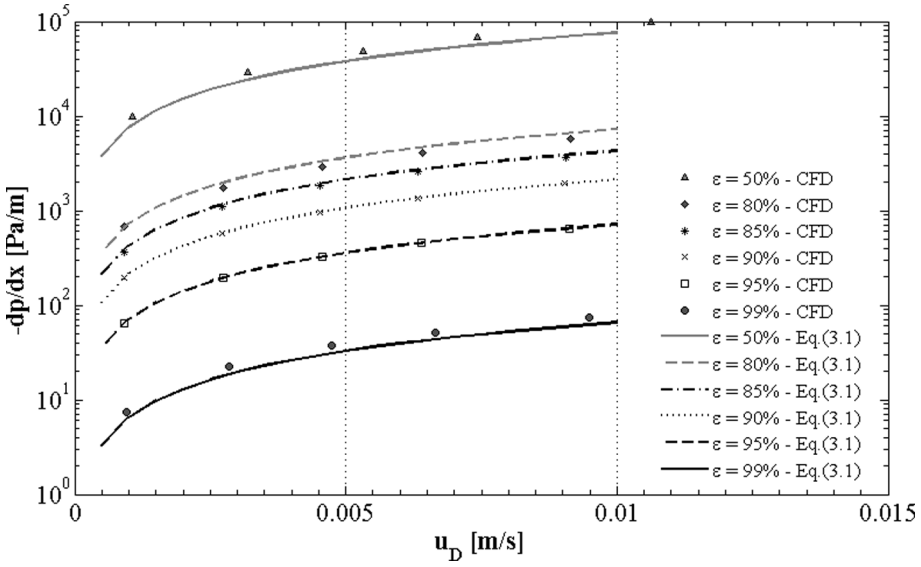

Figure 3.3: Pressure loss as a function of average inlet air velocity, for different values of porosity.

Going more in detail, a linear relationship has been found between average fluid velocity inside the REV and the pressure drop across it, for each porosity value.

This means that the Eq. (2.29) degenerates into the Darcy equation. Hence, the μ/K coefficient dependence on the fluid volume fraction ε has been investigated, by means of a heuristic approach: first of all, we have assumed that the pressure loss is negligible for the maximum value of porosity (completely fluid domain $\Rightarrow \varepsilon = 1$).

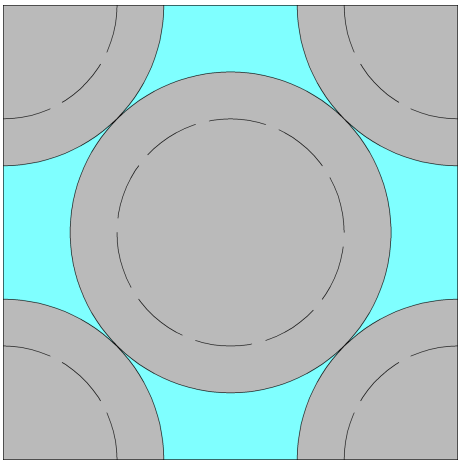

Figure 3.4: Graphical representation of the limit-porosity geometrical configuration.

Secondly, we have hypothesized that pressure loss tends to infinity as porosity tends to a limit value, which implies the contact between adjacent fibers, as represented in Figure 3.4, and the interruption of free channels for the fluid motion (approximately we have $\varepsilon_{lim} \cong 0.2146$). The regression equation obtained is then (Figure 3.3):

$$-\frac{dp}{dx} = 70.74 \left[\frac{1-\varepsilon}{5.527 \cdot 10^{-4} \left(\varepsilon - \varepsilon_{lim}\right)} \right]^{1.437} \cdot u_D \tag{3.1}$$

3.3.2 Heat transfer

Ignoring the two-dimensional behavior, thermal tortuosity and dispersion, which have been defined in Eqs. (2.45) and (2.46), have been calculated on the x coordi-

nate, using the following discretized form:

$$\lambda_{tor,xx} \approx \frac{(\lambda_f - \lambda_s)/V_{REV}}{\Delta \langle T \rangle_x / L_{REV}} \int_{A_{sf}} n_{sf,x} \left(T - \langle T \rangle\right) dA \tag{3.2}$$

$$\lambda_{disp,xx} \approx \frac{(\rho c_p)_f / V_{REV}}{\Delta \langle T \rangle_x / L_{REV}} \int_{V_f} \left(u - \langle u \rangle\right) \left(T - \langle T \rangle\right) dV \tag{3.3}$$

where u is the x component of the local velocity vector. In fact, considering a multidimensional heat transfer phenomenon, thermal dispersion and tortuosity are written in a tensorial form. If our analysis of the building envelope is restricted to a one-dimensional problem, which is normally enough to describe the thermal behavior of a dynamic insulation system (heat flux and air flow are generally transversal to the wall section, while solid fibers statistically lie on the wall plane), the number of dimensions considered for thermal tortuosity and dispersion can be reduced to one.

The closure problem, which comes from the need for a set of equations to describe the spatial distribution of local deviations, have been solved using numerical results of CFD simulations for velocity and temperature fields, according to the method proposed in [26]. For example, in Figure 3.5 representations of thermal and velocity fields are reported, for $\varepsilon = 95\%$, $\bar{u}_{in} = u_e$ and ΔT_1 in *contra-flux* condition (only the central elementary cell of the computational domain has been used and represented - Figure 3.5).

Before starting the postprocessing phase, the assumption consistency of constant temperature conditions along the y-axis for left and right faces of the central *REV* has been verified: in Figure 3.6(a) the horizontal distribution of temperature

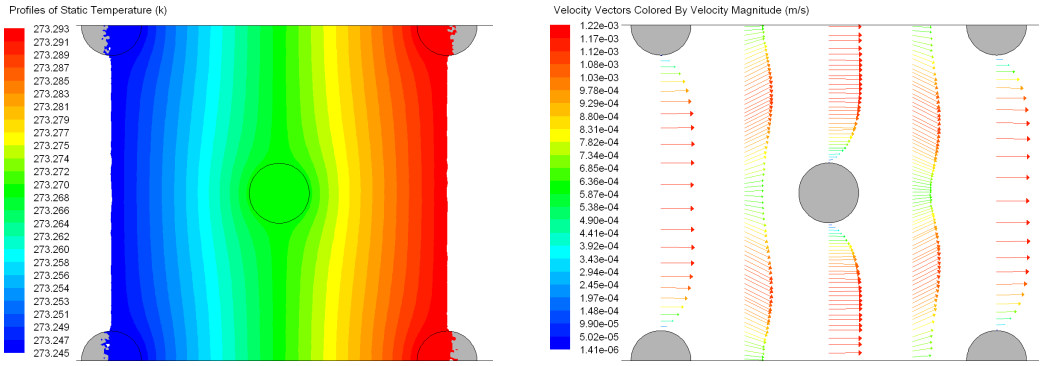

(a) (b)

Figure 3.5: Temperature (a) and velocity (b) fields representation, obtained by means of a CFD simulation of a unit-cell with $\varepsilon = 95\%$, $\bar{u}_{in} = u_a$ and ΔT_1 (*contra-flux* condition).

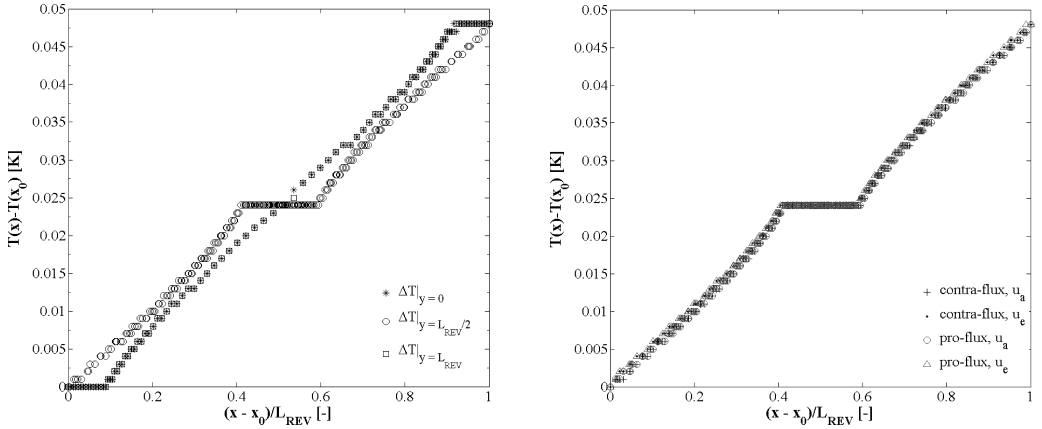

(a) (b)

Figure 3.6: Temperature field analyses. (a) Comparison among horizontal temperature gradients at different y values for the $\varepsilon = 95\%$ unit-cell ($\bar{u}_{in} = u_a$, ΔT_1) in *contra-flux* condition. (b) Comparison among horizontal temperature gradients at $y = L_{REV}/2$ ($\varepsilon = 95\%$, ΔT_1) for different average inlet velocities (u_a and u_e) and working conditions (*pro* and *contra-flux*).

is represented for three levels of ordinate values ($y = 0$, $y = L_{REV}/2$ and $y = L_{REV}$). Comparing the three curves, we can observe that for $x = 0$ and $x = L_{REV}$ (graph abscissa) temperature values seem to be coincident along the y direction. This analysis has confirmed that horizontal temperature gradient can be considered independent from the vertical coordinate for the central REV.

In Figure 3.6(b), temperature values at $y = L_{REV}/2$ are reported for extreme

values of average inlet velocity and for *pro* and *contra-flux* working conditions at ΔT_1: a negligible effect of velocity field on the temperature distribution can be observed, perhaps as a result of the low Peclet condition.

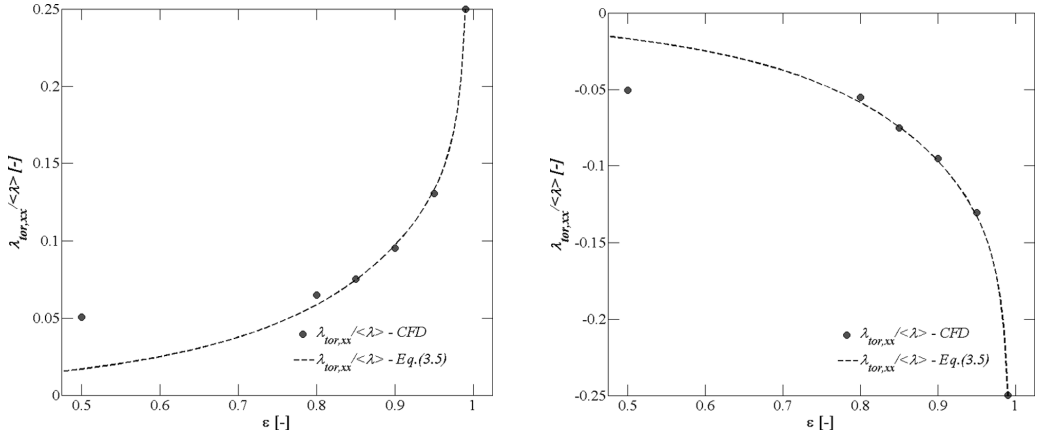

(a) *pro-flux* (b) *contra-flux*

Figure 3.7: Comparison between numerical results and regression curves for the tortuosity coefficient $\lambda_{tor,xx}/\langle\lambda\rangle$ for *pro* (a) and *contra-flux* (b) conditions.

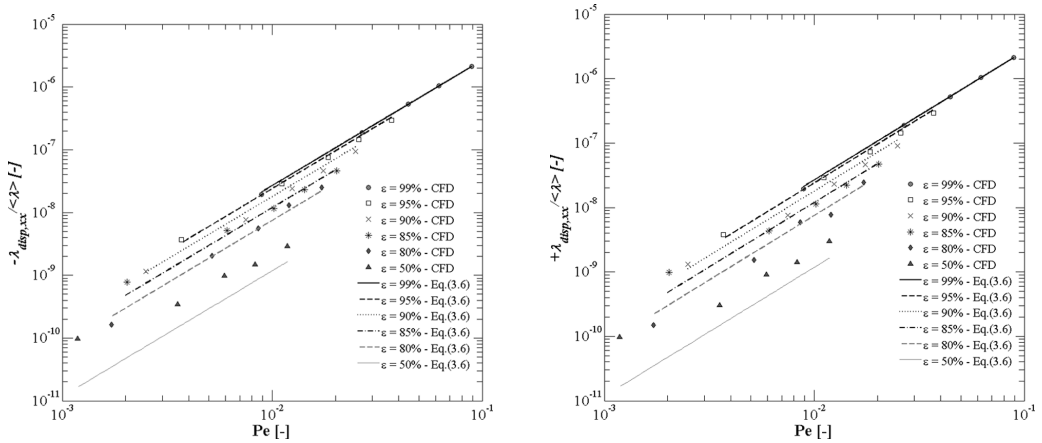

(a) *pro-flux* (b) *contra-flux*

Figure 3.8: Comparison between numerical results and regression curves for the dispersion coefficient $\lambda_{disp,xx}/\langle\lambda\rangle$ for *pro* (a) and *contra-flux* (b) conditions.

Starting from the assumption that both thermal tortuosity and dispersion are dependent on parameter like porosity, horizontal temperature gradient and Peclet number, it has been possible to evaluate two regression equations based on numerical

results of CFD simulations. In Figure 3.7 and 3.8 both quantities are represented as a fraction of the average thermal conductivity of the *REV* calculated as follows:

$$\langle\lambda\rangle = \varepsilon \cdot \lambda_f + (1-\varepsilon) \cdot \lambda_s \tag{3.4}$$

Interpolating equations for both these ratios are:

$$\frac{\lambda_{tor,xx}}{\langle\lambda\rangle} \approx \mp \frac{-4.263 \cdot \varepsilon + 3.965 \cdot \varepsilon^{10.5}}{1 - 290.5 \cdot \varepsilon - (1-290.5) \cdot \varepsilon^{0.1}} \tag{3.5}$$

$$\frac{\lambda_{disp,xx}}{\langle\lambda\rangle} \approx \pm 2.675 \cdot 10^{-4} \cdot Pe_H^2 \cdot e^{100\varepsilon^2 \cdot \left[\frac{(1-\varepsilon)^2}{2}\right]} \tag{3.6}$$

These two parameters are analyzed separately.

Table 3.4: Results of thermal tortuosity calculation. For every porosity level and every working configuration minimum and maximum values are reported. Arithmetic mean (μ) and standard deviation (σ) are given.

Config.	ε	Min.	Max.	μ	σ
pro	50%	4.98%	5.10%	5.04%	0.04%
	80%	6.16%	6.81%	6.48%	0.31%
	85%	7.48%	7.54%	7.50%	0.02%
	90%	9.50%	9.55%	9.52%	0.01%
	95%	13.02%	13.09%	13.06%	0.02%
	99%	24.65%	25.29%	25.00%	0.22%
contra	50%	-5.11%	-5.01%	-5.05%	0.03%
	80%	-5.84%	-5.15%	-5.51%	0.32%
	85%	-7.54%	-7.49%	-7.52%	0.02%
	90%	-9.59%	-9.50%	-9.53%	0.02%
	95%	-13.08%	-13.02%	-13.05%	0.02%
	99%	-25.26%	-24.65%	-24.99%	0.21%

The thermal tortuosity (Figure 3.7) seems to be affected only by the material porosity, while it shows little sensitiveness to different values of horizontal thermal gradient and Pe number (Table 3.4). For this reason, results obtained for the

same value of porosity, but different ΔT_x and $\bar{u}_{in}$, have been summarized with their mean value (six points for each working condition). Moreover, the trend of data seems to suggest a symmetry respect to the abscissa axis, for opposite working conditions (*pro* and *contra-flux*). Indeed, when air flow and thermal flux have the same direction, thermal tortuosity gives a positive contribution to effective thermal conductivity; while it decreases $\lambda_{eff,xx}$ in *contra-flux* condition. Furthermore, its relevance increases for higher values of porosity, which are typical for fibrous insulating material in buildings (rock wool porosity is between 90% and 99%, depending on bulk density): within this porosity range, thermal tortuosity is approximately between the $\mp$9.5% and the $\mp$25% of the average thermal conductivity, as defined in Eq. (3.4).

Table 3.5: Comparison among different thermal dispersion values depending on temperature difference between left and right edge of the considered *REV*.

ε	$\bar{u}_{in}$ $[m/s]$		$\frac{\lambda_{disp,xx}}{\langle\lambda\rangle}\Big\vert_{\Delta T_1}$	$\frac{\lambda_{disp,xx}}{\langle\lambda\rangle}\Big\vert_{\Delta T_2}$	Abs.Diff.
50%	0.001	*(pro)*	-1.03^{-8}%	-9.38^{-9}%	9.01^{-10}%
	0.01	*(pro)*	-3.13^{-7}%	-2.72^{-7}%	4.11^{-8}%
	0.001	*(contra)*	9.71^{-9}%	9.31^{-9}%	3.95^{-10}%
	0.01	*(contra)*	3.03^{-7}%	2.81^{-7}%	2.19^{-8}%
99%	0.001	*(pro)*	-1.93^{-6}%	-1.92^{-6}%	6.60^{-9}%
	0.01	*(pro)*	-2.11^{-5}%	-2.11^{-5}%	5.34^{-7}%
	0.001	*(contra)*	1.94^{-6}%	1.90^{-6}%	3.33^{-8}%
	0.01	*(contra)*	2.11^{-5}%	2.11^{-5}%	2.85^{-7}%

Considering Figure 3.8, where thermal dispersion for *pro* and *contra-flux* condition is represented, a central symmetry respect of the axes origin could be inferred: for the same values of Pe number and porosity, we have obtained similar values of thermal dispersion, with opposite sign (minus in *pro-flux*, plus in *contra-flux* regime). Moreover, it is possible to underline a substantial independence from the temperature gradient over the x axis, keeping constant the other two independent

variables, as shown in Table 3.5, where different results are compared, for extreme values of porosity and Pe number. As it has been done for tortuosity, points in Figure 3.8 are average values calculated for different thermal boundary conditions, with the same porosity and Pe values. However, if we look at the order of magnitude of the results obtained for this quantity, the thermal dispersion contribution on the energy balance is very small in the low Peclet number region (the maximum value obtained is approximately $\pm 2.1 \cdot 10^{-4}\%$ of the correspondent average thermal conductivity). Therefore, under these conditions, this quantity can be neglected.

Finally, if we consider both thermal tortuosity and dispersion, we could highlight a general agreement between numerical results of CFD simulations and correlation functions (3.5) and (3.6): R^2 coefficients are respectively 0.9699 and 0.9999. The greatest difference can be found for the lowest value of porosity considered ($\varepsilon = 50\%$): indeed, this seems to be the only situation in which there is no good correspondence between data and regression values. However, for low porosity range, thermal dispersion becomes increasingly negligible and tortuosity becomes less influential.

3.4 Conclusions and final remarks

All analyses shown in this work are finalized to obtain a detailed description of the fluid dynamic inside fibrous materials and the heat exchange between the flowing air and the solid matrix at microscopic scale. This could provide a better comprehension of the behavior of resistive dynamic insulation in building envelopes [3, 4].

Taking into account the relationship between velocity and pressure drop, a linear connection has been found, which corresponds to the Darcy equation. The ratio μ/K has been assumed as a non-linear function of the solid matrix porosity. Its form has been defined so that it becomes zero when we have a fluid domain, while it tends to infinity when the effective porosity, as it has been defined in §2.1, tends to zero.

Concerning with the thermal tortuosity, it is only dependent on the material porosity, while it is not affected by Pe number and temperature gradient. Moreover, this parameter seems to have a significant impact on the effective thermal conductivity, especially in the high porosity range ($\varepsilon \geq 90\%$). Conversely, thermal dispersion appears to be negligible: it depends both on the porosity and the Pe number, but its order of magnitude is lower than the $\pm 2.11 \cdot 10^{-4}\%$ of the volume average thermal conductivity. The effect of the working condition (*pro* or *contra-flux*) has been synthesized with the sign of both quantities: positive for *pro-flux* tortuosity and *contra-flux* dispersion, negative in other cases. For both thermal tortuosity and dispersion, regression equations have been obtained, with a good agreement to numerical results, except the ones coming from the lowest porosity considered ($\varepsilon = 50\%$).

As we stated previously in this Chapter, all analyses described have been done with the purpose to verify the reliability of the volume averaging technique for the problem under discussion. For this reason, no statistical approach to the geometry definition has been used. Anyway, in the future results will be used in numerical simulations after an experimental validation.

The following Chapter deals with the pervious concrete, also known as no-fines

concrete [30–32], characterization, which is based on a similar approach, while a more detailed geometrical definition of the solid matrix has been performed.

Chapter 4

No-fines concrete characterization

This Chapter deals with the characterization of no-fines concrete. This material is a cement based mixture, which is produced without using small diameter aggregates. This leads to a highly porous hardened solid matrix, with well interconnected pores. Thanks to its high permeability, this material has been largely used in streets pavement construction [30–32].

Taking into account its effective porosity and its thermal capacity, we have considered no-fines concrete a suitable choice for dynamic insulation technology, in order to develop a stratified technical solution optimized for Mediterranean climate conditions.

As it has been done for fibrous insulating materials, the volume average method has been applied. Unlike what has been presented in the previous Chapter, no geometrical approximation has been introduced: some cubic samples have been

subjected to image analysis. This procedure has led to the REV definition and the mesh production for CFD simulations.

Thermophysical properties of the solid matrix have been evaluated using a Transient Plane Source (TPS) apparatus [33–37].

Then, a simple experimental apparatus has been built to find the empirical correlation between average air velocity and pressure drop across no-fines concrete samples. The regression curve obtained has been compared with numerical simulations results, in order to validate them.

CFD simulations have also been used to calculate thermal tortuosity and dispersion as a function of porosity and Peclet number, as we described in the previous Chapter.

4.1 Domain definition and numerical model

In this section, the statistical approach used to define the REV dimension is described. Than, we present the procedure to define the solid matrix geometry, used to create calculus meshes for CFD simulations, and the laboratory anayses we have done in order to evaluate thermophysical properties of the solid phase of the porous medium considered.

4.1.1 The REV size

As stated in Chapter 2, a representative elementary volume can be considered as a physical point of the domain. This assumption implies that, for characteristic dimensions of the macroscopic problem (some orders of magnitude greater than the REV size), macroscopic (i.e. locally volume averaged) thermophysical and geomet-

rical properties are constant over the domain.

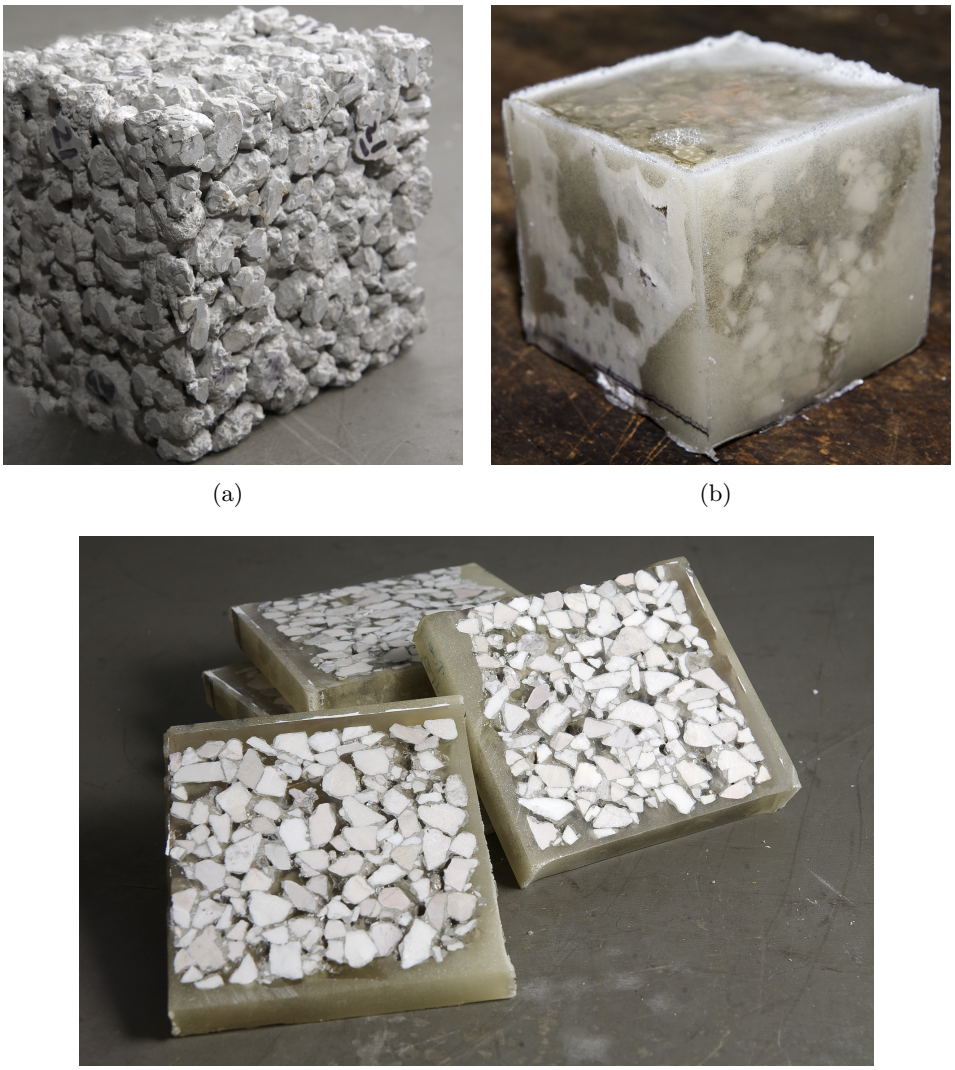

(a) (b)

(c)

Figure 4.1: (a) Picture of a cubic sample of no-fines concrete (this particular one has not been used for experimental purposes, because of some inaccuracies in the casting procedure). (b) Picture of one sample imbued in the hardened epoxy resin. (c) Picture of one impregnated sample cut into slices.

This means that, first of all, we have to find the typical REV size for no-fines concrete. Such a result has been obtained analyzing images of section of no-fines concrete small samples. These cubic samples, with a side dimension of 10 cm (Figure 4.1(a)), have been produced in collaboration with the research group of

Prof. Luca Bertolini, from Dipartimento di Chimica, Materiali e Ingegneria Chimica "'G.Natta"' of Politecnico di Milano. Mix-design parameters are as follows:

- water/cement mass ratio (w/c) - 0.39;
- aggregate/cement mass ratio - 7.03;
- aggregate - Zandobbio limestone
  - large gravel ($\phi = 9 \div 12mm$) - 60%;
  - medium gravel ($\phi = 6 \div 9mm$) - 40%;
- cement powder - limestone Portland cement CEM II-A-L/42.5

Once the samples were hardened, all inner cavities (pores) have been filled with a transparent epoxy resin and, after its solidification (Figure 4.1(b)), have been cut into slices (thickness of 1÷2 cm - Figure 4.1(c)), obtaining more or less 15 samples. After a photographic survey, 28 RGB images have been produced (e.g. Figure 4.2(a)) and transformed into binary (black and white) square $L_{img} \times L_{img}$ images (e.g. Figure 4.2(b)): white represents the fluid phase, while black represents the solid matrix.

Hence, samples obtained have been used to define the REV size, referring to following parameters: porosity and autocorrelation length (defined as the radial coordinate of the pixel related to the maximum value of autocorrelation function, as shown below).

With both porosity and autocorrelation length we have obtained two possible REV sizes (L_ε and L_{ACF}); the actual value used in further analyses (L_{REV}) is the greater of them.

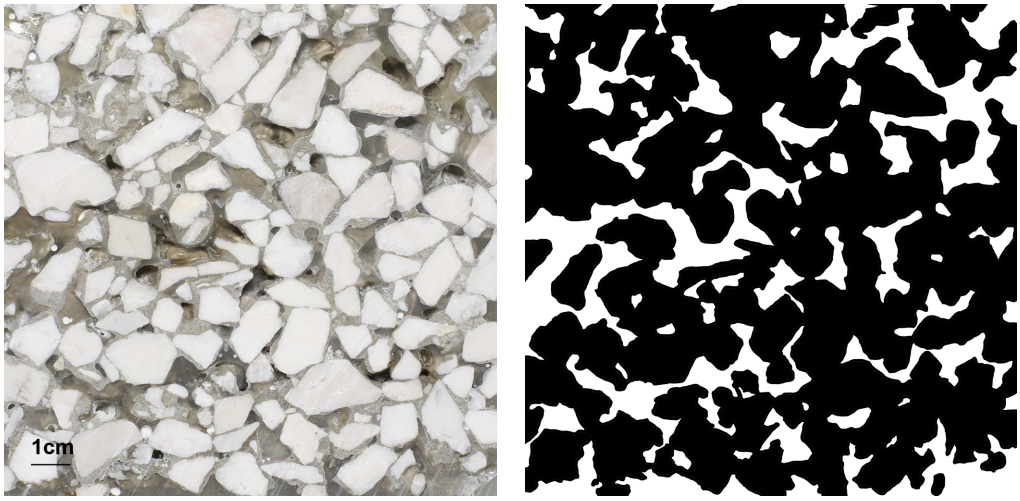

(a) (b)

Figure 4.2: (a) Original image of one of the slices obtained, with dimensional scale reported; (b) binary conversion of the image.

Porosity calculation

As described with Eq. (2.4), we can consider the binary representation of the no-fines concrete surface as a phase function as follows [38–40]:

$$Z(\mathbf{r}) = \begin{cases} 1 & \text{if } \mathbf{r} \text{ belongs to the pore space} \\ 0 & \text{otherwise} \end{cases} \tag{4.1}$$

where $\mathbf{r}$ represents the vector position of each point of the domain (or binary image), relative to a generic origin. Considering Eq. (4.1), in addiction to the physical definition of porosity related to Eq. (2.8), we can introduce its mathematical interpretation:

$$\varepsilon = \overline{Z}(\mathbf{r}) \cong \frac{\sum_{(i=1)}^{m} \sum_{(j=1)}^{n} Z(i,j)}{m \times n} \tag{4.2}$$

where the right member represents the discrete approximation, used for the binary

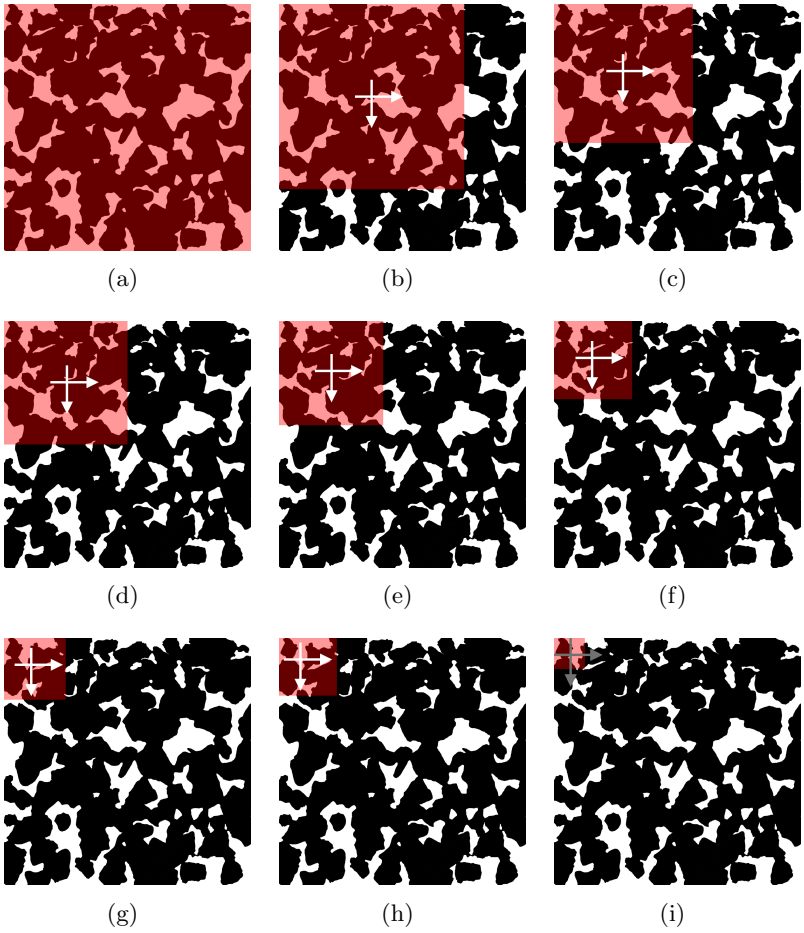

Figure 4.3: Graphical description of the procedure for porosity evaluation. The red box represents the jig used to collect subsamples of the image. The sampling procedure has been done translating horizontally and vertically, in order to scan the whole image. Sub-sample size are: (a) 1024×1024 pxl (1 sample); (b) 768×768 pxl (4225 samples); (c) 576×576 pxl (12769 samples); (d) 512×512 pxl (16641 samples); (e) 432×432 pxl (22201 samples); (f) 324×324 pxl (30976 samples); (g) 256×256 pxl (37249 samples); (h) 240×240 pxl (38809 samples); (i) 128×128 pxl (50625 samples).

images analysis. Going more in detail, we have taken samples from every binary image. For every image, a set of different *jigs* has been defined to collect subsamples from each image considered. The sampling process has been performed starting with the left-up corner of the image (with (0,0) coordinate), and identifying a subsample of predefined size each time the jig is moved one pixel, vertically or horizontally, over the whole image, like the procedure described in Figure 4.3. Then, samples

have been divided into groups, according to their side dimension. On each group we have calculated average porosity and standard deviation: the REV size assumed, referred to porosity, is the smallest side dimension (L_ε) with a porosity standard deviation lower than 4% (Figure 4.4).

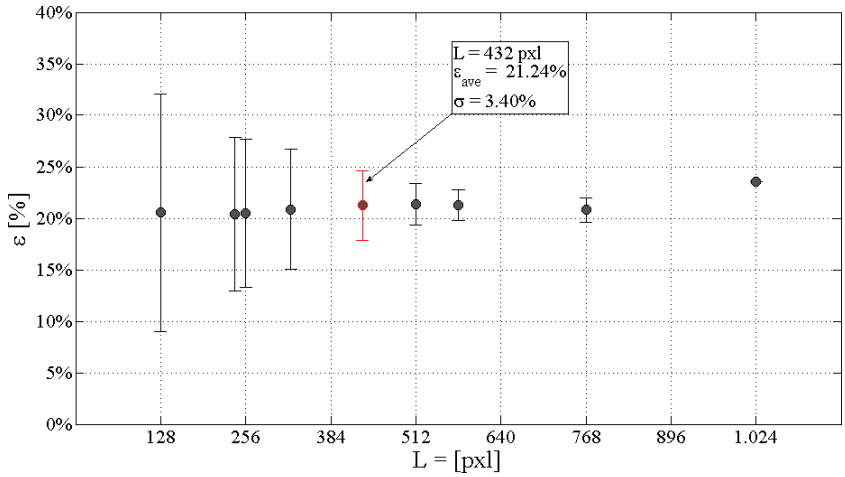

Figure 4.4: Statistical evaluation of REV size, referred to porosity (L_ε), of one of the samples considered. Dots represent average porosity (ε_{ave}) for a given sub-sample size (abscissa), while whiskers size is equal to standard deviation (σ).

Therefore, the procedure described has led two main results: first of all, possible values for REV dimension has been found; secondly, it has been possible to calculate the average porosity of each sample (image), as summarized in Figure 4.5.

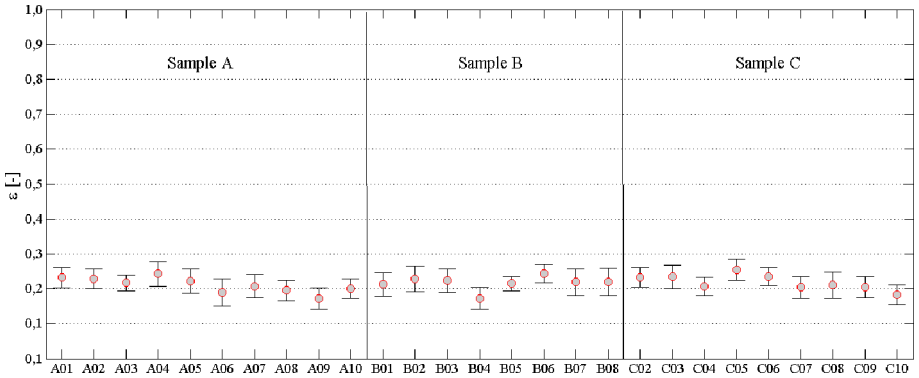

Figure 4.5: Mean values and standard deviations of porosity, calculated for each image taken from the samples A, B and C.

Autocorrelation function

The autocorrelation function, in its normalized form, is defined as follows [38,39]:

$$R_Z(\mathbf{u}) = \frac{\overline{[Z(\mathbf{r}) - \varepsilon]\,[Z(\mathbf{r}+\mathbf{u}) - \varepsilon]}}{\sigma^2} \tag{4.3}$$

where ε is the mean value of the phase function, calculated with Eq. (4.2) over the whole image, and σ^2 is the variance of the phase function and is equal to $\varepsilon - \varepsilon^2$ (because the function $Z(\mathbf{r})$ can be considered a Bernoulli distribution).

On each image, the autocorrelation function has been evaluated using an *ad hoc* developed code employed in MATLAB® environment. In literature [38, 39], this function is interpreted as characterizing the dependence of a generic point $(\mathbf{r} + \mathbf{u})$ upon a point $\mathbf{r}$ of the same image, parametric on its mean (ε). Therefore, the autocorrelation function can be considered a synthetic description of the solid matrix structure (pore size and interconnection, spatial periodicity, etc.), and its calculation has been performed in order to find in every image (mathematically considered a two-dimensional phase distribution) a possible sub-structure assumable as a REV.

As fare as the MATLAB® algorithm is concerned, in order to reduce the time consumption of calculations we have used the Fourier transform of each image: in fact, the convolution product, needed for the autocorrelation function evaluation in the Cartesian domain, becomes a simple product between the Fourier transform and its complex conjugate in the spatial frequency domain. The final passage has been the calculation of the inverse Fourier transform of the result, and gave us the autocorrelation of the original image (Figure 4.6).

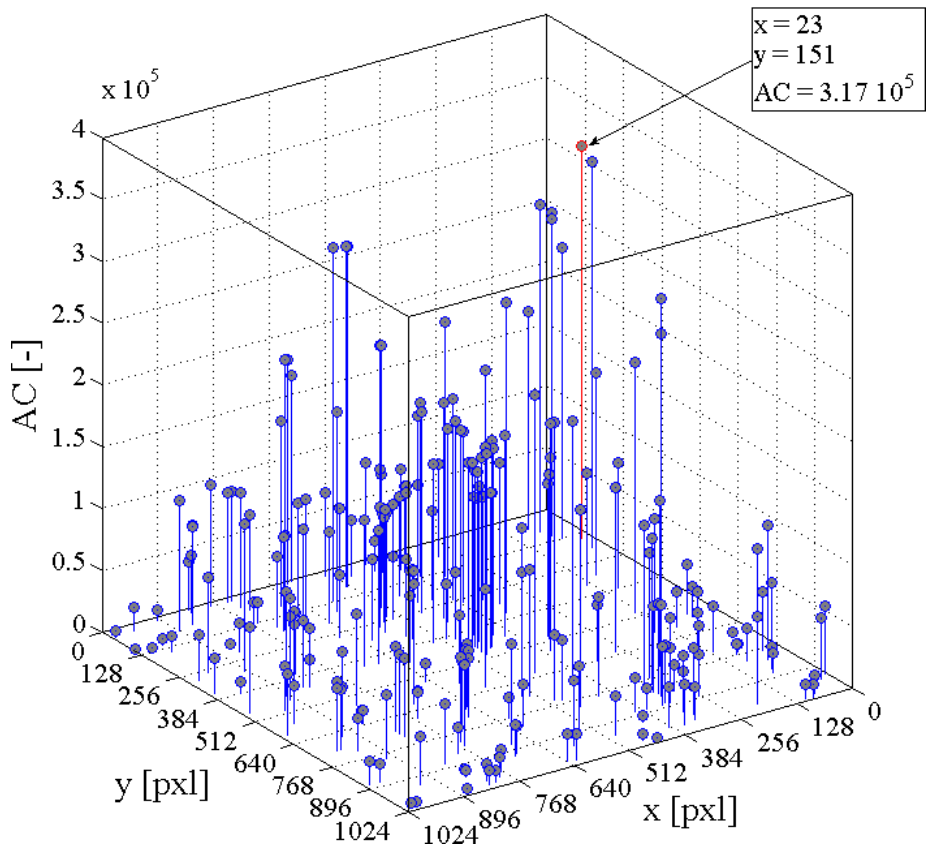

Figure 4.6: Autocorrelation function of one of the images considered. The highlighted value (red) is the absolute maximum of the function.

Finally, we have introduced the concept of autocorrelation length, which has been defined as the modulus of the coordinate vector **r**, related to the absolute maximum of the autocorrelation function of the image considered (In Figure 4.6 it is represented in red). This length has been defined as the REV size related to the solid matrix structure (L_{ACF}), defined as follows:

$$L_{ACF} = |\mathbf{r}_{max}| : R_Z(\mathbf{r_{max}}) = max \, \|R_Z(\mathbf{u})\| \, \forall \mathbf{u} \in L_{img} \times L_{img}. \tag{4.4}$$

Results of analyses

In Table 4.1 results of analyses previously described are summarized: L_ε, L_{ACF} and L_{REV} are reported both in terms of pixels and millimeters. Values reported in the last column of each table have been use for the domain definition in CFD simulation further described.

Table 4.1: List of REV size for each image taken from samples A, B and C.

Samp. A	L_{ACF}		L_ε		L_{REV}	
Image	[pxl]	[mm]	[pxl]	[mm]	[pxl]	[mm]
A_{01}	162	14.57	768	69.38	768	69.38
A_{02}	354	31.58	432	38.62	432	38.62
A_{03}	545	49.87	432	39.53	545	49.87
A_{04}	288	25.95	432	38.91	432	38.91
A_{05}	277	25.19	512	46.61	512	46.61
A_{06}	206	19.31	324	30.34	324	30.34
A_{07}	492	45.29	324	29.87	491	45.29
A_{08}	124	11.39	512	47.05	512	47.05
A_{09}	272	25.50	324	30.34	324	30.34
A_{10}	349	33.26	324	30.93	348	33.26
Samp. B	L_{ACF}		L_ε		L_{REV}	
Image	[pxl]	[mm]	[pxl]	[mm]	[pxl]	[mm]
B_{01}	153	14.33	432	40.54	432	40.54
B_{02}	369	35.90	432	42.10	432	42.10
B_{03}	373	36.52	512	50.10	512	50.10
B_{04}	263	24.82	324	30.60	324	30.60
B_{05}	428	40.79	432	41.21	432	41.21
B_{06}	614	56.15	432	39.51	614	56.15
B_{07}	352	33.17	512	48.33	512	48.33
B_{08}	282	27.49	432	42.08	432	42.08
Samp. C	L_{ACF}		L_ε		L_{REV}	
Image	[pxl]	[mm]	[pxl]	[mm]	[pxl]	[mm]
C_{02}	544	51.64	432	41.05	544	51.64
C_{03}	286	27.51	432	41.60	432	41.60
C_{04}	625	58.06	432	40.14	625	58.06
C_{05}	138	12.81	512	47.76	512	47.76
C_{06}	232	22.44	432	41.77	432	41.77
C_{07}	257	23.84	432	40.03	432	40.03
C_{08}	462	44.90	324	31.49	462	44.90
C_{09}	228	21.87	432	41.52	432	41.52
C_{10}	177	16.60	432	40.57	432	40.57

4.1.2 The mesh definition

Once the REV size of each image has been found, some of them has been used to produce numerical meshes for CFD simulations. A selection among them has been done in order to have an acceptable level of interconnection between pores, to allow the fluid motion across them. The admissibility of this arbitrary choice will be later discussed in §4.3.1.

Image vectorization

The first step was to transform pixel images into vectorial ones, to be able to import them into a mesh modeler.

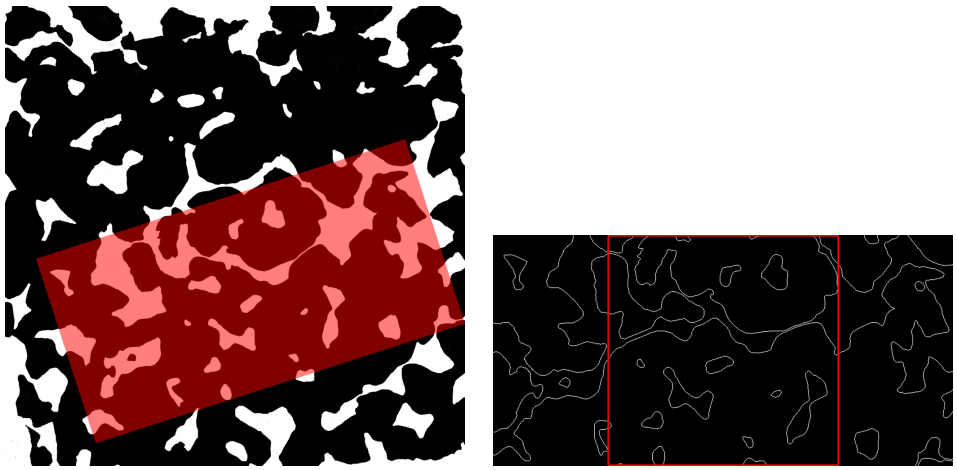

(a) (b)

Figure 4.7: (a) rectangular selection in a binary image of a porous section; (b) result of the edge detection process. The red square represents the central REV, used for further calculation of parameters.

In the chosen images, a rectangular selection has been taken (Figure 4.7(a)), which dimension are L_{REV} hight and $2 \times L_{REV}$ width. The reason of this approach will be explained in §4.2.

The procedure used to obtain each mesh used for numerical simulations is di-

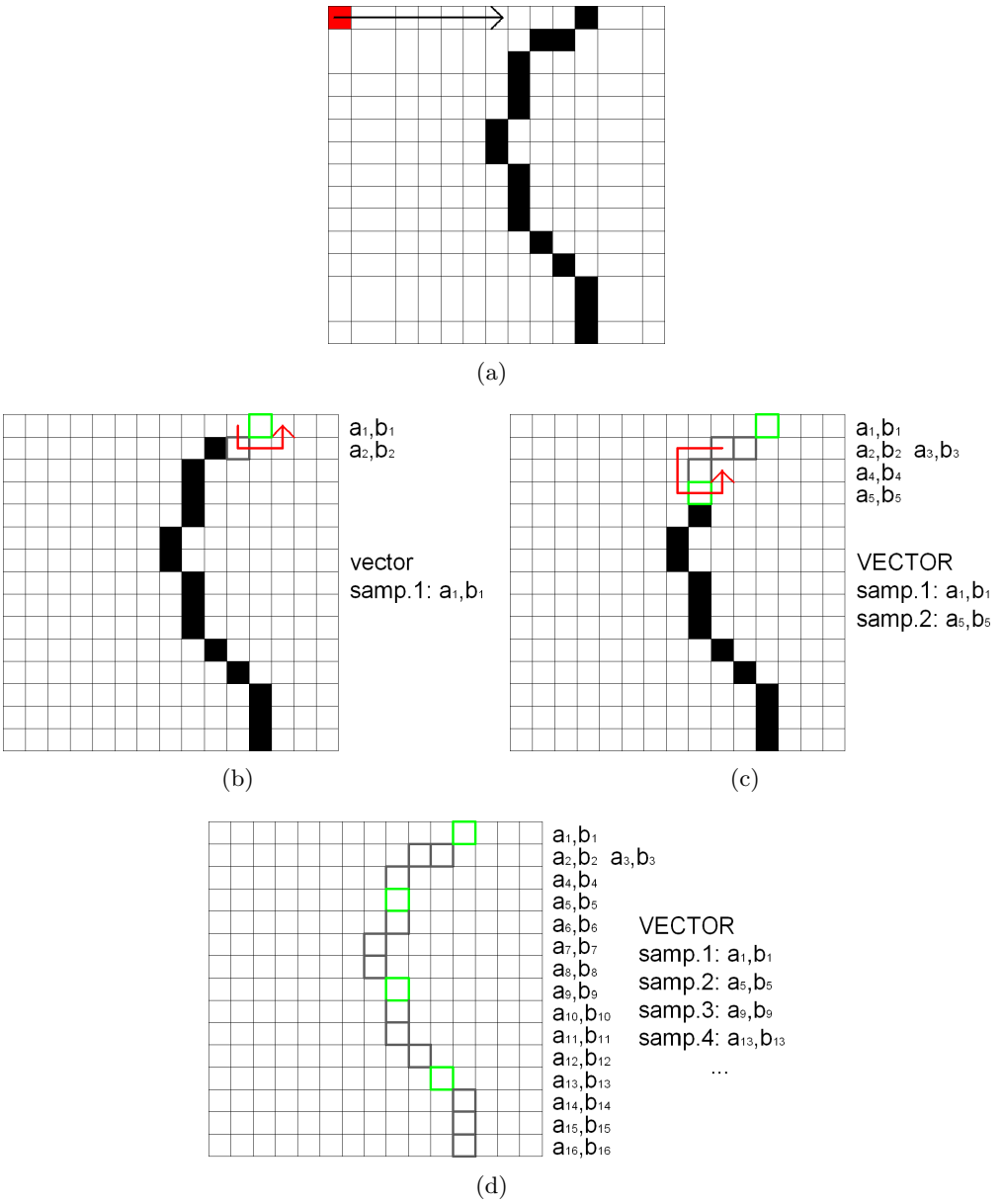

Figure 4.8: Notice that these images have illustrative purposes only: black and white are reversed compared to the images actually used in the analyses. (a) The scanning procedure starts from the pixel (1,1); (b) the first not-null pixel is turned into null, while its coordinates are registered in a vector. This pixel is used as a reference to scan the surrounding pixels; (c) any other not-null pixel found is turned to null and used as a new reference. (d) Coordinates are recorded into the vector every four pixels sampled.

vided in two main steps: first of all, every rectangle is processed with a edge-detection algorithm developed in MATLAB®, in order to produce binary images with the only representation of boundary between solid and fluid phases (Fig-

ure 4.7(b)); secondly, these new images have been vectorized with another algorithm developed with a MATLAB® code. Final results have been used as starting point to define calculus mesh for CFD simulations.

Going more in detail, the algorithm analyzes binary images similar to the example reported in Figure 4.7(b). Considering every image as a two-dimensional array of boolean values, where edges are 1 and other point are 0, the program starts the scanning process from the first element (first row, first column - Figure 4.8(a)) and moves following a horizontal path until it finds a not-null pixel (Figure 4.8(b)). Its value is turned to 0 and its coordinates (i, j) are registered in a vector. At this point, the program scans the perimeter of the $(i \pm 1, j \pm 1)$ square, moving with a counterclockwise direction (Figure 4.8(c)). When a new not-null pixel (i', j') is found, it is used as the center of a new $(i' \pm 1, j' \pm 1)$ square. Again, its value is turned to zero. Coordinates are recorded into the vector every four pixels found (Figure 4.8(d)).

Meshing procedure

The final coordinate vector, produced by the vectorizing algorithm described above, is transformed using an appropriate *pixel*→*mm* conversion and, later, is used to generate a journal file to be run in Gambit© [41]. In this way, we are able to automatically generate a raw version of the edges of the domain. Finally, they have been refined, and a triangular pave mesh has been defined, with a grid spacing two orders of magnitude smaller than the REV size. The resulting geometrical model has been loaded in Fluent©, and used as a calculus domain [41].

4.1.3 Thermophysical properties measurement

After the mesh definition, an experimental study of the solid matrix of no-fines concrete was needed to obtain its thermophysical properties, required to perform CFD simulations.

Measurements have been done using a Transient Plane Source apparatus [33–37], represented in Figure 4.9. All studies have also been done on samples which have been expressly produced, so that they were representative of the solid matrix of no-fines concrete.

The TPS apparatus

This laboratory device is composed by a multimeter, a power supply, a Wheatstone bridge and a probe (also known as *hot-disk*), and is based on the theory of heat conduction in a semi-infinite solid medium.

Going more in details, the hot-disk plays both the functions of heat source and sensing element. Indeed, every record is based on two main phases: during the first one, the probe is sandwiched between two samples of the same material (the contact surface has to be smooth enough, in order to reduce the contact resistance between materials); a very low potential difference is provided by the power supply, to allow the user to balance the bridge. This means that the probe and the samples are in thermal equilibrium, and a 0 V potential is measured.

Than the proper measurement phase starts: the hot-disk, represented in Figure 4.10, provides thermal power to the sample, thanks to a double nickel spiral, and measures the temperature increase at the same time, for a user-defined transient period. Temperature measurement is obtained by means of potential difference

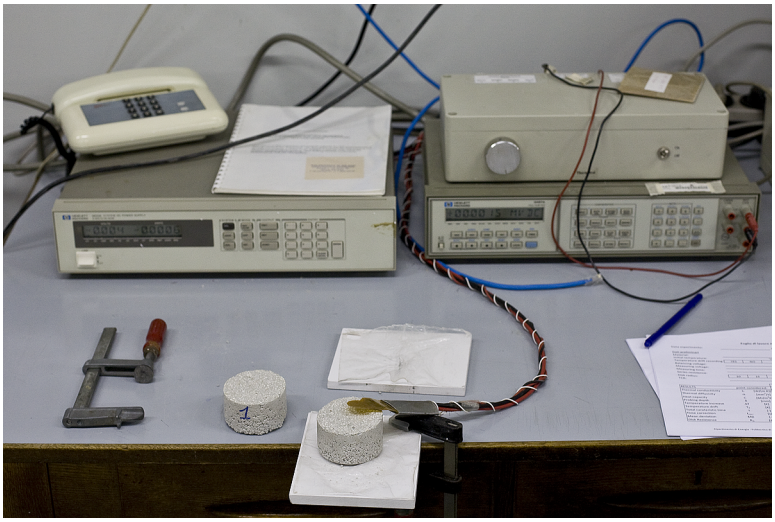

Figure 4.9: Picture of the TPS apparatus: on the right side there are the multimeter (bottom) and the Wheatstone bridge; on the left side there is the power supply. On the bottom of the picture there are the circular probe and one of the concrete samples used in the experimental analysis.

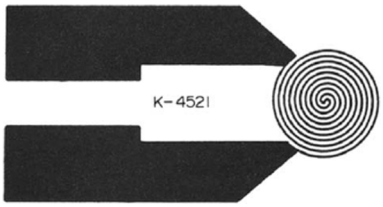

Figure 4.10: Representation of the hot-disk probe used in the TPS apparatus (figure found in [33]).

measurement. In fact, the temperature rise of the sensor causes a increase in its electrical resistance $R(t)$, according to the following equation:

$$R(t) = R_0 \left[1 + \alpha_{TCR} \cdot \overline{\Delta T}(\tau)\right] \tag{4.5}$$

where R_0 is the TPS electrical resistance before the transient recording has been initiated (it is measured during the balancing phase), α_{TCR} is the temperature coefficient of resistivity, and $\overline{\Delta T}(\tau)$ is a mean value of the time dependent temperature increase experienced by the hot-disk. Than, the electrical resistance increase causes the Wheatstone bridge imbalance, generating a potential difference $\Delta V(t)$, which

is measured by the multimeter.

At the end of the transient recording, time dependent temperature increases are calculated reverting Eq. (4.5). Their values are also analytically calculated, taking into account the output of thermal power provided by the hot-disk, the sensor geometry and hypothesis values for thermal conductivity and diffusivity [33]. Such values are than refined iteratively, by means of comparisons between time dependent temperature increase values measured and that analytically calculated.

Therefore, the temperature variation over time is used to solve the inverse problem of heat conduction, in order to iteratively calculate thermal conductivity, thermal diffusivity and heat capacity at the same time [34]. For more details about the hot-disk method, pleas refer to [42].

Samples

In order to measure thermophysical properties of the whole no-fines concrete solid matrix, some cylindrical samples have been expressly prepared: in fact, we had to perform TPS measurements on samples with a very low porosity (few small pores, poorly interconnected) and, at the same time, the mixture had to be representative of the overall solid matrix of cubic samples described in §4.1.1.

Therefore, we have used the same mix-design of cubic sample, keeping the same water/cement and aggregate/cement mass ratio, but changing the aggregate size, replacing gravel with sand and powder of Zandobbio limestone in the following percentage:

- sand ($\phi = 1 \div 2mm$) - 60%;

- powder ($\phi < 1mm$) - 40%;

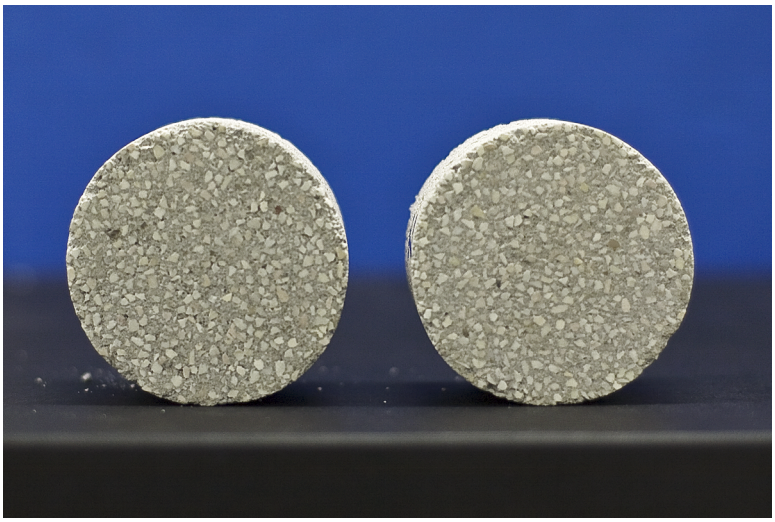

Figure 4.11: Two of the samples used to measure thermophysical properties of the no-fines concrete solid matrix.

Samples radius (30 mm) have been defined so that they were suitable for the hot-disk radius (10 mm). Every sample has been cast and cut into two pieces, after its hardening (Figure 4.11). Than, cut surfaces have been sanded, in order to reduce, as far as possible, the contact thermal resistance between samples and the probe.

Results

In Table 4.2 results of TPS measurements are reported. It is important to notice that such experimental arrangement provides values for thermal conductivity, thermal diffusivity and heat capacity, which are homogeneous equivalents of the compound structure of samples (intra-pore radiative heat transfer is thus taken into consideration using such properties). The density ρ has than been evaluated by means of volume and weight measurements.

Table 4.2: Thermal conductivity, thermal diffusivity, heat capacity and density obtained by means of experimental measurements.

quantity	Mean	Std. Dev.
density - ρ [kg/m^3]	1823.65	107.35
th. conductivity - λ [W/mK]	2.101	0.396
th. diffusivity - α [m^2/s]	$1.588{\cdot}10^{-06}$	$0.656{\cdot}10^{-06}$
heat capacity - C [MJ/m^{3}K]	1.445	0.377

Finally, in Table 4.3 thermophysical properties used in CFD simulations are reported, both for air (fluid phase) and solid matrix. Starting from experimental results, specific heat of the solid matrix c_s has been calculated using the definition of thermal diffusivity α:

$$\alpha = \frac{\lambda}{c_s \cdot \rho} \Rightarrow c_s = \frac{\lambda}{\alpha \cdot \rho} \tag{4.6}$$

Table 4.3: Thermophysical properties of fluid and solid matrix used in CFD simulations.

Fluid: Air	
Density - ρ_f	1.225 kg/m^3
Conduttivity - λ_f	0.024 W/mK
Specific Heat - $c_{p,f}$	1006 J/kgK
Solid: Zandobbio limestone, cement powder and water	
Density - ρ_s	1824 kg/m^3
Conduttivity - λ_s	2.101 W/mK
Specific Heat - c_s	815 J/kgK

4.2 Boundary conditions

For what concerns boundary conditions adopted for CFD simulations, we have adopted the same approach described in §3.2, in the fibrous insulation characterization. For every mesh considered, five steps of average inlet velocity have been applied to the inlet section (left side) of the domain. Pe number has been succes-

sively calculated using the mean volume value of the x component of velocity. A horizontal temperature gradient $\Delta T_x/L$ has been imposed, keeping its value constant along the y-axis: as described in the previous Chapter, temperature values have been given for the left side, both for the solid wall and the inlet fluid.

As far as the right side is concerned, we have experienced the same problem we had in the fibrous insulation treatment: since the fluid part of the unit-cell right side is an outlet boundary condition, it was not possible to assign any temperature value. The solution to this problem has been achieved extending two times the elementary cell over the x direction and imposing the temperature value on the solid part of the right side. The calculus domain has than been divided into three parts: the first and the third are $L_{REV}/2$ width, while the central one has the same width of one REV, and has been used in data processing.

Velocity and temperature boundary conditions used in CFD simulations are summarized in Table 4.4 and 4.5 respectively. The simulation of *pro-flux* and *contra-flux* conditions have been performed reverting temperature values of left and right faces.

Table 4.4: Boundary conditions for the numerical solution of the velocity field.

Inlet mean velocity	u_a	u_b	u_c	u_d	u_e
$\bar{u}_{in}$ $[m/s]$	0.001	0.003	0.005	0.007	0.01

4.3 Results and discussion

As mentioned above in §4.1.2, only 12 of the 29 no-fines sections have been vectorized and used as calculus domain in CFD simulations. Results have been

Table 4.5: Boundary conditions for the numerical solution of the temperature distribution. Data in bold are related to the mesh effectively used for CFD simulations

mesh	ΔT_1	ΔT_1	mesh	ΔT_1	ΔT_1	mesh	ΔT_1	ΔT_1
A_{01}	3.469 K	17.346 K	**B_{01}**	**2.022 K**	**10.112 K**			
A_{02}	**1.931 K**	**9.654 K**	**B_{02}**	**2.105 K**	**10.524 K**	C_{02}	2.582 K	12.909 K
A_{03}	2.494 K	12.468 K	B_{03}	2.505 K	12.524 K	**C_{03}**	**2.080 K**	**10.401 K**
A_{04}	**1.946 K**	**9.729 K**	B_{04}	1.530 K	7.650 K	C_{04}	2.903 K	14.516 K
A_{05}	2.331 K	11.653 K	**B_{05}**	**2.061 K**	**10.303 K**	C_{05}	2.388 K	11.940 K
A_{06}	**1.517 K**	**7.584 K**	B_{06}	2.807 K	14.037 K	**C_{06}**	**2.088 K**	**10.442 K**
A_{07}	2.265 K	11.324 K	B_{07}	2.416 K	12.081 K	**C_{07}**	**2.001 K**	**10.007 K**
A_{08}	2.353 K	11.763 K	**B_{08}**	**2.104 K**	**10.520 K**	C_{08}	2.245 K	11.225 K
A_{09}	1.517 K	7.586 K				C_{09}	2.076 K	10.381 K
A_{10}	**1.663 K**	**8.315 K**				**C_{10}**	**2.029 K**	**10.143 K**

used to evaluate fluid dynamic parameters (permeability and Ergun coefficient) and heat transfer parameters (thermal tortuosity and thermal dispersion), in order to define regression functions with macroscopic parameters, such as porosity and Peclet number. Permeability and Ergun coefficient values have also been validated by means of laboratory tests.

4.3.1 Fluid dynamic

For what concerns the evaluation of fluid dynamic parameters in Eq. (2.29), we have adopted two approaches: first of all, we have performed some laboratory tests aimed at detecting the connection between pressure drop and average air velocity inside pores for no-fines concrete, which have led to a regression equation. Secondly, we have compared this equation with numerical results coming from CFD simulations of no-fines concrete REVs, to validate this latter.

In order to analyze the fluid dynamic behavior of no-fines concrete, we have built an experimental arrangement (Figure 4.12), mainly consisting in a parallelepiped-shaped wood box, which is used to accommodate samples, with in-line inlet and

outlet sections. Circular section ducts have been connected both to the inlet and the outlet of the box.

The inlet channel has been used to simplify the air velocity measurement: it is know that, for a laminar regime, the air velocity has a parabolic profile, with the maximum in the channel axis and a null value in the area of contact between the fluid and the inner walls of the pipe. Therefore, after confirming that the regime was laminar for all flow rates imposed, we have limited our measurements to the central (maximum) value of the velocity profile of the inlet section. From this information we have been able to calculate the volumetric flow rate (m^3/s) and, knowing the area of the samples front section, evaluate the Darcean velocity, as it has been defined in §2.3. For what concerns the outlet channel, its purpose was only to allow the connection to the extraction fan.

Finally, pressure drop across samples have been measured with a differential manometer. If we consider Figure 4.12(b) it is possible to notice that there is an empty chamber upstream samples inside the box, while another one is located downstream. They have been used to stabilize pressure values before and after samples, in order to obtain more reliable measurements of the pressure drop.

Dealing with no-fines concrete samples, they have been prepared using the same mixture described in §4.1.1. Moreover, their size (0.32 m $\times$ 0.32 m $\times$ 0.15 m) is bigger than that of cubic samples: in fact, they have been prepared with the original purpose to build a 1 m $\times$ 1 m wall to be used in thermal analyses performed with the *DAVTB* apparatus described later in this dissertation. More details about this experimental arrangement are provided in Chapter 6.

Pressure drop measurements have been performed on four of the nine samples

(a) (b)

Figure 4.12: (a) overview of the experimental arrangement for pressure drop measurement. (b) Detail of the sample and the air flow inlet section.

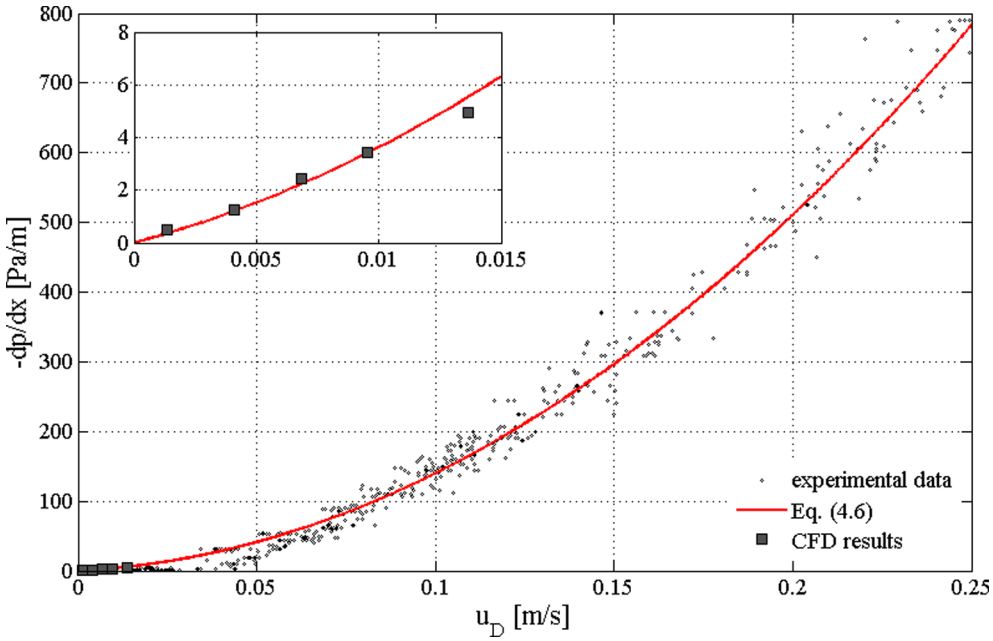

Figure 4.13: Experimental data and regression curve for pressure drop vs filter velocity in no-fines concrete samples. In the small box, a comparison with the regression curve and numerical values obtained with CFD simulations is reported, values for abscissa are reduced to values typical for dynamic insulation technology.

prepared, combined in various way, in order to obtain a wide data set to process. Values of filter velocity and differential pressure have been than used to obtain the

following regression equation ($R^2 = 0.9839$), reported in Figure 4.13:

$$-\frac{dp}{dx} = 11530u_D^2 + 247.3u_D \tag{4.7}$$

while for fibrous insulation, according to Darcy equation, a linear relationship between $\frac{dp}{dx}$ and u_D has been found, for no-fines concrete we have obtained a quadratic relationship, like the more general reported, in a time-dependent form, with Eq. (2.29). For this reason, we have used both velocity coefficients in Eq. (4.7), in order to empirically derive permeability and Ergun coefficient for no-fines concrete: assuming air density ρ and dynamic viscosity μ equal to 1.205 kg/m^2 and $1.81{\cdot}10^{-5}$ Pa·s respectively, we have obtained

$$K \cong 7.32 \cdot 10^{-8}\ m^2$$

and

$$C_E \cong 2.589.$$

As we have stated previously, we have validated numerical results of CFD simulations, from the fluid dynamic point of view, by means of direct comparison with values calculated using Eq. (4.7), as reported in the small box in Figure 4.13.

It is important to notice that results coming from CFD simulations on no-fines concrete REV have a punctual meaning: in fact, according to the theoretical approach summarized in Chapter 2, a representative elementary volume can be considered as a physical point of the mediated domain. This assumption is not true any more when we deal with experimental results obtained with the procedure

previously described, which allow us to obtain only mean quantities. For this reason, in order to compare Eq. (4.7) with numerical results, we have mediated these last, grouping the ones with the same boundary condition for the inlet velocity. This manipulation led us to the points reported in the small box in Figure 4.13, which show a good agreement between experimental and numerical results.

Moreover, this evidence means also that calculus domains used for CFD simulations are enough representative for the real porous medium, even if we have arbitrarily chosen them, as stated in §4.1.2.

4.3.2 Heat transfer

According to what we have done in the fibrous insulation characterization described in Chapter 3, results coming from CFD simulations of no-fines concrete meshes have been used to derive regression equations for thermal tortuosity $\lambda_{tor,xx}$ and thermal dispersion $\lambda_{disp,xx}$, trying to relate them with both porosity ε and Peclet number Pe_H.

We have to notice that results obtained from this kind of irregular geometries are more disperse than the ones coming from fibrous insulation. Moreover, we also have to consider that the range of porosity values we have been able to reproduce is smaller than the $50\% \div 99\%$ one: for no-fines concrete we have

$$\varepsilon = 18.5\% \div 23.5\%.$$

Regression equations have been evaluated trying to use the same shape of Eqs. (3.5) and (3.6), and changing only coefficients.

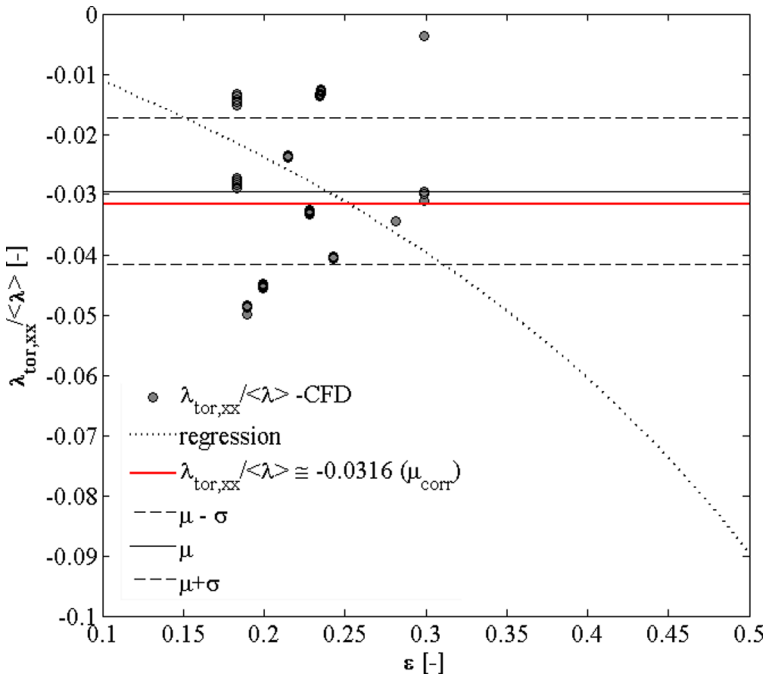

Figure 4.14: Thermal tortuosity for no-fines concrete in *contra-flux* condition. Comparison between numerical results and regression analysis.

Taking into account thermal tortuosity, it seems to be affected only by the material porosity, while it shows little sensitiveness to different values of horizontal thermal gradient and Pe number, like what we have noticed for fibrous insulation. In a first step we have searched for coefficients to modify Eq. (3.5), to make it representative for numerical data. Unfortunately, being thees too disperse, it has not been possible to achieve any acceptable result: the best regression curve obtained, represented in Figure 4.14, has a R^2 parameter lower than 0.4.

Therefore, we had to follow a different approach: considering that tortuosity values are generally in a range between the 1% and the 5% of the volume average thermal conductivity (calculated according to Eq. (3.4)), they have small effect over the whole thermal behavior of the domain, but they can not be considered negligible. Than, we have decided to calculate a constan mean value, not depending

on ε, working in two steps: fist of all, mean value and standard deviation of the whole data set have been calculated; secondly, values not included in the range $\mu - \sigma \div \mu + \sigma$ have been considered outliers and eliminated. A new mean value has been calculated on the remaining data, and assumed to be equal to $\lambda_{tor,xx}/\langle\lambda\rangle$. According to this approach, we have obtained:

$$\lambda_{tor,xx}/\langle\lambda\rangle \cong \mp 3.16\%,$$

where we consider a negative value for *pro-flux* and a positive one for *contra-flux*: again, when air flow and thermal flux have the same direction, thermal tortuosity gives a positive contribution on effective thermal conductivity; while it decreases $\lambda_{eff,xx}$ in *contra-flux* condition.

In Figure 4.14 are reported the first and the second (actual thermal tortuosity) mean values, the selection range, the trial regression equation and the complete set of numerical data.

Dealing now with thermal dispersion, the central symmetry underlined for fibrous insulation and the independence from the temperature gradient have been confirmed. Therefore, numerical results have been used to search for new coefficient suitable to modify the fibrous insulation regression Eq. (3.6), in order to obtain a new relation with porosity and Peclet number. Again, data are more disperse than the ones reported in §3, because of the irregular shape of the different solid matrices assumed as calculus domains.

After a firs trial, we have also noticed a not negligible difference (more than one order of magnitude) between results coming from two of the considered meshes

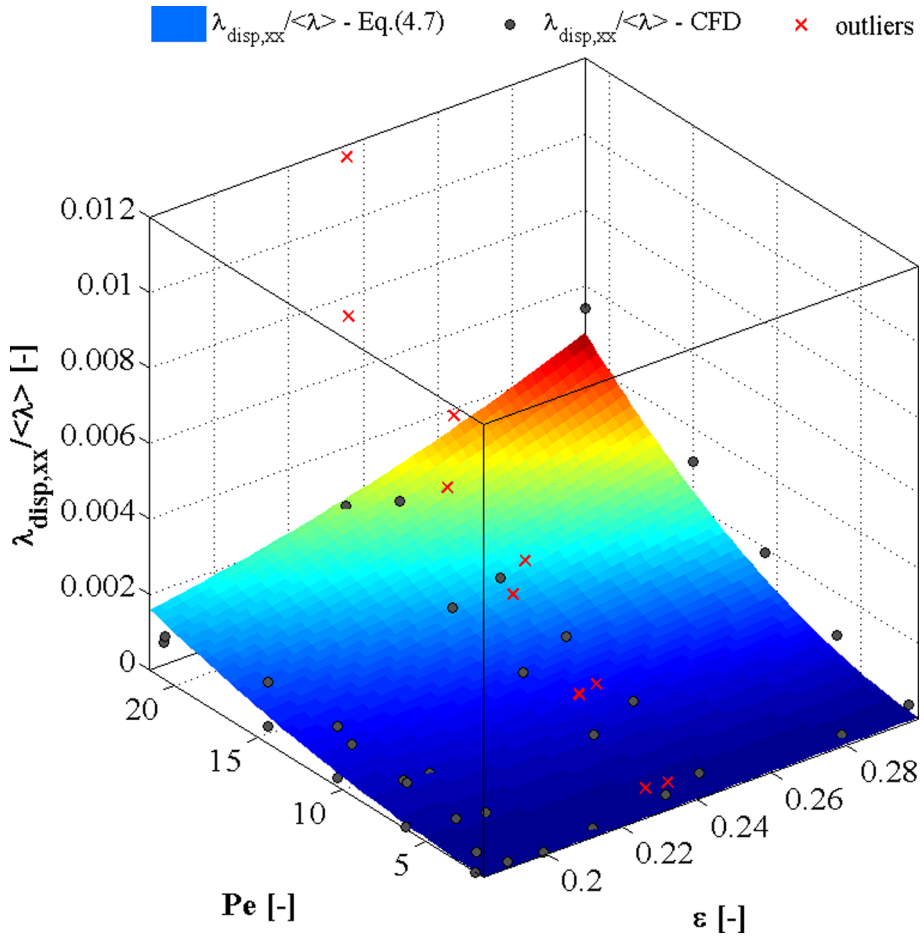

Figure 4.15: Thermal dispersion for no-fines concrete in *contra-flux* condition. Comparison between numerical results and regression analysis.

and the regression surface initially obtained. A detailed analysis of simulations performed have highlighted a wrong choice of the vectorized image portion: in fact, image subsamples considered for such simulations are smaller than the actual REV size. Therefore, their results have been rejected.

The new data set has than been used to derive a new regression equation, portrayed in Figure 4.15, which seems to be enough representative of numerical results ($R^2 \cong 0.9871$):

$$\frac{\lambda_{disp,xx}}{\langle\lambda\rangle} \approx \pm 6.343 \cdot 10^{-7} \cdot Pe_H^2 \cdot e^{100\varepsilon^2\left[\frac{(1-\varepsilon)^2}{2}\right]} \tag{4.8}$$

However, if we take into account the order of magnitude of the numerical results obtained for this quantity, its effect on the energy balance is very small in the low Peclet number region considered (the maximum value obtained is approximately $\pm 0.8\%$ of the correspondent average thermal conductivity). Therefore, under these conditions, this quantity can be neglected, like we have assumed for fibrous insulation.

4.4 Conclusions and final remarks

Following the same approach described in Chapter 3, all analyses performed are meant to obtain a detailed description of the fluid dynamic inside no-fines concrete and the heat exchange between the flowing air and the solid matrix at microscopic scale, and their effects from the macroscopic point of view.

First of all, a detailed analysis of solid matrix geometries has been performed, aimed at evaluate values for porosity and REV size. Moreover, images used for such studies have been exploited to define calculus domains for CFD simulations, thanks to a MATLAB® vectorization algorithm we have developed.

Dealing with the relationship between filter velocity, as it is described in §2.3, and pressure drop, a quadratic equation has been found: air permeability and Ergun coefficient have been found by means of laboratory tests, performed using an experimental arrangement expressly built. The regression curve has than been compared with appropriately manipulated numerical results of CFD simulations, in order to validate the mesh definition procedure.

Concerning with thermal tortuosity, we have not been able to relate it with the

solid matrix porosity, because of its high degree of dispersion (in a range between the 1% and the 5% of the volume average thermal conductivity). Moreover, no significant connection with Pe number and temperature gradient has been found. For this reason, we have decided to evaluate a corrected mean value, which is around the 3.16% of the volume average thermal conductivity.

Taking into account thermal dispersion, a dependence on porosity and Pe number has been found, while there is no effect coming from the temperature gradient. A regression curve has been derived, with the same shape of the one defined for fibrous insulation. Anyway, this quantity seams to be negligible, because its order of magnitude is generally lower than the 0.8% of the volume average thermal conductivity.

Even if a part of numerical results has been experimentally validated, the found thermal tortuosity and dispersion relations with porosity and Pe still need to be confirmed. Therefore, an experimental set up, which is described in Chapter 6, has been designed and built. Unfortunately, the lack of time did not allow us to perform such laboratory test.

In the next Chapter, the description of a finite one-dimensional difference simulation algorithm is reported, which purpose is to simulate the thermal performance of dynamic insulation envelope technologies.

Chapter 5

Numerical simulation of Dynamic Insulation walls

The evaluation of energy performance of a building envelope technical solution is, in general terms, closely related to the whole building structure and to boundary conditions, such as climate forcing agents, internal gains, etc. Moreover, when summer performances are investigated, a time-dependent approach is most appropriate than a steady-state model.

For this reason, we have developed a numerical simulation algorithm, expressly deigned to assess the thermal performance of a multilayer dynamic insulation wall, taking into account the environment in which it operates. The numerical modeling approach adopted is based on the one-dimensional finite difference method, for the energy equation. On the other hand, a quasi-static treatment has been used for the flow field calculation.

After a development phase, which has been done working on a MATLAB® code,

we have built a component to be integrated into the TRNSYS© simulation environment, in order to explore the dynamic insulation building component performance when it is coupled with a complex building structure, with statistically meaningful boundary conditions.

5.1 A finite difference model of permeable materials

When a differential problem can not be solved analytically, the only possible approach is the numerical solution of its discrete approximation, namely the implementation of a *numerical method* [43]. Generally speaking, if we consider the abstract exact problem

$$F(x, d) = 0,$$

where d is the data set which the solution depends on, x is the solution, and F expresses the functional relationship between x and d, and the numerical approximation of the problem

$$F_n(x_n, d_n) = 0,$$

following properties have to be respected:

consistency: if x is the solution of the exact problem corresponding to the data set d, we must obtain

$$F_n(x, d) = F_n(x, d) - F(x, d) \to 0 \text{ if } n \to \infty;$$

convergence: if the numerical solution tends to the exact solution for a growing

number of nodes n

$$\lim_{n\to\infty} \max \|F_n(x_n, d_n) - F(x_n, d_n)\| = 0;$$

stability: if the solution x_n depends continuously on the data d_n. More precisely, if δd_n is an admissible perturbation of data, and δx_n is the corresponding solution, we must have

$$F_n(x_n + \delta x_n, d_n + \delta d_n) = 0.$$

One of possible approaches to numerically solve a generic differential problem $F(x, d) = 0$ is represented by the finite difference method: it is based on the original definition of a function derivative, which is equal to the limit of the incremental ratio. In general terms, we have:

$$\dot{f}(x) = \frac{df}{dx} = \lim_{\Delta x\to 0} \frac{f(x + \Delta x) - f(x)}{\Delta x} \tag{5.1}$$

Moving from a continuous space to a discrete one, the limit operation can be eliminated, and a function derivative can be replaced with its incremental ratio. In this way, starting from a continuous problem, mathematically modeled with a partial differential equation, we have to deal with a discrete one, treated as a linear equation system: in fact, the one-dimensional spatial domain is discretized with a calculus grid and nodes are used to evaluate the approximated solution.

Therefore, the discretization procedure leads to the definition of a coefficient matrix, which links the solution of the approximated in between two adjacent time

steps for every node of the spatial domain. More in detail, we can have

$$\{T_n\}^{\tau+1} = \underline{\underline{A}}_{exp} \{T_n\}^{\tau} = [a_{n,n}]_{exp} \{T_n\}^{\tau}$$

for a full-explicit time modeling, and

$$\{T_n\}^{\tau} = \underline{\underline{A}}_{imp} \{T_n\}^{\tau+1} = [a_{n,n}]_{imp} \{T_n\}^{\tau+1}$$

for a full-implicit one.

For what concerns the temperature distribution $T(x,t)$, derivative terms in the Eq. (2.42) are than approximated using the Taylor series expansion, in the right and left neighborhood of x and t alternatively:

$$T(x+\Delta x,t) = T(x,t) + \frac{\partial T(x,t)}{\partial x}\Delta x + \frac{\partial^2 T(x,t)}{\partial x^2}\frac{\Delta x^2}{2} + R_2(x) = T_{j+1}^{\tau} \qquad (5.2)$$

$$T(x-\Delta x,t) = T(x,t) - \frac{\partial T(x,t)}{\partial x}\Delta x + \frac{\partial^2 T(x,t)}{\partial x^2}\frac{\Delta x^2}{2} + R_2(x) = T_{j-1}^{\tau} \qquad (5.3)$$

$$T(x,t+\Delta t) = T(x,t) + \frac{\partial T(x,t)}{\partial t}\Delta t + \frac{\partial^2 T(x,t)}{\partial t^2}\frac{\Delta t^2}{2} + R_2(t) = T_{j}^{\tau+1} \qquad (5.4)$$

$$T\left(x,t+\Delta t\right)=T\left(x,t\right)-\frac{\partial T\left(x,t\right)}{\partial t}\Delta t+\frac{\partial^{2}T\left(x,t\right)}{\partial t^{2}}\frac{\Delta t^{2}}{2}+R_{2}(t)=T_{j}^{\tau-1} \tag{5.5}$$

where $R_2(x)$ and $R_2(t)$ are the remains of the Taylor series expansions referred to space and time respectively, and are due to the second order truncation. Time and space derivatives are than treated separately: for both first and second order space derivatives, a centered finite difference approach is used; conversely, a backward (full-implicit) Euler method is used for the time derivative. Therefore we have:

$$\text{First order space derivative (centered difference):}\ \frac{\partial T}{\partial x}\cong\frac{T_{j+1}^{\tau}-T_{j-1}^{\tau}}{2\Delta x} \tag{5.6}$$

$$\text{Second order space derivative (centered difference):}\ \frac{\partial^{2}T}{\partial x^{2}}\cong\frac{T_{j+1}^{\tau}-2T_{j}^{\tau}+T_{j-1}^{\tau}}{\Delta x^{2}} \tag{5.7}$$

$$\text{First order time derivative (backward difference):}\ \frac{\partial T}{\partial t}\cong\frac{T_{j}^{\tau}-T_{j}^{\tau-1}}{\Delta t} \tag{5.8}$$

Once we have replaced all derivative terms contained in Eq. (2.42), with Eqs. (5.6), (5.7) and (5.8), we obtain the following finite difference model of the temperature distribution in a porous medium over space and time:

$$\underbrace{[\epsilon(\rho c_p)_f + (1-\epsilon)(\rho c)_s]}_{\langle \rho c \rangle} \frac{T_j^{\tau+1} - T_j^{\tau}}{\delta t} + u(\rho c_p)_{air} \frac{T_{j+1}^{\tau+1} - T_{j-1}^{\tau+1}}{2\Delta x} =$$

$$= \lambda_{eff} \frac{T_{j+1}^{\tau+1} - 2T_j^{\tau+1} + T_{j+1}^{\tau+1}}{\Delta x^2} \quad (5.9)$$

Eq. (5.9) is the field discrete equation for a general heat transfer problem in a one-dimensional and macroscopically homogeneous domain. Velocity, at this early stage, is considered as a parameter of the problem: it is a fixed value, independent of boundary conditions. The solution of the problem at the time step $\tau+1$ is obtained reversing the coefficient matrix

$$\{T_n\}^{\tau+1} = \underline{\underline{A}}_{imp}^{-1} \{T_n\}^{\tau} .$$

5.1.1 Field equation

Dealing now with the actual algorithm, in its first version it has been developed for a multilayer porous wall. Considering the $j-th$ node of the $i-th$ layer of the technical solution, the approximated field equation, evaluated over τ and $\tau+1$ time steps, is:

$$\langle \rho c \rangle_i \frac{T_{i,j}^{\tau+1} - T_{i,j}^{\tau}}{\Delta t} + u(\rho c_p)_{air} \frac{T_{i,j+1}^{\tau+1} - T_{i,j-1}^{\tau+1}}{2\Delta x} =$$

$$= \lambda_{eff,i} \frac{T_{i,j+1}^{\tau+1} - 2T_{i,j}^{\tau+1} + T_{i,j+1}^{\tau+1}}{\Delta x^2} \qquad \begin{cases} i = 1 \dots N \\ \\ j = 1 \dots M_i - 1 \end{cases} \quad (5.10)$$

where N is the total number of porous layers, and M_i is the total number of nodes contained into the $i-th$ layer. Part of the coefficient matrix $[a_{n,n}]_{imp}$ is than obtained manipulating Eq. (5.10), in order to express the τ value of the temperature in the $j-th$ node, as a function of the $\tau+1$ one in the nodes $j-1$, j and $j+1$, according to the following equation:

$$T_{i,j}^{\tau} = T_{i,j+1}^{\tau+1}\left[u\frac{(\rho c_p)_{air}}{\langle\rho c\rangle_i}\frac{\Delta t}{2\Delta x_i} - \frac{(\lambda)_{eff,i}}{\langle\rho c\rangle_i}\frac{\Delta t}{\Delta x_i^2}\right] + \\ + T_{i,j}^{\tau+1}\left[1 + \frac{(2\lambda)_{eff,i}}{\langle\rho c\rangle_i}\frac{\Delta t}{\Delta x_i^2}\right] + \\ + T_{i,j-1}^{\tau+1}\left[-u\frac{(\rho c_p)_{air}}{\langle\rho c\rangle_i}\frac{\Delta t}{2\Delta x_i} - \frac{(\lambda)_{eff,i}}{\langle\rho c\rangle_i}\frac{\Delta t}{\Delta x_i^2}\right] \quad (5.11)$$

Finally, it is important to notice that $\lambda_{eff,i}$ is the effective thermal conductivity in a one-dimensional domain, as it is defined in Eq. (2.44). Thermal tortuosity and dispersion are calculated for the $i-th$ layer according to the corresponding correlation, as discussed in Chapters 3 and 4.

5.1.2 Boundary conditions

Boundary conditions for the heat transfer differential problem under discussion have been defined using the finite volume method: for every geometrical discontinuity (external and internal surface, interface between adjacent layers), the energy balance for a reference volume has been defined, according to the following general

equation:

$$\frac{1}{dt}\int_{\overline{V}_i} \rho_i \cdot c_i \cdot T_i \cdot dV = -\sum_{j=1}^{N_{sj}} \int_{A_{si}} \phi_{j\to i} \cdot n_{ij} \cdot dS + \int_{\overline{V}_i} \sigma_i \cdot dV \tag{5.12}$$

where $\phi_{j\to i}$ are the generic incoming thermal fluxes, coming from the adjacent volumes $\overline{V}_j$ into $\overline{V}_i$ through the N_{sj} interface surfaces, and σ_i represents energy sources or sinks. Going more in detail with the problem under discussion, in Figure 5.1 a graphical description of the approach adopted to define boundary conditions is reported.

For illustrative purposes, in Figure 5.1(a) a two layers wall have been considered. In Figure 5.1(b) the external surface node is treated, considering both temperature and radiation boundary conditions (respectively, the external air temperature T_e and the incident solar radiation φ_{sol}); for the internal boundary, in Figure 5.1(d), the air temperature T_i in given. Discrete equations and coefficients have than been derived as follows:

- External boundary condition (BC-E - Figure 5.1(b))

$$\langle \rho c \rangle_1 \frac{T_{1,0}^{\tau+1} - T_{1,0}^{\tau}}{\Delta t}\frac{\Delta x_1}{2} = h_e\left(T_{ext}^{\tau+1} - T_{1,0}^{\tau+1}\right) + \frac{\lambda_{eff,1}}{\Delta x_1}\left(T_{1,1}^{\tau+1} - T_{1,0}^{\tau+1}\right) + \\ + u(\rho c_p)_{air}[T_{ext}^{\tau+1} - \underbrace{T_{\frac{1}{2}}^{\tau+1}}_{\frac{T_{1,0}^{\tau+1}+T_{1,1}^{\tau+1}}{2}}] + \alpha_1 \varphi_{sol}^{\tau+1} \tag{5.13}$$

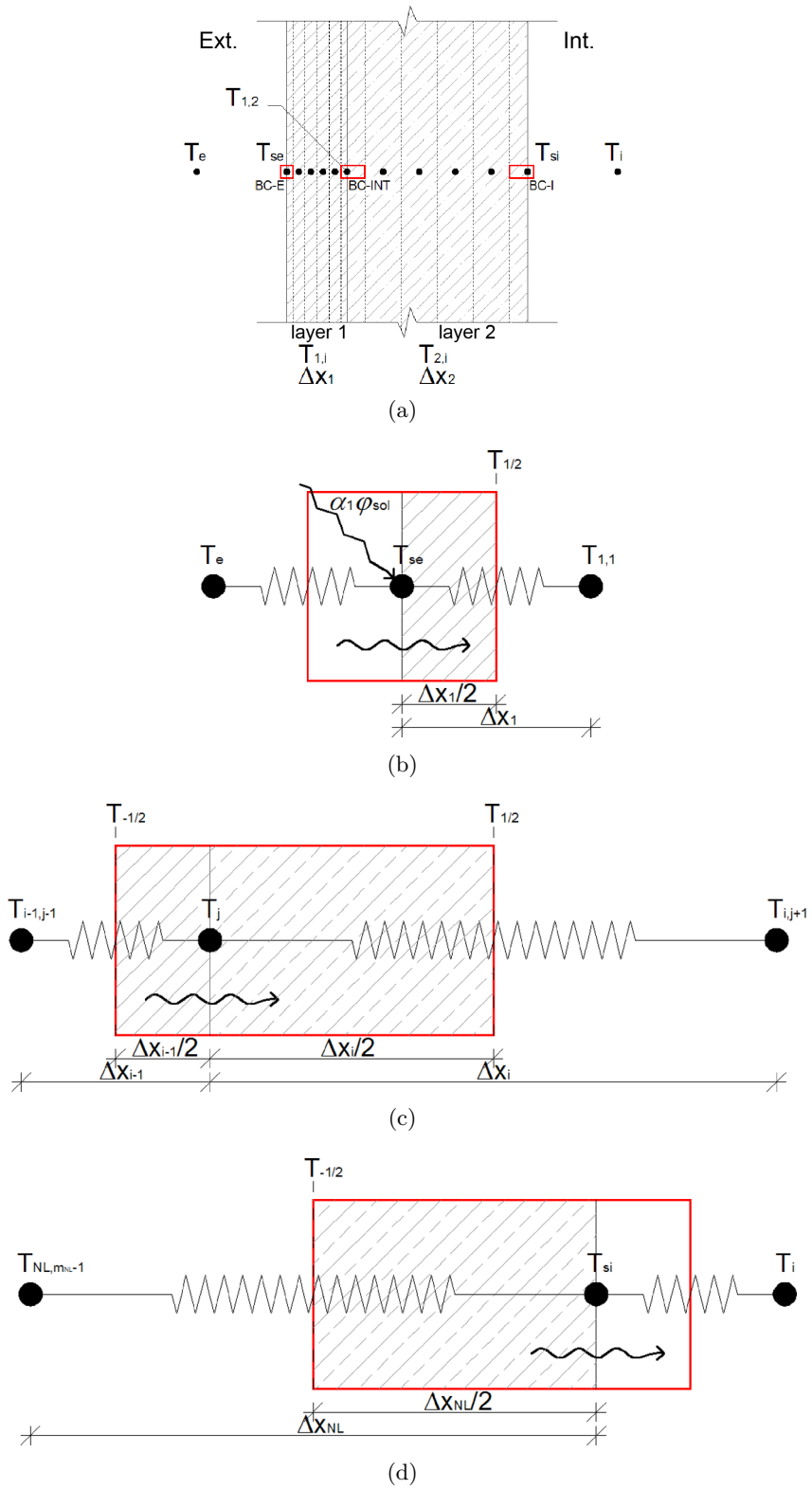

Figure 5.1: (a) Calculus domain discretization. (b) Integration volume for the external boundary condition. (c) Integration volume for the interface between two adjacent layers of the wall. (d) Integration volume for the internal boundary condition.

$$T_{1,1}^{\tau+1}\left[u\frac{(\rho c_p)_{air}}{\langle\rho c\rangle_1}\frac{\Delta t}{\Delta x_1}-\frac{2\lambda_{eff,1}}{\langle\rho c\rangle_1}\frac{\Delta t}{\Delta x_1^2}\right]+$$
$$+T_{1,0}^{\tau+1}\left[1+\frac{2h_e}{\langle\rho c\rangle_1}\frac{\Delta t}{\Delta x_1}+\frac{2\lambda_{eff,1}}{\langle\rho c\rangle_1}\frac{\Delta t}{\Delta x_1^2}+u\frac{(\rho c_p)_{air}}{\langle\rho c\rangle_1}\frac{\Delta t}{\Delta x_1}\right]+$$
$$+T_{ext}^{\tau+1}\left[-2u\frac{(\rho c_p)_{air}}{\langle\rho c\rangle_1}\frac{\Delta t}{\Delta x_1}-\frac{2h_e}{\langle\rho c\rangle_1}\frac{\Delta t}{\Delta x_1}\right]=T_{1,0}^{\tau}+\frac{2\Delta t}{\langle\rho c\rangle_1\Delta x_1}\alpha_1\varphi_{sol}^{\tau+1} \quad (5.14)$$

where $T_{1,0}^{\tau}$ is the external surface temperature T_{se} at the $\tau-th$ time step.

- Interface between adjacent layers (BC-INT - Figure 5.1(c))

$$\underbrace{\langle\rho c\rangle_{i-1,i}}_{\frac{\Delta x_{i-1}(\rho c_p)_{i-1}+\Delta x_i(\rho c_p)_i}{\Delta x_{i-1}+\Delta x_i}}\frac{T_j^{\tau+1}-T_j^{\tau}}{\Delta t}\underbrace{\langle\Delta x\rangle_{i-1,i}}_{\frac{\Delta x_{i-1}+\Delta x_i}{2}}=$$
$$=\frac{\lambda_{eff,i-1}}{\Delta x_{i-1}}\left(T_{i-1,j-1}^{\tau+1}-T_j^{\tau+1}\right)+\frac{\lambda_{eff,i}}{\Delta x_i}\left(T_{i,j+1}^{\tau+1}-T_j^{\tau+1}\right)+$$
$$+u(\rho c_p)_{air}[\underbrace{T_{-\frac{1}{2}}^{\tau+1}}_{\frac{T_{i-1,j-1}^{\tau+1}+T_j^{\tau+1}}{2}}-\underbrace{T_{\frac{1}{2}}^{\tau+1}}_{\frac{T_j^{\tau+1}+T_{i,j+1}^{\tau+1}}{2}}] \quad (5.15)$$

$$T_{i,j+1}^{\tau+1}\left[\frac{u}{2}\frac{(\rho c_p)_{air}}{\langle\rho c\rangle_{i-1,i}}\frac{\Delta t}{\langle\Delta x\rangle_{i-1,i}}-\frac{\lambda_{eff,i}}{\langle\rho c\rangle_{i-1,i}}\frac{\Delta t}{\langle\Delta x\rangle_{i-1,i}\Delta x_i}\right]+$$
$$+T_j^{\tau+1}\left[1+\frac{\lambda_{eff,i-1}}{\langle\rho c\rangle_{i-1,i}}\frac{\Delta t}{\langle\Delta x\rangle_{i-1,i}\Delta x_{i-1}}+\frac{\lambda_{eff,i}}{\langle\rho c\rangle_{i-1,i}}\frac{\Delta t}{\langle\Delta x\rangle_{i-1,i}\Delta x_i}\right]+$$
$$+T_{i-1,j-1}^{\tau+1}\left[-\frac{u}{2}\frac{(\rho c_p)_{air}}{\langle\rho c\rangle_{i-1,i}}\frac{\Delta t}{\langle\Delta x\rangle_{i-1,i}}-\frac{\lambda_{eff,i-1}}{\langle\rho c\rangle_{i-1,i}}\frac{\Delta t}{\langle\Delta x\rangle_{i-1,i}\Delta x_{i-1}}\right]=T_j^{\tau} \quad (5.16)$$

where the $j-th$ node represents the interface between layers $i-1$ and i.

- Internal boundary condition (BC-I - Figure 5.1(d))

$$\langle \rho c \rangle_N \frac{T^{\tau+1}_{N,M_N} - T^{\tau}_{N,M_N}}{\Delta t} \frac{\Delta x_N}{2} = h_i \left(T^{\tau+1}_{int} - T^{\tau+1}_{N,M_N} \right) + \\ + \frac{\lambda_{eff,N}}{\Delta x_N} \left(T^{\tau+1}_{N,M_N-1} - T^{\tau+1}_{N,M_N} \right) + u(\rho c_p)_{air} [\underbrace{T^{\tau+1}_{-\frac{1}{2}}}_{\frac{T^{\tau+1}_{N,M_N-1} + T^{\tau+1}_{N,M_N}}{2}} - T^{\tau+1}_{i}] \quad (5.17)$$

$$T^{\tau+1}_{int} \left[2u \frac{(\rho c_p)_{air}}{\langle \rho c \rangle_N} \frac{\Delta t}{\Delta x_N} - \frac{2h_i}{\langle \rho c \rangle_N} \frac{\Delta t}{\Delta x_N} \right] + \\ + T^{\tau+1}_{N,M_N} \left[1 + \frac{2h_i}{\langle \rho c \rangle_N} \frac{\Delta t}{\Delta x_N} + \frac{2\lambda_{eff,N}}{\langle \rho c \rangle_N} \frac{\Delta t}{\Delta x_N^2} + v_x \frac{(\rho c_p)_{air}}{\langle \rho c \rangle_N} \frac{\Delta t}{\Delta x_N} \right] + \\ + T^{\tau+1}_{N,M_N-1} \left[-u \frac{(\rho c_p)_{air}}{\langle \rho c \rangle_N} \frac{\Delta t}{\Delta x_N} - \frac{2\lambda_N}{\langle \rho c \rangle_N} \frac{\Delta t}{\Delta x_N^2} \right] = T^{\tau}_{N,M_N} \quad (5.18)$$

where T^{τ}_{N,M_N} is the internal surface temperature T_{si} at the $\tau - th$ time step.

5.1.3 The coefficient matrix

The numerical method discussed leads to the definition of the coefficient matrix, which links, in an implicit way, nodal temperature values at the $\tau + 1$ time step with correspondent ones at the τ time step.

As a result, we obtain the tridiagonal coefficient matrix represented in Figure 5.2. Some considerations can be done: first of all, the first and the last element of the main diagonal are equal to 1 and are aimed at the description of external and internal thermal conditions. Therefore, correspondent values of the known terms vector have to be equal to $T_e^{\tau+1}$ and $T_i^{\tau+1}$. Secondly, coefficients obtained with

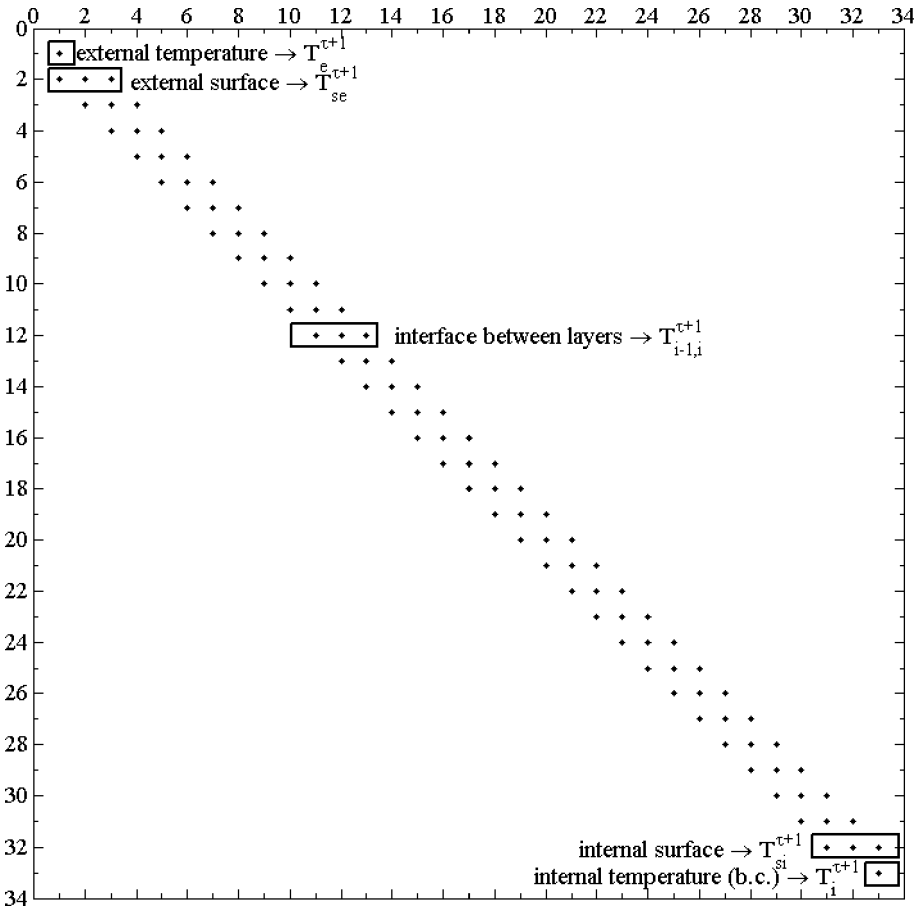

Figure 5.2: Representation of the not-null elements of the tridiagonal coefficient matrix $a_{n,n}$ defined for a double-layered domain. The number of rows and columns depends on the number of nodes in the spatial grid.

Eqs. (5.14) and (5.18) appear into the second and the penultimate row. Concerning again the known terms vector, its second element have to be affected from solar radiation, as it is possible to understand from Eq. (5.14).

5.2 A numerical model for dynamic insulation walls

We have now to remember that the simulation algorithm under discussion has been developed in order to perform time dependent numerical simulations of buildings with dynamic insulation technical solutions. This means that the algorithm

has to be able to reproduce realistic stratigraphies.

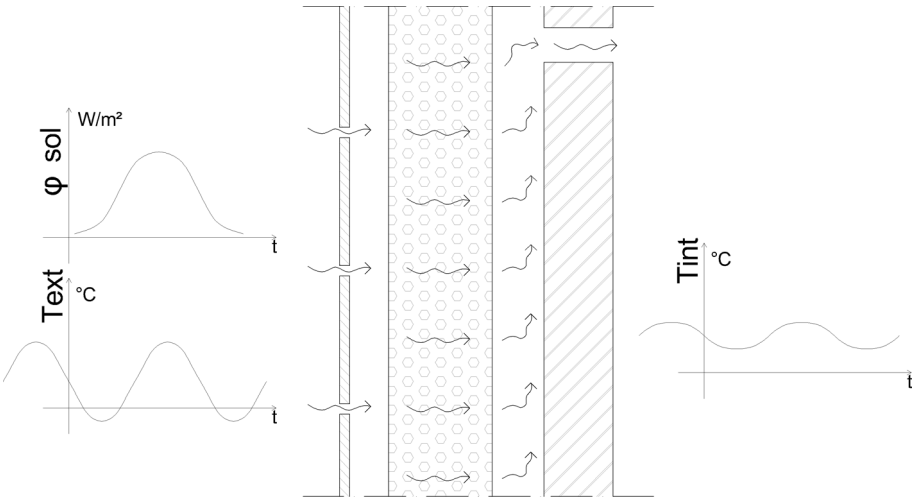

Figure 5.3: Wall schematization and boundary conditions. From left to right we have the external shield, the external ventilated cavity, the external air permeable layers, the internal ventilated cavity and the internal not permeable layers. On the top of the right side the connection with the ventilation system is represented.

Therefore, we have introduced some changes to the stratigraphy treatment: while the previous approach was concerned with a fully permeable wall (every layer is made of a open cell porous material), in this new version we have introduced an external shield, such as a ventilated façade, which purpose is the protection of the underlying porous layer from climatic agents. In this way, the model takes into account that the flowing air which crosses permeable layers is taken from the external cavity, and its temperature may be different from the actually external one.

Moreover, we have take in to account that porous layers have to be protected on the inner side too: indeed, building users may not accept an air flow coming from wall surfaces. For this reason, we have introduced a internal not permeable facing, which could be made of bricks with plaster coating, gypsum plasterboard, etc. The internal layers introduced lead than to the formation of an air cavity between permeable and not permeable layers. From the technological point of view, this

cavity will be linked to channels of the ventilation system. The wall schematization is represented in Figure 5.3.

Internal layers are than numerically treated with a null air velocity: therefore, the reference differential equation is not Eq. (2.42), but the well known Fourier equation [44].

Modifications introduced have led to a modified set of discrete equations for the coefficient matrix definition.

5.2.1 The energy equation modeling

The problem modeled at this stage is different from the previous one from some point of view: first of all, not only permeable layers are taken into account. This means that we have to introduce another field equation to evaluate nodal values of temperature. Secondly, we have to model the thermal behavior of both internal and external cavities. Lastly, we have defined new boundary conditions and modified some o previous ones, in order to take into account the new sequence of layers.

Field equation

As far as the field equation is concerned, we have to make a distinction between permeable domain and not permeable domain: the first one is still described by the discrete Eq. (5.10), which correspondent coefficients are calculated according Eq. (5.11). Conversely, the not permeable sub-domain finite difference full-implicit equation is:

$$\langle \rho c \rangle_i \frac{T_{i,j}^{\tau+1} - T_{i,j}^{\tau}}{\Delta t} = \lambda_i \frac{T_{i,j+1}^{\tau+1} - 2T_{i,j}^{\tau+1} + T_{i,j+1}^{\tau+1}}{\Delta x^2} \qquad \begin{cases} i = N+1 \dots L \\ j = 1 \dots M_i - 1 \end{cases} \tag{5.19}$$

$$\begin{aligned} T_{i,j}^{\tau} = T_{i,j+1}^{\tau+1} \left[-\frac{(\lambda)_i}{\langle \rho c \rangle_i} \frac{\Delta t}{\Delta x_i^2} \right] + \\ + T_{i,j}^{\tau+1} \left[1 + \frac{(2\lambda)_i}{\langle \rho c \rangle_i} \frac{\Delta t}{\Delta x_i^2} \right] + \\ + T_{i,j-1}^{\tau+1} \left[-\frac{(\lambda)_i}{\langle \rho c \rangle_i} \frac{\Delta t}{\Delta x_i^2} \right] \end{aligned} \tag{5.20}$$

where L is the number of not permeable layers in the wall under discussion.

Boundary conditions

In order to model dynamic insulation multi-layered walls, new boundary conditions have been introduced, according to Figure 5.4. The analytical procedure involved to define differential equations is the same previously described for the first version of the simulation algorithm.

For what concerns the external side of the wall, we have introduced the following approximation: since no simple and reliable physical models of ventilated façade have been found in literature, we have decided to neglect the external shield contribution to the heat transfer phenomenon, in terms of thermal resistance and time shift (Figure 5.4(a)). Therefore, we only take into account its shielding effect, only reducing the superficial heat transfer coefficient, between the outermost permeable layer and the outside air, in Eq. (5.14). Its is assumed to be equal to the internal

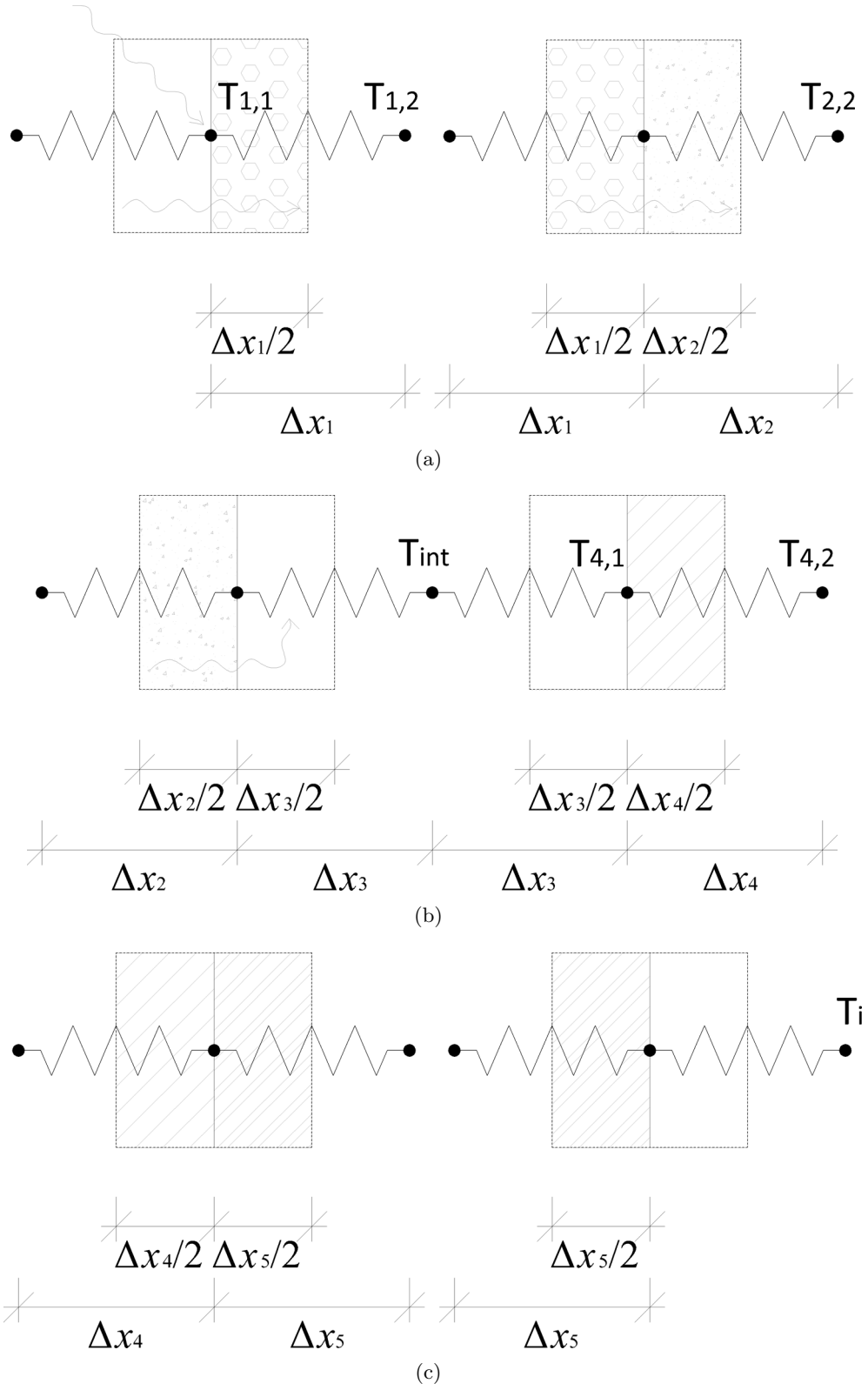

Figure 5.4: Control volumes used for boundary conditions definition: (a) external cavity interface, interface between two adjacent permeable layers, (b) interface between a permeable layer and the internal cavity, the interface between the internal cavity and a not permeable layer, (a) the interface between two adjacent not permeable layers, and the internal boundary condition.

one, as suggested in [45]:

$$h_e = h_i = 7.7\frac{W}{m^2K}.$$

Interface between two adjacent permeable layers (Figure 5.4(a)) is treated in the same way previously presented, according to Eq. (5.16). Conversely, the interface between the internal porous layer and the internal cavity has been introduced (Figure 5.4(b)): in order to simplify the calculus procedure, we have represented the cavity as a single node, which temperature (T_{cav}) is equal to the arithmetic average between superficial temperature. Therefore we have:

$$\begin{aligned}\langle\rho c\rangle_N \frac{T^{\tau+1}_{N,M_N} - T^{\tau}_{N,M_N}}{\Delta t}\frac{\Delta x_N}{2} &= h_i^*\left(T^{\tau+1}_{cav} - T^{\tau+1}_{N,M_N}\right) + \\ &+ \frac{\lambda_{eff,N}}{\Delta x_N}\left(T^{\tau+1}_{N,M_N-1} - T^{\tau+1}_{N,M_N}\right) + v_x(\rho c_p)_{air}[\underbrace{T^{\tau+1}_{-\frac{1}{2}}}_{\frac{T^{\tau+1}_{N,M_N-1}+T^{\tau+1}_{N,M_N}}{2}} - T_i^{\tau+1}] \quad (5.21)\end{aligned}$$

$$\begin{aligned}T^{\tau+1}_{cav}&\left[2v_x\frac{(\rho c_p)_{air}}{\langle\rho c\rangle_N}\frac{\Delta t}{\Delta x_N} - \frac{2h_i^*}{\langle\rho c\rangle_N}\frac{\Delta t}{\Delta x_N}\right] + \\ &+ T^{\tau+1}_{N,M_N}\left[1 + \frac{2h_i^*}{\langle\rho c\rangle_N}\frac{\Delta t}{\Delta x_N} + \frac{2\lambda_{eff,N}}{\langle\rho c\rangle_N}\frac{\Delta t}{\Delta x_N^2} + v_x\frac{(\rho c_p)_{air}}{\langle\rho c\rangle_N}\frac{\Delta t}{\Delta x_N}\right] + \\ &+ T^{\tau+1}_{N,M_N-1}\left[-v_x\frac{(\rho c_p)_{air}}{\langle\rho c\rangle_N}\frac{\Delta t}{\Delta x_N} - \frac{2\lambda_{eff,N}}{\langle\rho c\rangle_N}\frac{\Delta t}{\Delta x_N^2}\right] = T^{\tau}_{N,M_N} \quad (5.22)\end{aligned}$$

where h_i^* is the heat transfer coefficient referred to the internal cavity. Its definition will be further discussed. The interface between the internal cavity and the first not permeable layer (Figure 5.4(b)) is characterized by the following equation:

$$\langle \rho c \rangle_{N+1} \frac{T^{\tau+1}_{N+1,0} - T^{\tau}_{N+1,0}}{\Delta t} \frac{\Delta x_{N+1}}{2} = \\ = h^*_i \left(T^{\tau+1}_{cav} - T^{\tau+1}_{N+1,0} \right) + \frac{\lambda_{N+1}}{\Delta x_{N+1}} \left(T^{\tau+1}_{N+1,1} - T^{\tau+1}_{N+1,0} \right) \quad (5.23)$$

$$T^{\tau+1}_{N+1,1} \left[-\frac{2\lambda_{N+1}}{\langle \rho c \rangle_1} \frac{\Delta t}{\Delta x_{N+1^2}} \right] + \\ + T^{\tau+1}_{N+1,0} \left[1 + \frac{2h^*_i}{\langle \rho c \rangle_{N+1}} \frac{\Delta t}{\Delta x_{N+1}} + \frac{2\lambda_{N+1}}{\langle \rho c \rangle_{N+1}} \frac{\Delta t}{\Delta x^2_{N+1}} \right] + \\ + T^{\tau+1}_{cav} \left[-\frac{2h^*_i}{\langle \rho c \rangle_{N+1}} \frac{\Delta t}{\Delta x_{N+1}} \right] = T^{\tau}_{N+1,0} \quad (5.24)$$

where the subscript $N+1$ represent the first not permeable layer of the wall. Than, the interface between two adjacent layers of this kind is treated as follows (Figure 5.4(c)):

$$\underbrace{\langle \rho c_p \rangle_{i-1,i}}_{\frac{\Delta x_{i-1}(\rho c_p)_{i-1} + \Delta x_i (\rho c_p)_i}{\langle \Delta x \rangle_{i-1,i}}} \frac{T^{\tau+1}_j - T^{\tau}_j}{\Delta t} \underbrace{\langle \Delta x \rangle_{i-1,i}}_{\frac{\Delta x_{i-1} + \Delta x_i}{2}} = \\ = \frac{\lambda_{i-1}}{\Delta x_{i-1}} \left(T^{\tau+1}_{i-1,j-1} - T^{\tau+1}_j \right) + \frac{\lambda_i}{\Delta x_i} \left(T^{\tau+1}_{i,j+1} - T^{\tau+1}_j \right) \quad (5.25)$$

$$T_{i,j+1}^{\tau+1}\left[-\frac{\lambda_i}{\langle\rho c_p\rangle_{i-1,i}}\frac{\Delta t}{\langle\Delta x\rangle_{i-1,i}\,\Delta x_i}\right]+ \\ +T_j^{\tau+1}\left[1+\frac{\lambda_{i-1}}{\langle\rho c_p\rangle_{i-1,i}}\frac{\Delta t}{\langle\Delta x\rangle_{i-1,i}\,\Delta x_{i-1}}+\frac{\lambda_i}{\langle\rho c_p\rangle_{i-1,i}}\frac{\Delta t}{\langle\Delta x\rangle_{i-1,i}\,\Delta x_i}\right]+ \\ +T_{i-1,j-1}^{\tau+1}\left[-\frac{\lambda_{i-1}}{\langle\rho c_p\rangle_{i-1,i}}\frac{\Delta t}{\langle\Delta x\rangle_{i-1,i}\,\Delta x_{i-1}}\right]=T_j^{\tau} \quad (5.26)$$

where the subscript i for the central node considered has been dropped, because it represents the interface surface, and is not possible to attribute it unequivocally to a layer. Finally, the internal boundary condition equation is the following (Figure 5.4(c)):

$$\langle\rho c\rangle_L\frac{T_{L,M_L}^{\tau+1}-T_{L,M_L}^{\tau}}{\Delta t}\frac{\Delta x_L}{2}=h_i\left(T_{int}^{\tau+1}-T_{L,M_L}^{\tau+1}\right)+ \\ +\frac{\lambda_L}{\Delta x_L}\left(T_{L,M_L-1}^{\tau+1}-T_{L,M_L}^{\tau+1}\right)+ \quad (5.27)$$

$$T_{int}^{\tau+1}\left[-\frac{2h_i}{\langle\rho c\rangle_L}\frac{\Delta t}{\Delta x_L}\right]+ \\ +T_{L,M_L}^{\tau+1}\left[1+\frac{2h_i}{\langle\rho c\rangle_N}\frac{\Delta t}{\Delta x_N}+\frac{2\lambda_L}{\langle\rho c\rangle_L}\frac{\Delta t}{\Delta x_L^2}\right]+ \\ +T_{L,M_L-1}^{\tau+1}\left[-\frac{2\lambda_L}{\langle\rho c\rangle_L}\frac{\Delta t}{\Delta x_L^2}\right]=T_{L,M_L}^{\tau} \quad (5.28)$$

where T_{L,M_L} is internal surface of the $L-th$ layer and, therefore, the internal surface of the wall.

The internal cavity treatment

As previously stated, the internal air cavity is approximated with a single temperature node and is treated using the simplified approach of a single air gap thermal resistance split in two equal parts, in order to take into account the overall effects of convective and radiative heat transfer.

Dealing with the convective part of the resistance ($1/h_{cv}$), we have searched in literature for some semi-empirical correlations with the Nusselt number related to a weakly ventilated cavity. In [44] we have found:

$$Nu_{cav} = 4.86; \tag{5.29}$$

therefore we have:

$$h_{cv} = \frac{\lambda_{air} Nu_{cav}}{L_{cav}}; \tag{5.30}$$

where L_{cav} is the cavity thickness expressed in meters.

As far as the radiative heat transfer coefficient h_{rd} is concerned, we have introduced the dependence on superficial temperatures of cavity internal and external surfaces, and on their emissivity ϵ. Therefore, the heat transfer problem across the air cavity becomes non-linear, and an iterative method for numerical solution is needed. The radiative heat transfer coefficient is calculated as follows:

$$h_{rd} = \sigma \cdot \frac{\left(T_{s,ext}^2 + T_{s,int}^2\right) \cdot \left(T_{s,ext} + T_{s,int}\right)}{\frac{1}{\epsilon_{s,ext}} + \frac{1}{\epsilon_{s,int}} - 1} \tag{5.31}$$

where σ is the Stefan-Boltzmann constant and is equal to $5.67 \cdot 10^{-8} \frac{W}{m^2 K^4}$, $T_{s,ext}$

and $T_{s,int}$ are the superficial temperatures of the external and the internal surface of the air cavity respectively, $\epsilon_{s,ext}$ and $\epsilon_{s,int}$ are correspondent values of emissivity. With this approach, it is possible to evaluate the effects of low-emission coating, such as aluminum films, on the overall heat transfer phenomenon: in fact, this kind of solution can be considered interesting from the technological point of view, in order to solve thermal comfort issues due to superficial temperature reduction, as it has been noticed in literature [7, 8, 12].

Finally, once that h_{cv} and h_{rd} are calculated, the thermal resistance for the cavity is then as follows:

$$R_{cav} = \frac{1}{h_i^*} = \frac{1}{h_{cv} + h_{rd}} \tag{5.32}$$

5.2.2 The velocity field evaluation

While the previous version of the simulation algorithm, according to the simplified approach presented in literature [3–5, 7, 8], is treated as a simple boundary condition not depending on anything else, we have introduced the evaluation of the filter velocity, as defined in §2.3, as a function of pressure difference between indoor and outdoor, according to semi-empirical correlations described in Eqs. (3.1) and (4.7).

It is important to underline that the algorithm under discussion is aimed at the time-dependent simulation of permeable multi-layer walls. This means that the velocity calculation would have to be performed in the same way, according to Eq. (2.29). Further analyses have been performed to evaluate the opportunity of a quasi-static approach to the problem.

Numerical analysis

The first step of this study has been the numerical discretization of the time-dependent velocity equation (2.29), using permeability and Ergun coefficient referred to no-fines concrete (§4.3.1). The main purpose is to evaluate the relaxation time of the equation, for a step-wise pressure drop boundary condition. The numerical approximation of the simplified momentum equation is:

$$\frac{\rho}{\varepsilon}\frac{u_D^{\tau+1}-u_D^{\tau}}{\Delta\tau} = -\frac{d\langle p\rangle^f}{dx} - \frac{\mu}{K}u_D^{\tau} - \frac{C_E}{K^{1/2}}\rho\,|u_D^{\tau}|\,u_D^{\tau} \tag{5.33}$$

where the time dependency has been treated with a fully-explicit approach. Then, assuming that the pressure gradient remains constant through the domain thickness L, we can consider $\frac{d\langle p\rangle^f}{dx} = \frac{\Delta P}{L}$. In this way the old pore pressure gradient term in Eq. (2.29) is used as boundary condition in the approximated momentum equation. Therefore we can write:

$$u_D^{\tau+1} = -\frac{\varepsilon\cdot\Delta\tau}{\rho}\left(\frac{\Delta P}{L} + \frac{\mu}{K}u_D^{\tau} + \frac{C_E}{K^{1/2}}\rho\,|u_D^{\tau}|\,u_D^{\tau}\right) + u_D^{\tau} \tag{5.34}$$

It can be noticed that the final discrete equation does not depend on the spatial coordinate x. A MATLAB® code has been written in order to solve Eq. (5.34), for different transient conditions of pressure drop: a step-wise condition is imposed, than the relaxation time is evaluated. It is defined as the time required by the numerical solution to reach the 99.99% of the velocity value in steady state condition, after a sudden change of boundary condition (from 0 to non-0 Pa/m of pressure drop). Results are reported in Figure 5.5.

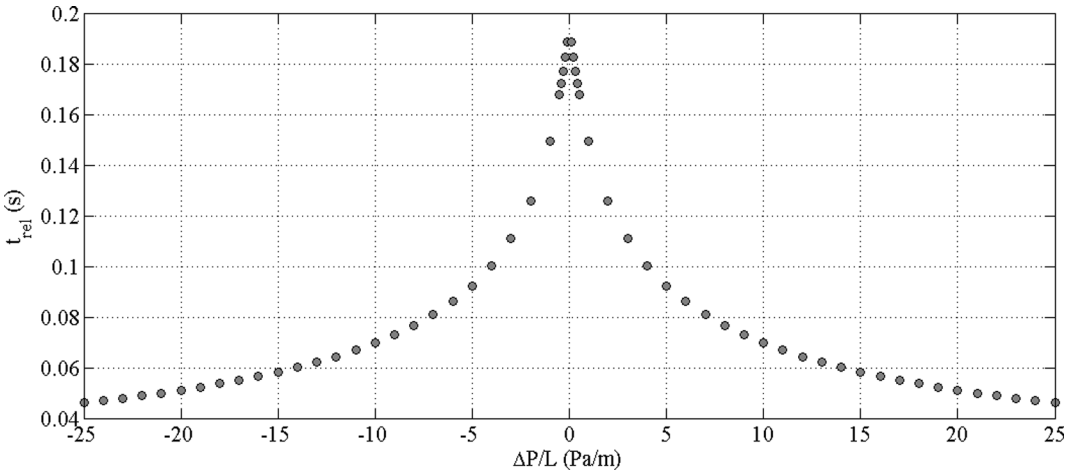

Figure 5.5: Relaxation time of the numerical problem, as a function of pressure drop boundary condition. Incoming and outgoing flows have been considered.

The range of velocity values obtained is wider than the working range of dynamic insulation systems (generally around ± 0.003 m/s), which corresponds to a ∓ 1 Pa/m (with a minimum of ∓ 0.3 Pa/m) of pressure drop range. The resulting relaxation time obtained is between 0.15 s and 0.18 s. This means that, simulating the energy performance of a dynamic insulation for variable temperature boundary condition with an hourly time step, it will be possible to treat the solution of the velocity field with a steady state approach.

Order-of-magnitude analysis

To confirm numerical results, a dimensionless analysis has been performed. First of all, some reference quantities have been defined; than, dimensionless variables (both dependent and independent) have been derived; finally, a order-of-magnitude analysis of coefficients has been performed to understand if the time dependent term was negligible or not. Fixing P_{diff} as the differential pressure between left and right domain boundaries (and, therefore, dependent on the domain thickness L),

reference quantities and dimensionless variables are:

$$\text{velocity: } V = \sqrt{\frac{P_{diff}}{\rho}} \quad \Rightarrow \quad u^* = \frac{u_D}{V}$$

$$\text{pressure: } p^* = \frac{p}{P_{diff}}$$

$$\text{length: } x^* = \frac{x}{L}$$

$$\text{time: } t^* = \frac{L}{V}$$

Manipulating Eq. (2.29) we obtain:

$$\frac{\rho}{\varepsilon}\frac{V^2}{L}\frac{\partial u^*}{\partial t^*} = -\frac{P_{diff}}{L}\frac{\partial p^*}{\partial x^*} - V\frac{\mu}{K}u^* - V^2\frac{C_E}{K^{1/2}}\rho\,|u^*|\,u^*$$

$$\frac{\rho}{\varepsilon}\frac{P_{diff}}{\rho L}\frac{\partial u^*}{\partial t^*} = -\frac{P_{diff}}{L}\frac{\partial p^*}{\partial x^*} - \sqrt{\frac{P_{diff}}{\rho}}\frac{\mu}{K}u^* - \frac{P_{diff}}{\rho}\frac{C_E}{K^{1/2}}\rho\,|u^*|\,u^*$$

$$\frac{\partial u^*}{\partial t^*} = -\varepsilon\frac{P_{diff}}{L}\frac{L}{P_{diff}}\frac{\partial p^*}{\partial x^*} - \varepsilon\sqrt{\frac{P_{diff}}{\rho}}\frac{L}{P_{diff}}\frac{\mu}{K}u^* - \varepsilon\frac{P_{diff}}{\rho}\frac{L}{P_{diff}}\frac{C_E}{K^{1/2}}\rho\,|u^*|\,u^*$$

$$\frac{\partial u^*}{\partial t^*} = -\varepsilon\frac{\partial p^*}{\partial x^*} - \underbrace{\frac{\mu\varepsilon L}{K\sqrt{P_{diff}\rho}}}_{\alpha}u^* - \underbrace{\varepsilon\frac{C_E L}{K^{1/2}}}_{\beta}|u^*|\,u^* \tag{5.35}$$

With Eq. (5.35) the velocity field is treated in a nondimensional form. The numerical order-of-magnitude analysis of α and β coefficients for $\frac{P_{diff}}{L} = 0.25 \div 1$ Pa/m and $L = 0.1 \div 0.3$ m is reported in Figure 5.6.

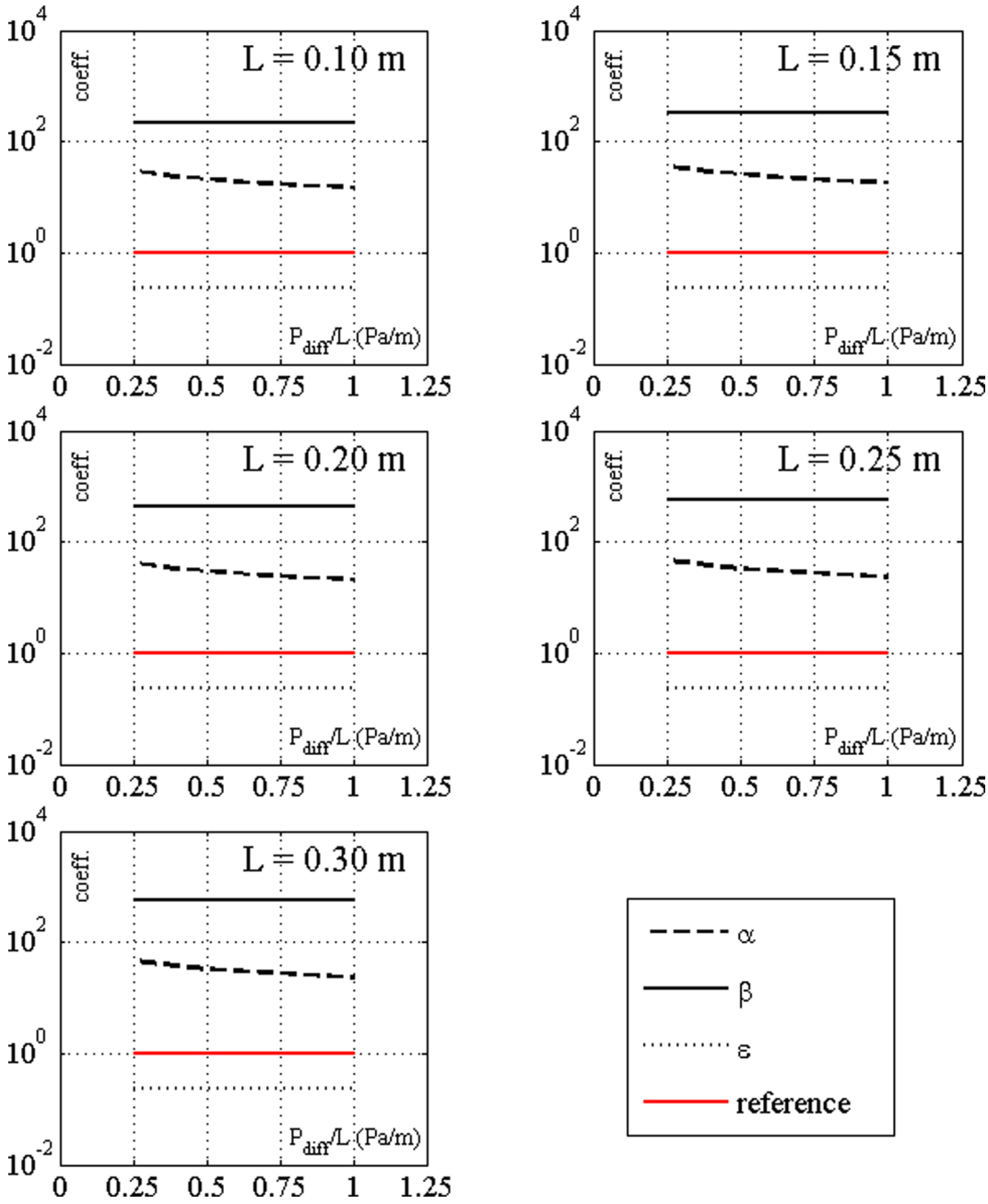

Figure 5.6: Order of magnitude analysis of α and β coefficients in Eq. (5.35). The *reference* line represents the coefficient of the dimensionless time derivative (equal to one).

As we can see, α and β are one or two order of magnitude bigger than the coefficient of the time dependent term (which in Eq. (5.35) assumes the value 1).

Results

Thanks to numerical and nondimensional analyses previously discussed, it is possible to affirm that in the range of pressure drop and wall thickness useful for this kind of technical solution, the time derivative term in Eq. (2.29) can be neglected in the numerical simulation of air permeable walls under variable boundary conditions. Therefore, a quasi-static approach to the solution of the fluid dynamic problem can be considered enough reliable.

5.2.3 Simulation results

For illustrative purpose only, some results of a numerical simulation performed are now presented.

Going more in detail, we have simulated e multi-layered wall in winter climate conditions. The indoor environment has been considered with constant temperature (T_{int} = 21 °C, as if a heating plant would be active), while for the external temperature boundary condition time dependent values have been imposed. On the external surface, also an incident solar radiation is considered. For hourly values of boundary conditions refer to Figure 5.7.

Layer thermophysical and geometrical properties are reported below in Table 5.1. When porosity is higher than zero the layer is considered permeable, and density, thermal conductivity and specific heat are referred to the solid matrix only; while in other cases are intended as *nominal* quantities taken from data sheets.

Taking into account superficial radiative properties, the external shield absorbance is equal to 0.3 (light-colored surface); while the emissivity of both surfaces of the internal cavity is equal to 0.9. Finally, resultant value of velocity is

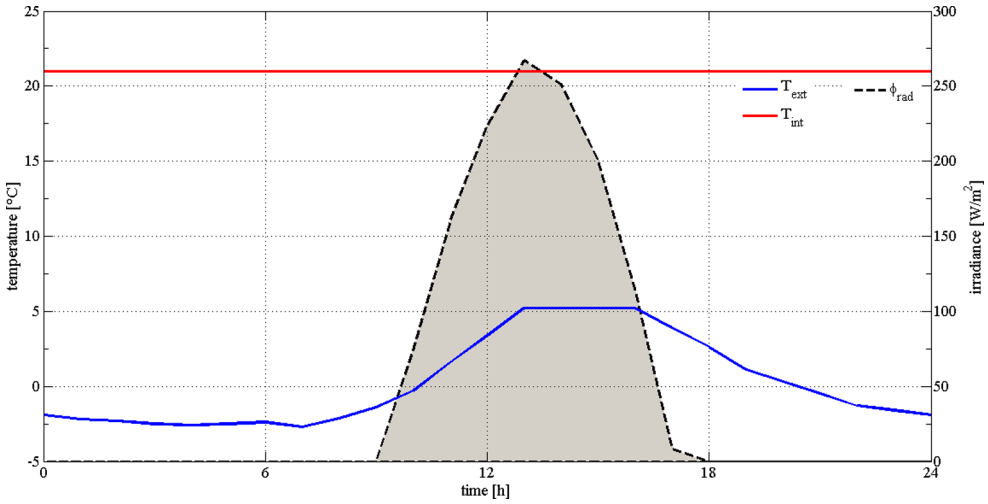

Figure 5.7: Internal and external boundary conditions for temperature and irradiance in winter conditions.

Table 5.1: Wall thermophysical end geometrical properties.

ID	material	ε [-]	ρ $[\frac{kg}{m^3}]$	λ $[\frac{W}{m^2K}]$	c_{sp} $[\frac{J}{kgK}]$	s s	$n^{\circ}{}_{nodes}$
1	fibrous insulation	0.98	2872	1.750	910	0.10	21
2	no-fines concrete	0.23	1824	2.101	815	0.15	31
3	air cavity		1.188	0.026	1006	0.05	1
4	gypsum plasterboard	0	1000	0.350	840	0.025	5
5	insulation	0	80	0.039	840	0.05	11
6	gypsum plasterboard	0	1000	0.350	840	0.025	5

approximately equal to 0.001 m/s.

The simulation has been performed for a period of seven days, repeating boundary conditions previously presented. Results for superficial temperature over time are reported in Figure 5.8, referred to internal and external surfaces, and to interfaces between main layers. Considering the nature of example of the simulation presented, a detailed analysis of the results obtained is not reported.

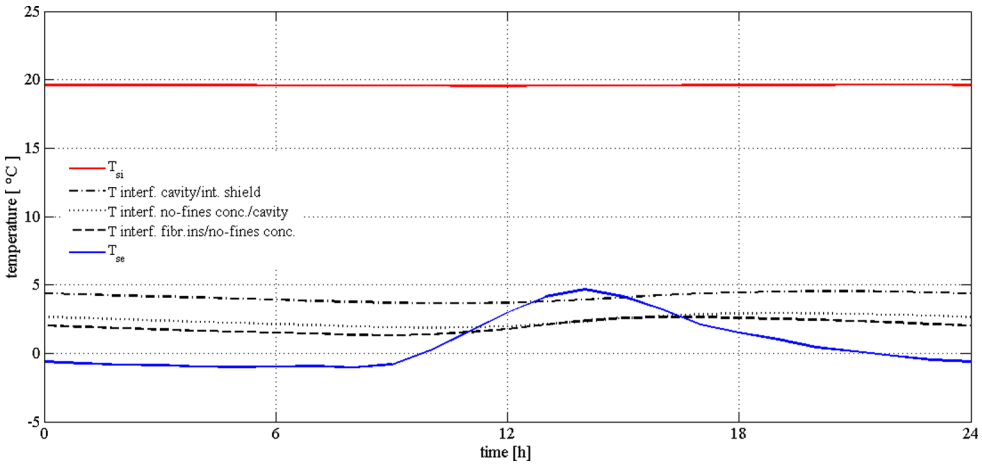

Figure 5.8: Temperature values obtained for the main surfaces of the wall.

5.3 Development of a TRNSYS Type

The main purpose of the numerical simulation algorithm previously discussed is the development of a TRNSYS© simulation *modulus*, also known as *Type* [46].

Almost every complex transient energy problem can be modeled by dividing it into some *elementary* problems, each of which is solved by a dedicated Type. A Type behaves as a black box: the calculus algorithm elaborates *inputs* (time dependent) and *parameters* (constant and user-defined), and returns *outputs*.

The building thermal behavior in transient conditions is modeled by a dedicated software called TRNbuild: it allows the user to define boundary conditions, envelope and partition technical solutions, ventilation rates and internal gains, in order to represent as accurately as possible the real building. Therefore, the main issue in defining a new numerical model aimed at wall simulation is the integration process with the whole building model developed in TRNbuild.

In fact, with this software technical solutions are treated with the transfer function technique and their corresponding coefficient are defined one-off before the

simulation process starts. Than, the main problem is to allow the information exchange between the building model and the dynamic insulation simulation Type.

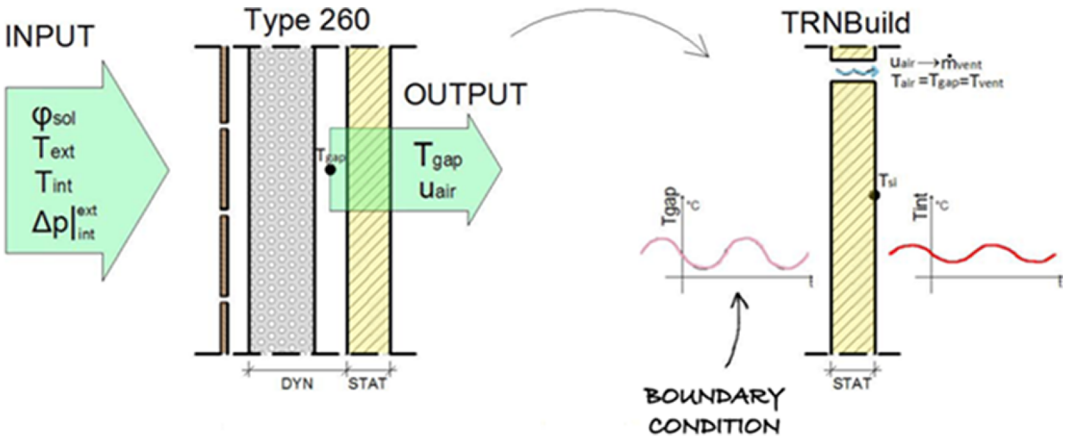

Figure 5.9: Representation of the integration between the Type for dynamic insulation modeling (finite differences) and the generic building model developed in TRNbuild (transfer functions).

The solution for this problem has been achieved using the following workaround: the dedicated Type simulates the whole building, considering as internal boundary condition the operative temperature coming from the TRNbuild model of the building. In the building model, only the not permeable part (internal shield) of a dynamic insulation wall is modeled, using the *BOUNDARY* option. Therefore, the Type passes to TRNbuild the temperature value related to the internal cavity node. In this way, after some unavoidable iterations, a convergent solution is reached.

Moreover, the internal air cavity temperature is used by the building numerical model to evaluate the ventilation air temperature and, consequently, to calculate the energy need related to air change of the enclosed environments considered. A simple schematization of the integration process is reported in Figure 5.9.

5.4 Conclusions and final remarks

In this Chapter, the development of a finite difference algorithm for the time dependent numerical simulation of multi-layered permeable walls have been presented.

More in detail, the development process is based on three key steps: first of all, we have implemented a MATLAB® code aimed at the simulation of permeable layers based on the volume average approach presented in previous chapters, with a constant velocity value given by the user.

These restrictions have been eliminated in the second version of the calculus procedure, where the simulation of not-permeable layers have been implemented, together with the velocity dependence on pressure difference between indoor and outdoor. Moreover, the ability to model external and internal cavities has been introduced: while the first kind is treated as a simple reduction of the heat transfer coefficient (considered now equal to that related to enclosed environment), for the second kind we have treated separately convective and radiative heat transfer. In this way, it is possible to evaluate effects of low-emissivity coatings on the overall heat transfer performance.

Finally, this last version of the algorithm has been used to develop a component for the TRNSYS® calculus suite: in this way, it is possible to evaluate the performance of the technology under discussion when it is integrated with a building, taking into account possible effects of control strategies, boundary conditions, etc.

In this Chapter, only few results have been presented, just with illustrative purpose: in order to be used for design and research oriented simulations, the

developed tool has to be validated. First of all, as we have stated in Chapter 3 and 4, all correlations used for the evaluation of effective thermal conductivity have to be compared with empirical data. The same operation would have to be performed over the whole algorithm, in order to check the reliability of the numerical model. Finally, the TRNSYS® Type has to be tested too, with the main purpose to assess the numerical consistency of the integration with the TRNbuild building model.

Taking into account the empirical validation of results previously presented, Chapter 6 introduces the design and construction of an experimental arrangement expressly developed for this purpose.

Chapter 6

The Dual Air Vented Thermal Box (DAVTB) apparatus

In previous chapters, the characterization of porous media that can be used for the construction of breathable walls has been described. All empirical and numerical correlations, as well as the simulation algorithm, need an experimental validation. Therefore, an experimental apparatus has been built in the Building Physics Laboratory of the Energy Department of Politecnico di Milano.

Going more in detail, the design process has been inspired by the *hotbox* arrangement presented in [11]. While the laboratory test arrangement found in literature is only able to reproduce a steady-state wall behavior, our apparatus have been designed with the purpose to test multi-layered building components under both transient or steady state boundary conditions.

Hence, the apparatus under discussion have been expressly developed with three main objectives: first of all, the validation of thermal tortuosity and dispersion

correlations presented in Chapter 3 and 4; secondly, the assessment of the numerical model robustness, as it has been described in Chapter 5; finally, the experimental arrangement can be used to study optimized technical solutions for various boundary conditions.

6.1 The apparatus

The apparatus under discussion can be considered as a sort of small double climatic chamber: it is mainly composed by two insulated chambers divided by the sample and connected by the ventilation system. Temperature can be controlled in each chambers separately, and the air flow can be controlled both in velocity and direction. The name of the apparatus, *Dual Air Vented Thermal Box* (*DAVTB*) derives from this features.

6.1.1 Chambers

External dimension of both chambers are 1.5 m $\times$ 1.5 m $\times$ 1.29 m, and wall section is a sandwich made with internal and external laminated coating (4 mm each one) with a polystyrene layer interposed, for a total thickness of 140 mm. Its purpose is to make the envelope as much adiabatic as possible.

Each chamber has two openings: the first, is a missing wall on the side with external dimension of 1.5 m $\times$ 1.5 m, and is used to put chambers in thermal (convective and conductive) contact through the sample, which is placed in the middle. The second opening is a hole on the opposite side, with a diameter of 20 cm, which is used to connect both chambers to the ventilation system.

In Figure 6.1 it is possible to see the chambers, as they have been produced by the

Figure 6.1: Picture of both chambers of the *DAVTB* apparatus as they have been produced by the manufacturer. In the right one the hole for the connection with the ventilation system is visible. The frame for the sample housing is visible too (in the picture is connected to the box on the left side).

manufacturer, in an open configuration: on the right one, the hole for the connection with the ventilation plant (on the back) and the gaskets for the airtightness (on the front) are visible; the steel frame for the sample housing is connected to the chamber on the left side of the picture. It is important to notice that the above mentioned frame can be completely detached from the rest of the apparatus, to allow the user to mount or unmount samples under study.

6.1.2 Heating and cooling plant

Temperature conditions in each chamber are controlled in an independent way, by a heating and cooling plant.

Going more in detail, this plant is linked to the central supply of the Energy Department building (*primary plant*) through two water tanks (Figure 6.2(a)), which have a dual purpose. First o all, they have to provide hot and cold water, thanks to

internal coil heat exchangers, to the part of the plant directly connected to the apparatus (*secondary plant*). Secondly, they allow us to decouple primary and secondary plants to facilitate any maintenance operation.

The secondary plant consists of three circuits similar to each other: two are used to provide thermally treated water to chambers; the third is connected to a heat exchanger in the ventilation system of the apparatus. In each of these circuit, the supply temperature to the corresponding terminal is controlled independently: hot and cold water coming from tanks are mixed in appropriate proportion to obtain a set-point temperature, which can be defined dynamically and can change during one experimental test, by acting on two servo valves for each circuit: the first is a mixing valve upstream of the delivery terminals; conversely, the other one is a diverter downstream (in Figure 6.2(b) the electrical actuators are visible).

As far as delivery terminals are concerned, two main kind can be identified: as mentioned before, in the ventilation plant there is a heat exchanger, which can act as a hot or cold battery either. The second kind is located directly into each of the two chambers, and consists of five radiant panels per chamber, connected in parallel. Every panel has been made with copper strips for solar collectors, like that in Figure 6.3(a), properly combined and connected (Figure 6.3(b)).

In order to promote the radiative heat exchange, thermal emissivity of the inner surface of each panel has been painted with a matte black ferromicaceous varnish. The new thermal emissivity has than been estimated by means of thermographic measurements: superficial temperature of a painted plate has been measured with thermocouples and a thermal imaging camera at the same time; the right value of emissivity is that which allows to obtain in both cases the same measured value. At

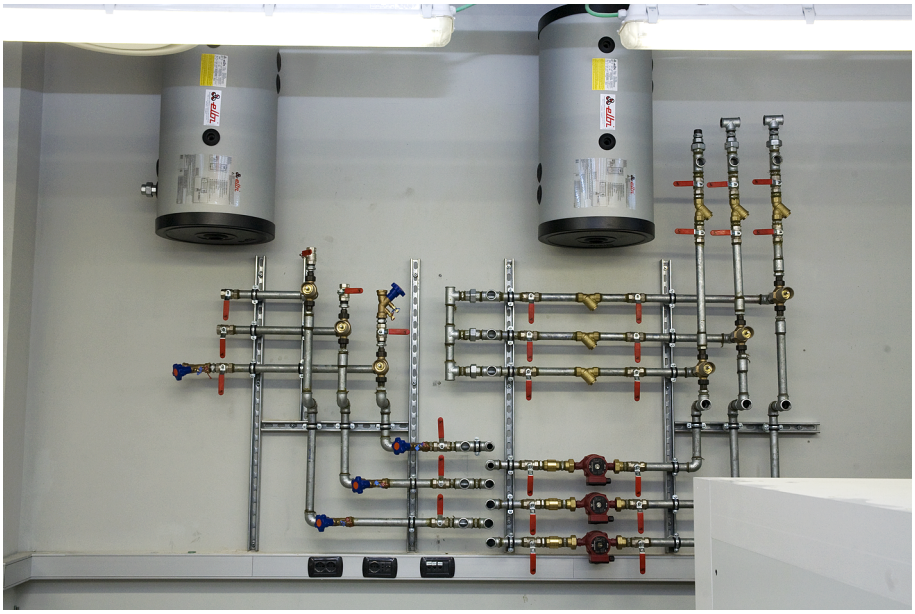

(a)

(b)

Figure 6.2: (a) Detail of tanks, in a early stage of the building procedure. (b) Main part of the water plant and the end of the building process.

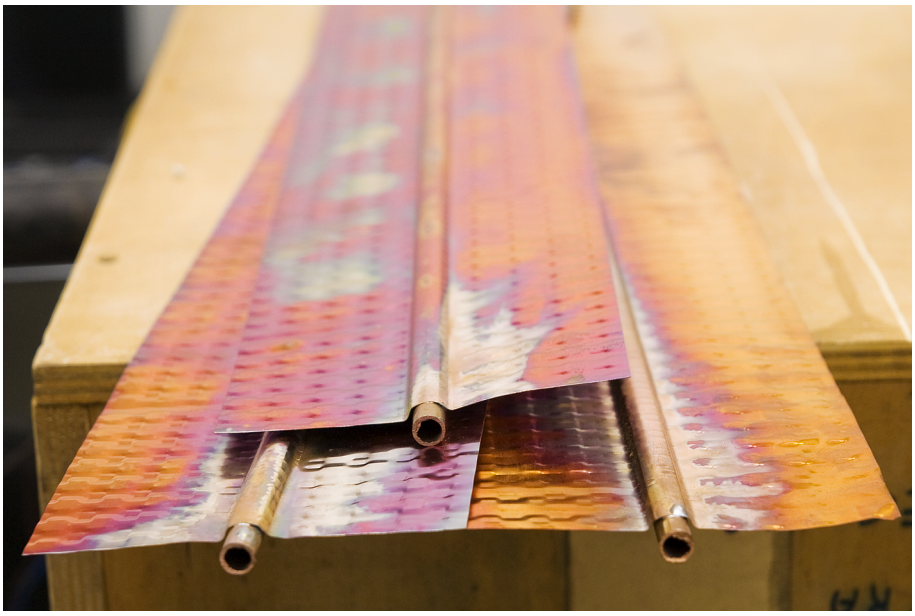

(a)

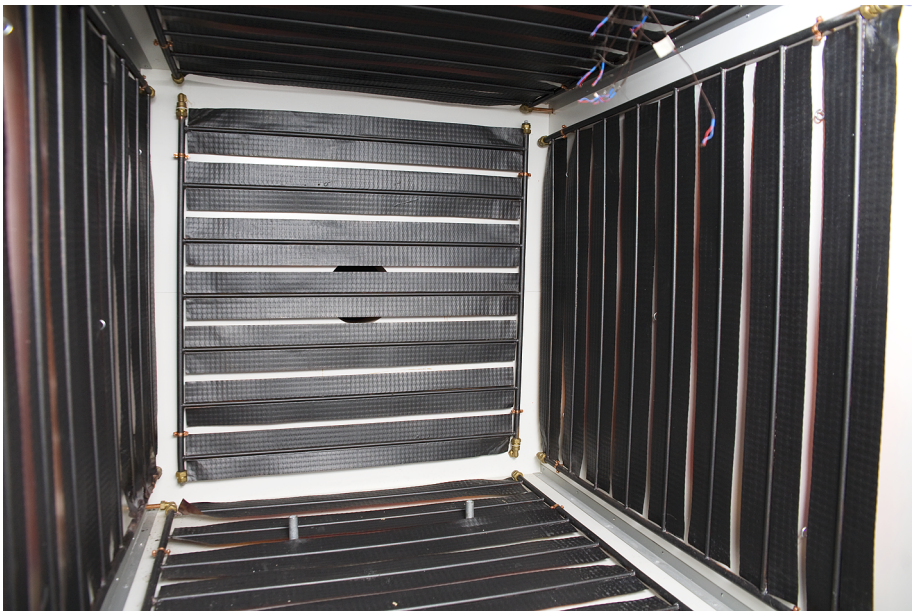

(b)

Figure 6.3: (a) Original appearance of copper solar strips. (b) Radiant panels assembled and mounted in one of the two chambers. Inward surfaces are painted with ferromicaceous varnish, to increase thermal emissivity.

the end, the emissivity is assumed to be equal to $0.92 \div 0.94$, which is grater than the usual value for copper ($0.01 \div 0.07$ when it is not oxidized).

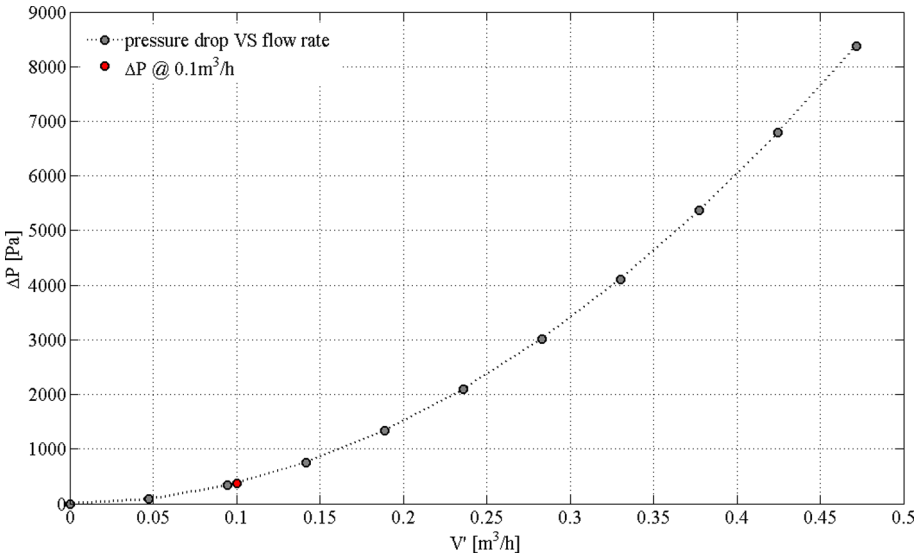

Figure 6.4: Pressure drop, referred to water flow rate, due to one of the radiant panels installed. The whole water flow rate circulating inside each chamber is around 0.5m ^{3}/h, therefore the fraction that passes through each panel is around 0.1 m^3/h, which gives a pressure loss of 365 Pa.

In each of the three circuits, water is moved by an electric three speeds pump, visible in Figure 6.2(a). In order to allow the sizing of these devices, the pressure loss due to each radiant panel has been evaluated numerically as a function of the water flow rate. The resulting curve is reported in Figure 6.4.

6.1.3 Ventilation system

The main function of the apparatus under discussion is the experimental analysis of dynamic insulation systems. In order to allow that, the air flow has to be guaranteed through the sample. For this reason, we have designed and built a ventilation system which connects the two chambers.

Going more in detail, the plant is divided into three main parts: the first one

is related to the heat exchanger previously described. The second part, is the fan section represented in Figure 6.5(b), which has been designed to allow the control of the air flow in terms of velocity and direction. In fact, this section consists of two parallel fans, facing in opposite direction, and two butterfly damper for each fan: one, with a ON/OFF control, insulates the circuit branch; the other, with a proportional control, regulates air flow rate. As far as fans are concerned, they are originally designed for computer equipment: as it is possible to see in Figure 6.5(a), they are centrifugal devices, with a PWM velocity control to allow a precise setting of air flow rate in the apparatus (48 Pa ÷ 560 Pa at 30.6 m^3/h ÷ 106.2 m^3/h).

While in the most part of the ventilation system channels have a diameter between 160 mm and 200 mm, in the third section it decreases to 50 mm. Indeed, this section consists of a 2 m long tube (visible in Figure 6.6) used to measure air flow rate, thanks to a small fan anemometer put in the middle: with this probe, the air velocity on the central axis of the tube is measured; than, assuming a laminar regime, the air flow rate can be inferred and, finally, the air velocity through the sample can be estimated.

6.2 Probes and control devices

The whole apparatus is automatically driven by a multifunctional switch unit, which is remotely controlled by a LabVIEW® algorithm. The multifunctional switch is an Agilent 34980A, equipped with following modules:

3×34921A/T - 40-Channel Armature Multiplexer: used for data measurement (temperature, air velocity, differential pressure) by means of voltage

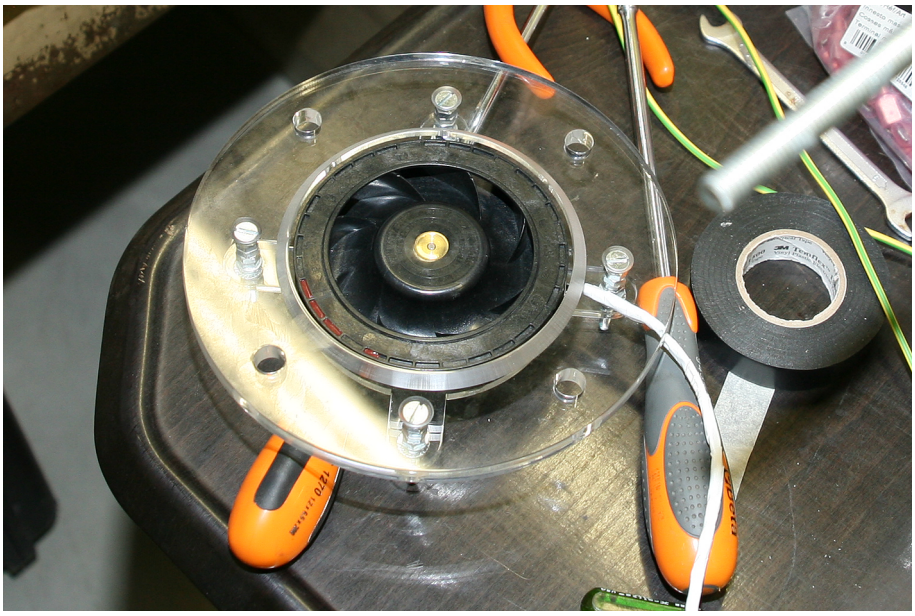

(a)

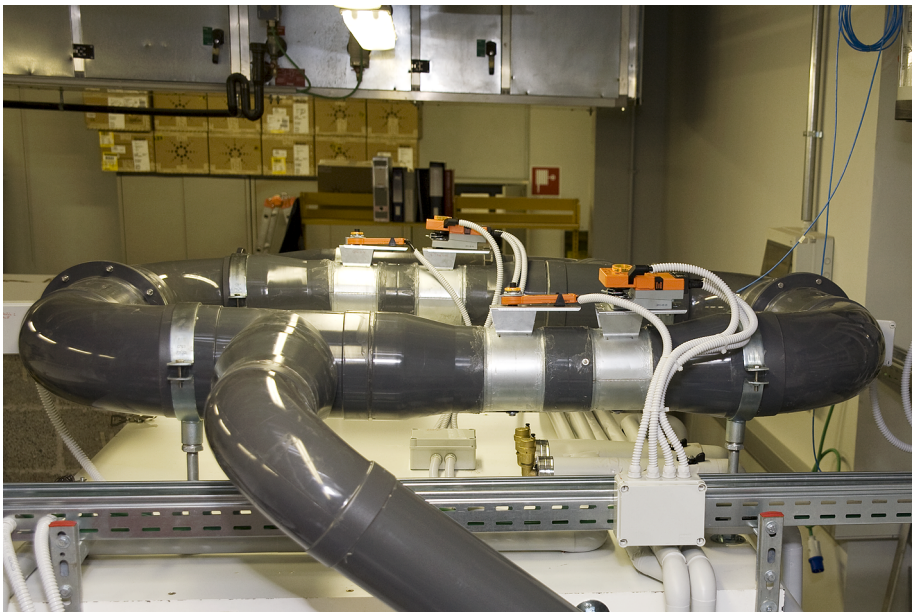

(b)

Figure 6.5: (a) One of the fans installed. The perspex frame used to mount it inside the channel is visible. (b) The ventilating section of the system. Fans are hidden into the channels in correspondence of the flanges (on the left and the right side of the picture). Damper actuators are also visible.

Figure 6.6: Picture of the overall apparatus at the end of the construction process. The measurement section is visible.

and current metering.

2×34951A/T 4-Channel D/A Converter with Waveform Memory: is used to control proportional actuators, generating a voltage or a current output. It is also able to generate waveforms, used for the PWM control of fans.

1×34938A/T 20-Channel 5A Form A Switch: is used to control ON/OFF actuators and the power supply of all electrical devices (through relays inside the control cabinet).

As fare as the measurement of environmental parameters is concerned, following probes have been adopted:

- a differential micromanometer for the measurement of the pressure difference between the two chambers straddling the sample;
- the aforementioned bidirectional fan anemometer (± 20 m/s - fan diameter ≅

10 mm);

- a series of thermocouples for the measurement of temperature in the two chambers (9 + 9 measuring points) and in the channel for air recirculation (one upstream of the fan section, one downstream of the heating and cooling coil);
- 16 needle thermocouples embedded in the hydraulic circuits and in the cool and warm tanks (Figure 6.2(b));
- 55 thermocouples embedded inside the concrete sample.

Every thermocouple in the experimental arrangement is a type T (copper-constantan), and has been calibrated in two main steps: the first is a thermostatic bath, filled with saturated ice obtained from demineralized water (temperature around 0 °C). The other step is a variable temperature measurement: the temperature of demineralized water is risen to around 65 °C in a thermally insulated container with a heating system, based on an electrical resistance. Than, the heat source is turned off, and a slow free-cooling process begins. In this way, the water inside the container cools down until it reaches thermal equilibrium with the surrounding environment (around 25 °C). In both calibration steps, the temperature of water is measured with thermocouples and a Pt100 thermoresistance, calibrated in a laboratory with the SIT accreditation (*Servizio Italiano di Taratura* - Italian Calibration Service), used as a reference element.

The thermocouples are connected to the multiplexer through a terminal block with a built-in thermocouple reference junction, which is used to obtain a direct measurement of temperature after the thermocouple signal is read. Therefore, the

internal reference junction gives a temperature value which has to be equal for all thermocouples connected (maximum 40 elements): if the connection in inside the terminal block is not isothermal, a measurement error is introduced. For this reason, we have adopted two precautions: first of all, we have detached all terminal blocks from the multifunctional switch unit. Indeed, the cooling system of this device produces hot air which can affect the temperature uniformity of terminal blocks. Secondly, we have built a small insulated and airtight box to contain terminal blocks. These expedients should ensure nearly isothermal junction of thermocouples on the terminal block, increasing the accuracy of measurement.

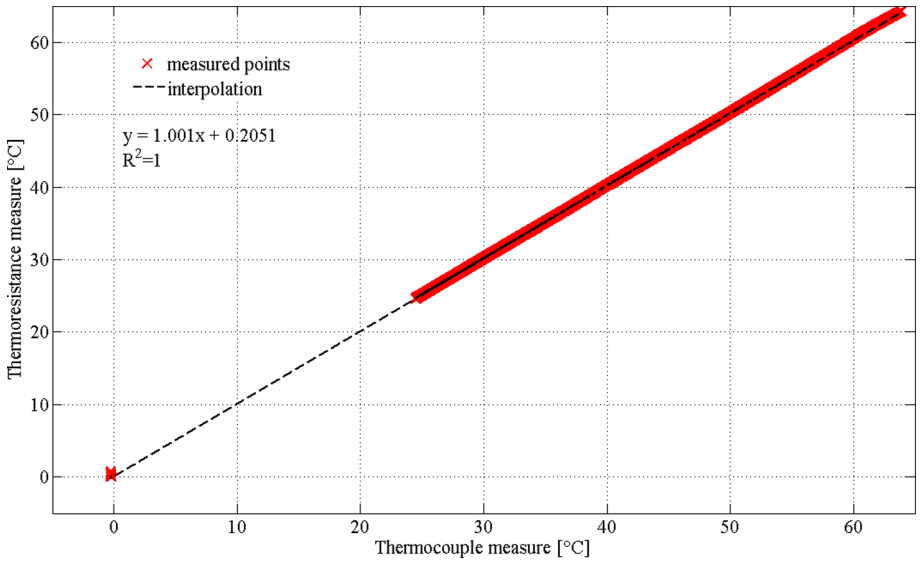

Figure 6.7: Comparison between temperature measurement performed with the reference thermoresistance and one of the thermocouple calibrated. The regression equation (with both slope and intercept) is given.

Finally, the regression linear equation to correlate both measurements have been found, obtaining a slope and a intercept, both representing the error in the temperature measuring with thermocouples. In Figure 6.7 the result of the calibration of one thermocouple is represented for illustrative purpose.

6.3 The no-fines concrete sample

Simultaneously with the construction of the experimental apparatus, we have built a wall sample made of no-fines concrete blocks, visible in Figure 6.8. It has a frontal area of about 1 m^2, and a thickness of 15 cm. Because of its considerable weight, this sample has been divided into 9 elements (32 cm $\times$ 32 cm $\times$ 15 cm) of two kinds: the first 4 blocks, represented in Figure 6.9(a), have no thermocouples inside. They have been built only for filling purposes, and have been used also to measure pressure drops as a function of filter velocity, as described in §4.3.1. Conversely, the other 5 blocks (Figure 6.9(b)) have 9 thermocouples embedded in each of them, arranged parallel to the thickness with a wheelbase of 1.5 cm, and 2 thermocouples attached to the exposed surfaces. In this way, the temperature distribution in these blocks will be monitored during every laboratory test. It is important to notice that the casting procedure has been performed carefully, not to damage the embedded junction of the thermocouple; moreover, distance between these probes has been measured, trying to reduce possible uncertainties during future experimental tests.

Figure 6.8: Wall sample made of no-fines concrete blocks. The edge insulation made of polystyrene slices is visible.

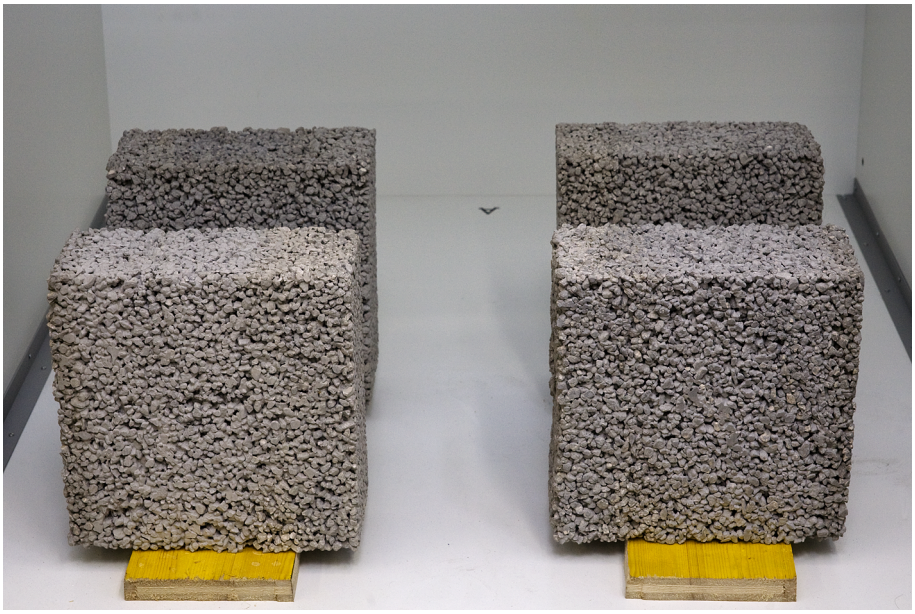

(a)

(b)

Figure 6.9: (a) Four samples without thermocouples. (b) One of the no-fines blocks during the casting procedure. Embedded junctions of thermocouples are visible.

The mix design used for each block is the same employed to prepare cubic samples for the image analysis of this material, described in §4.1.1. After their hardening, they have been bounded by means of mortar layers. Moreover, in order

to ensure a unidirectional heat flux during tests, some slices of polystyrene have been put the external edge of the sample, to make the metal frame as much adiabatic as possible.

6.4 Conclusions and final remarks

In this Chapter the development of an experimental apparatus has been presented. The main purposes of this device are: first of all, the experimental validation of numerical correlations described in Chapter 3 and 4. This will allow us to verify the reliability of the volume average method, compared to the simplified one proposed in literature, in dealing with heat transfer in porous media.

Secondly, it will be possible to check the consistency of the numerical model implemented to simulate air permeable walls. Going more in detail, thanks to the particular design of the heating and cooling plant of the apparatus under discussion, we will be able to reproduce either steady-state or transient thermal conditions, representative for winter and summer environmental conditions respectively.

Finally, it will be useful to optimize a multilayer technical solution for building envelope under climate conditions typical for Mediterranean countries: in fact, it will be possible to optimize the stratigraphy of the wall and the control strategy of the ventilation system (which will be the scaled representation of the ventilation plant of a real building), in order both to reduce energy needs for heating or cooling the enclosed environment and to ensure adequate conditions for thermal comfort (acceptable values for the temperature of the internal surface).

Going more in detail about the optimization of the control strategy, thanks to

arrangements taken in the realization the ventilating section, it will be possible to revert the direction of the air flow that passes through the sample, allowing us to study the effects of *pro* and *contra-flux* working configurations over the whole energy performance of the wall.

Unfortunately, because of construction delays, it has not been possible to perform any experimental test to be included in this work: all analyses described above will be the subject of future research developments.

Conclusions

Within the research work described in this dissertation, dynamic insulation components for building envelopes have been investigated. As a result of a literature review, following considerations can be done: first of all, the technology seems to be an interesting approach to reduce building energy requirements, thanks to the heating recovery effect related to the thermal exchange between the solid matrix and the flowing fluid inside porous layers; secondly, the wall acts as a heat exchanger and a filter of the ventilation plant, and is characterized by a low crossing velocity, which leads to reduced values of pressure loss and, theoretically, to lower energy consumption related to fans. In brief, the high level of integration between building envelope and ventilation system allows the users to dynamically control the energy behavior of walls. Furthermore, earlier studies have noticed that the main issue related to this technology, when it works in a *contra-flux* configuration in winter, is the reduction of the internal surface temperature, which affects indoor comfort conditions. Along with this, we have found a simplified approach to the treatment of heat and mass transfer in porous media.

Hence, purposes of our research are multiple: first of all, the theoretical study of the physical problem under discussion, with the introduction of a mathemati-

cal approach aimed at the evaluation of the thermal interaction between the fluid and solid phase in porous media. Secondly, the thermophysical characterization of porous materials of some interest in building breathable walls. Moreover, another of our purpose was the development of an algorithm for numerical simulations of dynamic insulation components under transient conditions, which can be useful both for research and design purposes. Finally, since such achievements require an empirical validation to assess their reliability, an experimental apparatus was needed.

As far as the theoretical approach is concerned, after a careful study of dedicated bibliography, the volume average method has been chosen in dealing with the heat transfer problem related to porous media. Going more in detail, the energy equation (2.42) at p. 34, coming from an average procedure performed over a representative elementary volume (REV) of the medium considered, has been used. This equation allows us to consider the problem under discussion from a macroscopic point of view, taking into account microscopic phenomena at the same time, thanks to a corrected value of thermal conductivity, described by Eq. (2.44) at p. 34. This quantity is related to some important parameters: first of all, the thermal conductivities of both the fluid and the solid part of the domain; secondly, its porosity (defined as the volume fraction of the fluid phase). Finally, due to the mathematical approach used, two more quantities appear: one is related to the local values of the temperature deviations from the average value, integrated over the interface between phases (thermal tortuosity - Eq. (2.45)); the other depends on both temperature and velocity deviations from their respective average values, integrated over the fluid volume contained in a REV (thermal dispersion - Eq. (2.46)). These two

parameters, which act as a correction of the mere volume averaged value of thermal conductivity, give rise to the need for an additional set of equations to close the problem. Considering now the mathematical method used to evaluate macroscopic (mediated) values of air velocity inside pores, we have chosen Eq. (2.29), reported at p. 31, where Darcean velocity and pressure gradient are linked by air permeability and Ergun coefficient of the material. As a conclusion of this first part of the study, we have experienced the need for a detailed analysis of some materials, which could be used in building dynamic insulation components. Materials considered are fibrous insulation (e.g. rock wool) and no-fines concrete.

Dealing now with fibrous insulating material, we have first defined a simplified REV, approximating fibers with parallel and ordered arrays of cylinders, orthogonally displaced in relation to fluid flow and thermal flux. This simplification has been considered acceptable at this stage: in fact, the study on this material has been mainly performed to test the volume average approach. Besides, a more detailed analysis would have need a image collection of thin sections of the material involved, which are difficult to produce because of the lack of suitable equipment. The calculus domain has been defined with six levels of porosity, and parametric boundary conditions have been applied for both inlet air velocity and temperature (five values for the first and two values of temperature gradient across the x-coordinate). *Pro* and *contra-flux* configurations have been simulated reverting the temperature gradient, obtaining an amount of 120 CFD simulations performed. Results have been used to calculate both thermal tortuosity (Eq. (3.5) at p. 46) and dispersion (Eq. (3.6) at p. 46), trying to correlate them with macroscopic parameters, such as porosity, Peclet number and temperature gradient. Two regression equations have

then been obtained: tortuosity is calculated as a function of the porosity only, and significantly affects the effective thermal conductivity; dispersion is influenced by Pe too, and its contribution on the overall heat transfer phenomenon can be considered negligible. Temperature gradient seems to have no effect on any of the two quantities. Numerical results have also been used to derive a correlation between pressure drop across the REV and the average air velocity. This analysis has led to the definition of a linear regression equation, which means that the aforementioned momentum equation is reduced to the Darcy equation. Then, the velocity coefficient in such equation (defined as the ratio between air dynamic viscosity and permeability of the material) has been heuristically calculated as a function of porosity.

A similar procedure has been applied in the no-fines concrete treatment. Though, this time a detailed description of the solid matrix geometry has been performed in defining calculus domains: real samples have been produced, cut and used for a photographic survey. Images produced have than been subjected to analyses, aimed at three main purposes: first, the evaluation of porosity; second, the definition of the REV size, obtained not only in comparison to porosity values of subsamples of each image taken, but also to the autocorrelation function of the whole picture itself; third and last goal, the definition of edges from the vectorization of the interface between the solid and the fluid phase (obtained thanks to an edge-detection algorithm). At the end of this process, twelve meshes have been prepared. As it has been done for fibrous insulation, similar parametric boundary conditions for inlet air velocity and temperature gradient have been applied, for an amount of 240 CFD simulations, both for *pro* and *contra-flux* configuration. Hence, thermophysical properties of the compound solid matrix have been obtained by means

of TPS measurements. Again, thermal tortuosity and dispersion have been calculated, and we have tried to relate them to the same macroscopic parameters used for fibrous insulation, using equations of the same form. As far as the tortuosity is concerned, it has not been possible to find any good correlation; therefore, a mean value (p. 76) has been calculated over a filtered set of results (outliers have been found and eliminated). On the contrary, a regression equation with good agreement with numerical results has been found for thermal dispersion (Eq. (4.8) at p.77), which depends again on porosity and Peclet number. Results of CFD simulations have also been used to evaluate a correlation between pressure drop and average velocity: unlike what has been obtained for the fibrous insulation, in this case the regression equation has a quadratic form. Therefore, we have been able to obtain both permeability and Ergun coefficient for no-fines concrete. Numerical results and regression equation have also been validate by means of experimental analysis, performed on parallelepiped-shaped samples, and show a good agreement with empirical data.

Besides the characterization of materials, some efforts have been made in the definition of a simulation algorithm aimed at the evaluation of realistic multi-layered dynamic insulation building components in transient boundary conditions. In order to have a detailed description of the temperature distribution inside the wall, we have decided to implement a one-dimensional finite difference numerical model. More in detail, space derivatives have been approximated with central differences, and time derivative has been treated with a full-implicit approach. All boundary conditions have been derived defining the energy conservation equations over appropriated reference volumes. The numerical model obtained at the end of this work

presents following features: first of all, we have introduced an external cavity, which comes from the fact that, in real technical solutions, insulating layers have to be protected from atmospheric agents that may damage them. The contribution of the external shield has been reduced to the assumption that the heat transfer coefficient is taken equal to the one used for enclosed environments. Secondly, an arbitrary number of air permeable layers can be modeled: all parameters (effective thermal conductivity, permeability and Ergun coefficient) are calculated as a function of user-defined conditions, according to all regression equations previously mentioned. Therefore, only fibrous insulation and no-fines concrete can be implemented at this stage. Thirdly, we have decided to introduce the ability of the numerical model to portray also not-permeable materials, which can be used as an internal screen in real walls. Therefore, in order to allow the air motion through porous layers, we planned the presence of an internal cavity, between permeable and not-permeable layers. This fluid layer has been treated as a single temperature node, and its thermal resistance is calculated considering separately convective and radiative heat transfer. This has led to the ability of the algorithm to evaluate effects of superficial coatings with different values of emissivity, which could be a possible solution for the comfort issue mentioned in literature. In addition to the computation of the temperature distribution, we have implemented the velocity calculation as a function of pressure gradient across the wall. Thanks to both numerical and order-of-magnitude analyses, we have been able to demonstrate that, with typical time steps for walls simulation (0.25h $\div$1.00 h), a quasi-static approach to the velocity evaluation is sufficiently reliable. At the end, the algorithm described has been used to define a TRNSYS® Type, which allows the user to simulate the kind of

wall under discussion when it is integrated in a building, taking into account the effects of all boundary conditions.

Simultaneously with the theoretical and numerical work described above, we have developed an experimental apparatus, aimed at the reproduction of both indoor and outdoor environments, in steady state or transient temperature conditions. Moreover, the ventilation system adopted is able to precisely control air flow in terms of velocity and direction, allowing the user to investigate the effects of *pro* and *contra-flux* configurations. At this stage, a no-fines concrete wall has been built, with 55 embedded thermocouples for the temperature distribution measurement.

In the future, the experimental arrangement will be used to validate all correlations numerically derived, both for fibrous insulation and no-fines concrete, and will allow us to test the consistency of the finite difference model. Moreover, after the validation process is over, it will be possible to search for stratigraphies and control strategies optimized for climate conditions typical for Mediterranean countries.

Bibliography

[1] F.J. Powell and S.L. Matthews. *Thermal insulation: materials and systems*. Powell/Matthews, 1988.

[2] A.M. Omer. Renewable building energy systems and passive human comfort solutions. *Renewable and Sustainable Energy Reviews*, (12):1562–1587, 2008.

[3] B.J. Taylor and M.S. Imbabi. The application of dynamic insulation in buildings. *Renewable Energy*, (15):377–382, 1998.

[4] B.J. Taylor, R. Webster, and M.S. Imbabi. The building envelope as an air filter. *Building and Environment*, (34):353–361, 1999.

[5] M.S. Imbabi. Modular breathing panels for energy efficient, healthy building construction. *Renewable Energy*, (31):729–738, 2006.

[6] B.J. Taylor and M.S. Imbabi. Dynamic insulation in multi-storey buildings. *Building Services Engineering Research and Technology*, 20:179–184, 1999.

[7] B.J. Taylor, D.A. Cawthorne, and M.S. Imbabi. Analytical investigation of the steady-state behaviour of dynamic and diffusive building envelopes. *Building and Environment*, (31):518–525, 1996.

[8] G. Gan. Numerical evaluation of thermal comfort in rooms with dynamic insulation. *Building and Environment*, (35):445–453, 2000.

[9] M. Krarti. Effect of air flow on heat transfer in walls. *Journal of Solar Energy Engineering*, 116:35–42, 1994.

[10] J. Brunsell. The performance of dynamic insulation in two residential buildings. *Air Infiltration Review*, 16(4):7–11, 1995.

[11] B. Taylor and M.S. Imbabi. The effect of air film thermal resistance on the behavior of dynamic insulation. *Building and Environment*, 32(5):397–404, 1997.

[12] A. Dimoudi, A. Androutsopoulos, and S. Lykoudis. Experimental work on a linked, dynamic and ventilated, wall component. *Energy and Buildings*, 36(5):443–453, 2004.

[13] E. Elsarrag, M. Aboulnaga, A. Peacock, and M.S. Imbabi. Dynamic insulation for energy conservation and improved indoor air quality in hot humid

climates. In *ASHRAE Emirates Falcon Chapter, 5th Chapters Regional Conference (CRC)*, Dubai, November 2006.

[14] J.M. Wong, F.P. Glasser, and M.S. Imbabi. Evaluation of thermal conductivity in air permeable concrete for dynamic breathing wall construction. *Renewable Energy*, 31:729–738, 2006.

[15] W.G. Gray. A derivation of the equations for multi-phase transport. *Chemical Engineering Science*, 30:229–233, 1975.

[16] W.G. Gray and P.C.Y. Lee. On the theorems for local volume averaging of multiphase systems. *International Journal of Multiphase Flow*, 3:333–340, 1977.

[17] M. Hassanizadeh and W.G. Gray. General conservation equations for multi-phase systems: 1.averaging procedure. *Advances in Water Resources*, 2(September):131–144, 1979.

[18] M. Hassanizadeh and W.G. Gray. General conservation equations for multiphase systems: 2.mass, momenta, energy and entropy equations. *Advances in Water Resources*, 2(December):191–144, 1979.

[19] M. Hassanizadeh and W.G. Gray. General conservation equations for multiphase systems: 3.constitutive theory for porous media flow. *Advances in Water Resources*, 3(March):25–40, 1980.

[20] M.Kaviany. *Principles of Heat Transfer in Porous Media.* Springer, New York, second edition, 1995.

[21] A. Bejan and D. Nield. *Convection in Porous Media.* Springer, New York, third edition, 2006.

[22] S. Ergun and A.A. Orning. Fluid flow through randomly packed columns and fluidized beds. *Industrial & Engineering Chemistry*, 41:1179–1184, 1949.

[23] M. Quintard, M. Kaviany, and S. Whitaker. Two-medium treatment of heat transfer in porous media: numerical results for effective properties. *Advances in Water Resources*, 20:191–203, 1997.

[24] M. Quintard and S. Whitaker. Local thermal equilibrium for transient heat conduction: theory and comparison with numerical experiments. *International Journal of Heat and Mass Transfer*, 38:2779–2796, 1995.

[25] C. Moyne, S. Didierjean, H.P. Amaral Souto, and O.T. da Silveira. Thermal dispersion in porous media: one-equation model. *International Journal of Heat and Mass Transfer*, 43:3853–3867, 2000.

[26] M.H.J. Pedras and M.J.S. de Lemos. Thermal dispersion in porous media as a function of solid-fluid conductivity ratio. *International Journal of Heat and Mass Transfer*, 51:5359–5367, 2008.

[27] A. Ahmadi, A. Aigueperse, and M. Quintard. Calculation of the effective properties describing active dispersion in porous media: from simple to complex unit cells. *Advances in Water Resources*, 24:423–438, 2001.

[28] M. Quintard, F. Cherblanc, and S. Whitaker. Dispersion in heterogeneous porous media: One-equation non-equilibrium model. *Transport in Porous Media*, 44:181–203, 2001.

[29] C.T. Hsu. A closure model for transient heat conduction in porous media. *Journal of Heat Transfer*, 121:733–739, 1999.

[30] V.M. Malhotra. No-fines concrete - its properties and applications. *ACI Journal*, 73:628–644, 1976.

[31] N. Ghafoori and S. Dutta. Building and nonpavement applications of no-fines concrete. *Journal of Materials in Civil Engineering*, 7:286–289, 1995.

[32] N. Neithalath, M.S. Sumanasooriya, and O. Deo. Characterizing pore volume, size and connectivity in pervious concrete for permeability prediction. *Materials Characterization*, 61:802–813, 2010.

[33] Izhar-Ul-Haq, N.S. Saxena, S.E. Gustafsson, and A. Maqsood. Simultaneous measurement of thermal conductivity and thermal diffusivity of rock-marbles using transient plane source (tps) technique. *Heat Recovery Systems & CHP*, 11(4):249–254, 1991.

[34] A. Bouguerra, A. Ait-Mokhtar, 0. Amiri, and M.B. Diop. Measurement of thermal conductivity, thermal diffusivity and heat capacity of highly porous building materials using transient plane source technique. *International Communications in Heat and Mass Transfer*, 28(8):1065–1078, 2001.

[35] Y. He. Rapid thermal conductivity measurement with a hot disk sensor - part 1. theoretical considerations. *Thermochimica Acta*, 436:122–129, 2005.

[36] S.A. Al-Ajlan. Measurements of thermal properties of insulation materials by using transient plane source technique. *Applied Thermal Engineering*, 26:2184–2191, 2006.

[37] A. Franco. An apparatus for the routine measurement of thermal conductivity of materials for building application based on a transient hot-wire method. *Applied Thermal Engineering*, 27:2495–2504, 2007.

[38] M. Adler. Reconstructed porous media. In *Porpus media - geometry and transport*. Butterworth-Heinemann, Stoneham, first edition, 1992.

[39] Y. Anguy, R. Ehrlich, A. Ahmadi, and M. Quintard. On the ability of a class of random models to portray structural features of real, observed, porous media in relation to fluid flow. 23:313–330, 2001.

[40] F. Nekka and J. Li. A new analysis approach to porous media texture - mathematical tools for signal analysis in a context of increasing complexity. In *Mathematical Models and Methods for Real World Systems*. Taylor & Francis Group, London, first edition, 2006.

[41] *FLUENT 6.3 User's Guide*. ©Fluent Inc., 2006.

[42] *ISO 22007-2:2008(E) Plastics - Determination of thermal diffusivity - Part 2: Transient plane source (hot disk) method.* 2008.

[43] A. Quarteroni, R. Sacco, and F. Saleri. *Matematica numerica.* Springer-Verlag, Milano, third edition, 2008.

[44] F.P. Incropera, D.P. Dewitt, and T.L. Bergman. *Fundamentals of Heat and Mass Transfer.* John Wiley & Sons, Hoboken NJ, seventh edition, 2012.

[45] *EN ISO 6946 Building components and building elements - Thermal resistance and thermal transmittance - Calculation method.* 2007.

[46] *TRNSYS 16 - a TRaNsient SYstem Simulation program.* ©Solar Energy Laboratory, University of Wisconsin-Madison, 2007.